



ALMA MATER STUDIORUM  
UNIVERSITÀ DI BOLOGNA

DOTTORATO DI RICERCA IN  
INGEGNERIA ELETTRONICA, TELECOMUNICAZIONI E TECNOLOGIE  
DELL'INFORMAZIONE

Ciclo 36

**Settore Concorsuale:** 09/F2 - TELECOMUNICAZIONI

**Settore Scientifico Disciplinare:** ING-INF/03 - TELECOMUNICAZIONI

"INTERFERENCE MANAGEMENT TECHNIQUES FOR NON-TERRESTRIAL  
NETWORKS IN 5G/6G SYSTEMS"

**Presentata da:** M. Rabih Dakkak

**Coordinatore Dottorato**

Aldo Romani

**Supervisore**

Alessandro Vanelli Coralli

**Co-supervisore**

Alessandro Guidotti

Daniel Gaetano Riviello

## Abstract

Non-Terrestrial Network (NTN) can be defined as communication systems that use air-/space-borne platforms to establish communication links among various points on Earth's surface. These networks use airborne or spaceborne vehicles, involving satellites at Low Earth Orbit (LEO), Medium Earth Orbit (MEO), and Geostationary Earth Orbit (GEO), High Altitude Platforms Systems (HAPS), Low Altitude Platforms (LAPs), and drones. In the context of Fifth Generation (5G), NTN aims at the use of NTN platforms to enhance the flexibility, adaptability and the resilience of 5G Terrestrial Network (TN) system as well as to extend its coverage and provide connectivity to rural and underserved/un-served areas. In Sixth Generation (6G), NTN is expected to play an even more pivotal role, potentially forming a significant part of the global communication infrastructure. The unification of TN and NTN in 6G is envisioned to enable global coverage, low-latency communication, and support for massive Internet of Things (IoT) deployments. This unification will require advances in satellite and aerial communication technologies, as well as seamless integration with terrestrial networks to ensure ubiquitous and reliable connectivity. Furthermore, the use of NTN in 6G is expected to bring about new challenges in terms of network architecture and spectrum management. In this thesis, the research focuses on analysis the performance of a multi-beam LEO satellite systems since they provide reduced propagation delays and power consumption compared to GEO and MEO, as well as global coverage compared to HAPS and drones. The scarcity of spectrum resources to meet the demanding requirements of future Beyond 5G (B5G)/6G communication systems is considered one of the main challenges. To this aim, the current state of the art considers several strategies aimed at efficient utilization of the available spectrum bandwidth through either dynamic spectrum utilization schemes, such as Cognitive Radio solutions, or by fully exploiting the spectrum by decreasing the frequency reuse

factor down to Full Frequency Reuse (FFR). However, the latter solution introduces substantial Co-Channel Interference (CCI) or also known as Inter-Beam Interference (IBI), thus calling for the use of advanced interference management techniques at the transmitter side, i.e, at the satellite. This issue is addressed throughout the thesis by introducing interference management schemes and solutions within the following aspects and considerations:

1. Design and implementation of Multi-User (MU)-Multiple-Input-Multiple-Output (MIMO) for the Downlink (DL) transmission by assuming of a standalone LEO satellite equipped with an on-board Uniform Planar Array (UPA), which provides connectivity to the on-ground users equipped with Very Small Aperture Terminal (VSAT) antennas. Furthermore, we propose a Limited Field Of View (LFOV) planar array architecture composed of smaller planar subarrays in order to increase the directivity of the radiation pattern. The numerical results show the performance improvement of the proposed architecture compared to the non-subarrayed scenario in terms of interference rejection capability.
2. Introducing and proposing a unicast Signal-to-Leakage-Plus-Noise Ratio (SLNR) Beamforming (BF) scheme in standalone LEO satellite scenario. Furthermore, we provide a comparison between the proposed scheme and the current benchmark beamforming schemes including both those based on Channel State Information (CSI) knowledge at the transmitter, i.e., Minimum Mean Square Error (MMSE), and Zero-Forcing (ZF), and those only requiring the users' locations, i.e., Switchable Multi-beam (MB), and the Conventional Beamforming (CBF). The analysis shows the superiority of the proposed scheme with respect to the reference ones.
3. We extend the previous scenario of a standalone LEO satellite by proposing a swarm of multiple LEO satellite nodes aiming to provide global coverage and

service continuity. In this scenario, we introduce Cell Free distributed MIMO beamforming schemes incorporated with LFOV subarrays architectures, and we benchmark the performance with respect to the reference design.

4. Finally, we provide an overview on the future technologies enhancement of the thesis work such as incorporating AI/ML to predict CSI of NTN channel to improve CSI-based beamforming performance, and other possible enabling technologies in NTN will be discussed.

Part of this work has been supported by the following projects:

*The European Union Horizon-2020 Project, **DYNASAT** (Dynamic Spectrum Sharing and Bandwidth-Efficient Techniques for High-Throughput MIMO Satellite Systems) under Grant Agreement 101004145.*

*The **6G-NTN project**, which received funding from the Smart Networks and Services Joint Undertaking (SNS JU) under the European Union's Horizon Europe research and innovation programme under Grant Agreement No 101096479.*

# Table of Contents

<b>Abstract</b> . . . . .	<b>ii</b>
<b>Table of Contents</b> . . . . .	<b>ix</b>
<b>List of Figures</b> . . . . .	<b>x</b>
<b>List of Tables</b> . . . . .	<b>xii</b>
<b>Abbreviations</b> . . . . .	<b>xiii</b>
<b>Chapter 1 - Overview on Non-Terrestrial Networks in 5G and Beyond</b> . . . . .	<b>1</b>
1.1 NTN Nodes Topology . . . . .	2
1.2 NTN Platform Category . . . . .	3
1.2.1 Spaceborne category . . . . .	4
1.2.2 Airborne category . . . . .	5
1.3 Satellite Communication System Architecture . . . . .	7
1.3.1 Space Segment . . . . .	7
1.3.2 Ground Segment . . . . .	13
1.3.3 Satellite Communication Links . . . . .	14

1.4	NTN in 3GPP Standardization . . . . .	16
1.5	Main NTN Impairments . . . . .	20
1.5.1	Propagation delay: . . . . .	21
1.5.2	Doppler effect: . . . . .	25
1.5.3	Path Loss . . . . .	25
1.6	Frequency Reuse (FR) schemes in NTN . . . . .	29
 <b>Chapter 2 - System Characterization of Single LEO Satellite Scenario . . . . .</b>		<b>34</b>
2.1	Notation . . . . .	35
2.2	System architecture . . . . .	35
2.3	Antenna array model . . . . .	38
2.4	Channel model . . . . .	41
2.5	MIMO beamforming in standalone LEO satellite scenario . . . . .	42
2.6	Key Performance Indicators (KPIs) of the system . . . . .	46
 <b>Chapter 3 - Benchmark Beamforming Schemes and Proposed SLNR Bemforming Scheme for NTN systems . . . . .</b>		<b>48</b>
3.1	Benchmark beamforming algorithms . . . . .	50
3.1.1	CSI-based beamforming schemes . . . . .	50
3.1.2	Location-based beamforming schemes . . . . .	52

3.2	Proposed SLNR-based beamforming . . . . .	54
3.2.1	Literature . . . . .	54
3.2.2	Contribution . . . . .	55
3.2.3	Mathematical definition . . . . .	55
3.3	Complexity analysis . . . . .	58
3.4	Power Normalization Algorithms . . . . .	61
3.5	Numerical results . . . . .	62
3.5.1	Assumptions and System parameters . . . . .	62
3.5.2	Discussion and results . . . . .	67
3.6	Conclusions . . . . .	76
 <b>Chapter 4 - LFOV Planar Subarrayed Architecture with Beamforming in NTN Systems . . . . .</b>		<b>78</b>
4.1	State of the art on subarrays . . . . .	79
4.1.1	Contribution . . . . .	82
4.2	Mathematical model . . . . .	82
4.3	Numerical Assessment . . . . .	85
4.4	Conclusions . . . . .	93
 <b>Chapter 5 - Cell-Free Federated MIMO Beamforming in Multiple LEO Satellite Scenario . . . . .</b>		<b>94</b>

5.1	Contribution . . . . .	96
5.2	System architecture options . . . . .	96
5.3	System Model . . . . .	97
5.4	Distributed beamforming schemes . . . . .	104
5.5	Numerical results . . . . .	108
5.6	Conclusions and future works . . . . .	114
 <b>Chapter 6 - Conclusion and Future Possible Technologies for MU-MIMO Beamforming in 5G/6G NTN . . . . .</b>		<b>116</b>
6.1	Thesis conclusion . . . . .	116
6.2	Future work and possible enabling technologies . . . . .	118
 <b>References . . . . .</b>		<b>122</b>
 <b>Acknowledgements . . . . .</b>		<b>134</b>

## List of Figures

1.1	NTN toplogy . . . . .	3
1.2	NTN platform category . . . . .	5
1.3	High level SatCom system architecture . . . . .	7
1.4	Payload types . . . . .	9
1.5	Single-beam and Multi-beam satellite coverage . . . . .	10
1.6	Types of beams . . . . .	11
1.7	Types of coverage . . . . .	12
1.8	Examples of satellite use cases. . . . .	18
1.9	Interaction between TN and NTN before and beyond 5G . . . . .	20
1.10	NTN 3GPP roadmap. . . . .	21
1.11	Typical 71-beam coverage of Europe.. . . . .	30
1.12	Frequency reuse schemes with the same polarization. . . . .	31
1.13	Available bandwidth for FR schemes with two polarizations. . . . .	32
2.1	Single LEO satellite system architecture . . . . .	36
2.2	Coordinate system for the Uniform Planar Array model. . . . .	38
2.3	Block diagram of feed space beamforming considering OGBF and OBBF . . . . .	44
3.1	Block diagram depicting the leakage from user 1 on other users. . . . .	57
3.2	complexity analysis for SLNR and MMSE BF. . . . .	60
3.3	Beam lattice generated by LEO satellite in S-band. . . . .	67
3.4	CDF of users' SINR and spectral efficiency for fixed VSATs in LOS scenario, at $P_t = 4$ dBW/MHz. . . . .	70

3.5	CDF of users' spectral efficiency for fixed VSATs in LOS scenario for SLNR and MMSE beamforming with different power density values, $P_1 = 1$ dBW/MHz (solid line), $P_2 = 4$ dBW/MHz (dashed line), and $P_3 = 7$ dBW/MHz (dotted line). . . . .	71
3.6	CDF of users' SINR and spectral efficiency for fixed VSATs in NLOS scenario with $P_t = 4$ dBW/MHz. . . . .	72
3.7	CDF of users' spectral efficiency for fixed VSATs and MMSE/SLNR beamforming schemes with $P_t = 4$ dBW/MHz in LOS scenario (solid line) and NLOS scenario (dashed line). . . . .	74
3.8	CDF of users' spectral efficiency for vehicular VSATs and all considered BF schemes in LOS and NLOS scenarios with $P_t = 4$ dBW/MHz. . . . .	75
4.1	Categories of subarrays architecture . . . . .	80
4.2	Structure of the subarrayed UPA on board of a single NTN node.	83
4.3	CDF of VSATs' spectral efficiency considering MMSE and CBF BF schemes. . . . .	88
4.4	CDF of users' spectral efficiency for VSATs considering SLNR and MMSE with different subarray configurations. . . . .	92
5.1	CF federated MIMO beamforming architecture for $p$ -th NGSO swarm. . . . .	98
5.2	Federated scenario ( $S = 2$ ). Blue lines represent the beam lattice generated by node 1 and magenta by node 2. . . . .	106
5.3	CDF of users' spectral efficiency considering federated MIMO BF schemes with different subarray configurations. . . . .	110
5.4	Average spectral efficiency with multi-node ( $S = 2$ ) and single node ( $S = 1$ ) scenario. . . . .	112
6.1	Block diagram of the proposed NN-based CSI prediction. . . . .	120
6.2	RIS-assisted beamforming scheme in LEO SatCom. . . . .	121

## List of Tables

1.1	The summarize of one-way and RTT delays for GEO and LEO satellites at $h_{sat}=600$ km, with transparent payloads. . . . .	22
1.2	The summarize of one-way and RTT delays for GEO and LEO satellites at $h_{sat}=600$ km, with regenerative payloads. . . . .	23
1.3	Doppler characterization for LEO satellites at altitude 600 km. . .	26
3.1	Comparison of BF schemes . . . . .	59
3.2	Receiving antenna parameters. . . . .	64
3.3	Simulation parameters (proposed SLNR BF). . . . .	68
3.4	Average performance of BF schemes in case of CSI estimation with channel aging vs. genie-aided CSI estimation. . . . .	76
4.1	System Configuration Parameters (proposed LFOV architecture) .	86
4.2	Performance of BF with subarraying $M_H \times M_V$ . . . . .	90
5.1	System Configuration Parameters (CF Federated MIMO) . . . . .	107
5.2	Performance of BF with subarraying $M_H \times M_V$ , dual satellite ( $S = 2$ ).113	113
5.3	Simulation parameters ( $S = 1$ scenario). . . . .	114

## Abbreviations

<b>3GPP</b>	3rd Generation Partnership Project
<b>5G</b>	Fifth Generation
<b>5GC</b>	5G Core network
<b>6G</b>	Sixth Generation
<b>B5G</b>	Beyond 5G
<b>BF</b>	Beamforming
<b>BFN</b>	Beamforming Network
<b>CBF</b>	Conventional Beamforming
<b>CCI</b>	Co-Channel Interference
<b>CDF</b>	Cummulative Distribution Function
<b>CF</b>	Cell-Free
<b>CL</b>	Clutter Loss
<b>CSI</b>	Channel State Information
<b>CT</b>	Core Network and Terminals
<b>CU</b>	Centralized Unit
<b>DL</b>	Downlink
<b>DU</b>	Distributed Unit
<b>EIRP</b>	Effective Isotropic Radiated Power
<b>eMBB</b>	enhanced Mobile Broadband
<b>eMTC</b>	enhanced Machine Type Communications

**FFR** Full Frequency Reuse  
**FoV** Field of View  
**FR** Frequency Reuse  
**FR1** Frequency-range 1  
**FR2** Frequency-range 2  
**FSL** Free Space Loss  
  
**GEO** Geostationary Earth Orbit  
**GSO** Geosynchronous Orbiting  
**GW** Gateways  
  
**HAPS** High Altitude Platforms Systems  
**HARQ** Hybrid Automatic Repeat reQuest  
  
**IBI** Inter-Beam Interference  
**INR** Interference-to-Noise Ratio  
**IoT** Internet of Things  
  
**KPIs** Key Performance Indicators  
  
**LAPs** Low Altitude Platforms  
**LEO** Low Earth Orbit  
**LFOV** Limited Field Of View  
**LHCP** Left Hand Circular Polarization  
**LOS** Line of Sight  
**LOs** Local Oscillators  
**LSTM** Long Short Term Memory

**MB** Multi-beam  
**MC** Multi-Connectivity  
**MEO** Medium Earth Orbit  
**MIMO** Multiple-Input-Multiple-Output  
**MMSE** Minimum Mean Square Error  
**MPC** Maximum Power Constraint  
**MU** Multi-User  
**MUD** Multi-User Detection  
**NB-IoT** Narrowband-Internet of Things  
**NG-RAN** Next Generation Radio Access Network  
**NGSO** Non-Geosynchronous Orbiting  
**NLOS** Non-Line Of Sight  
**NN** Neural Network  
**NOMA** Non Orthogonal Multiple Access  
**NTN** Non-Terrestrial Network  
**OBBF** On-Board Beamforming  
**OGBF** On-Ground Beamforming  
**PAC** Per-Antenna Power Constraint  
**PAPR** Peak-to-Average Power Ratio  
**RA** Random Access  
**RAN** Radio Access Networks  
**RHCP** Right Hand Circular Polarization

**RRM** Radio Resource Management  
**RTT** Round Trip Time  
**SA** Services and Systems Aspects  
**SEE** Secure and Energy Efficient  
**SINR** Signal-to-Interference-Plus-Noise-Ratio  
**SIR** Signal-to-Interference Ratio  
**SLNR** Signal-to-Leakage-Plus-Noise Ratio  
**sMPC** Swarm-based Maximum Power Constraint  
**SNR** Signal-to-Noise-Ratio  
**SPC** Sum Power Constraint  
**SSP** Sub-Satellite Point  
**sSPC** Swarm-based Sum Power Constraint  
**SV** Steering Vector  
**TA** Timing Advance  
**TN** Terrestrial Network  
**TSG** Technical Specifications Groups  
**UAS** Unmanned Aerial System  
**UAVs** Unmanned Aerial Vehicles  
**UEs** User Equipments  
**ULA** Uniform Linear Array  
**UPA** Uniform Planar Array  
**UTs** User Terminals  
**VSAT** Very Small Aperture Terminal  
**ZF** Zero-Forcing

# **Chapter 1 - Overview on Non-Terrestrial Networks in 5G and Beyond**

The integration of the NTN with 5G technology is aimed at enabling seamless connectivity and ubiquitous coverage, particularly in remote or rural areas where deploying traditional network infrastructure is not feasible. NTN is also expected to support various use cases, including IoT applications, emergency communications, and enhanced mobile broadband services. The development of 5G NTN is part of the broader effort to create a global, interconnected communication infrastructure that can deliver high-speed, low-latency connectivity to users across the world, regardless of their location. Firstly, this chapter covers the main aspects of NTN systems including the topology of NTN nodes and classification of NTN platforms based on the altitude. Secondly, it describes the segments of Satellite Communication (SatCom) architecture and how 5G/6G NTN is defined and developed in 3GPP standardization. Then, it discusses the main channel impairments in NTN systems, and the full frequency reuse schemes in multi-beam NTN system.

## 1.1 NTN Nodes Topology

NTN nodes can be categorized based on their topology, link types, and the connectivity service they can provide to the ground station.

There are two main categories of NTN network topology in which inter-node communication is organized as follows:

1. Star Topology: in this configuration, the system is structured as a star network, with each node having the capability to communicate exclusively with a designated central node known as the hub. Communication links are individually established between nodes and the central hub. Additionally, it is possible for each individual star topology to establish communication with another star topology by utilizing their central nodes or hubs, thereby forming a multi-star topology
2. Mesh Topology: mesh network topology consists of a set of ground stations or nodes, where each node can communicate with every other node through the NTN links. This provides redundancy and multiple paths for signals to travel, thus improving reliability. It is worth highlighting that each generic satellite, ground station or ground (user) terminal, can act as a network node.

Fig. 1.1 depicts the aforementioned satellite node topology by considering a) star topology and b) mesh topology.

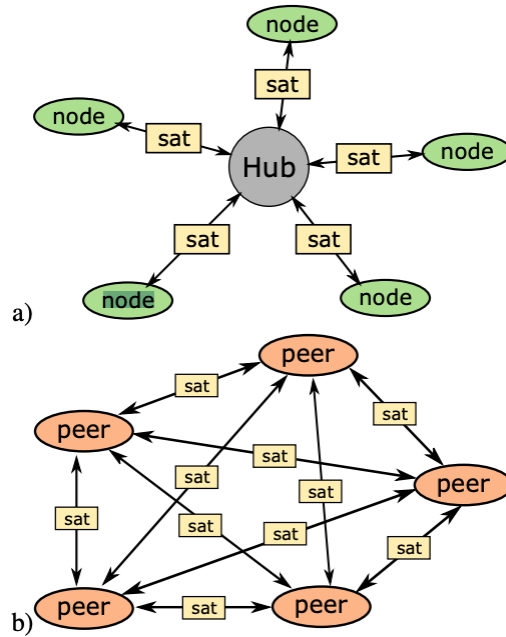


**Figure 1.1:** NTN topology a) Star, b) Mesh.  
[1]

## 1.2 NTN Platform Category

NTN systems have different deployment options according to the type of the NTN platform involved. NTN platforms are grouped into two main categories: spaceborne and airborne, as depicted in Fig. 1.2. The classification of these platforms typically depends on three main factors, such as i) altitude, i.e., the height above the Earth's surface at which the NTN platform, ii) beam footprint size, which refers to the area on the ground that is covered by the NTN node's beam, and iii) orbit, which is defined as a regular and repeating path (trajectory) followed by the satellite or NTN node in space.

### 1.2.1 Spaceborne category

NTN spaceborne encompasses Geosynchronous Orbiting (GSO) and Non-Geosynchronous Orbiting (NGSO) satellites:

1. GSO Satellites, in which the satellite is precisely at 35 786 km so as to match the Earth's rotation. From an observer on the Earth's surface, the satellite returns to exactly the same location in the sky after an orbital period. When the orbital plane is on the equatorial plane, the GSO satellite is in a Geostationary Earth Orbit (GEO) and from an observer's perspective on the Earth, it is in a fixed location in the sky at any time. GEO beam footprint size ranges of approximately from 200 to 3500 km [2, 3].
2. NGSO satellites do not have a fixed position in the sky with respect to the ground observers. To provide service continuity over time, a number of satellites (a constellation) is required to meet this objective: the lower the altitude, the higher the number of satellites. Different types of NGSO satellites are listed below:
  - Low Earth Orbit (LEO) Satellites, have a circular orbit around Earth, at an altitude ranges between 300 and 1500 km. The LEO beam footprint size ranges of approximately from 100 to 1000 km [2, 3].
  - Medium Earth Orbit (MEO) satellites, has a circular orbit<sup>1</sup> around the Earth, at an altitude varying from 7,000 to 25000 km [3]. MEO

---

<sup>1</sup>Circular orbits are those usually adopted for LEO satellites, but in MEO, this is not strictly necessary, in some cases they can have elliptical orbits.

beam footprint size ranges of approximately from 100 to 1,000 km [2, 3]. There are two MEO orbits of particular interest: the semi-synchronous and the Molniya orbits. As for the former, it is an MEO orbit at 20200 km, corresponding to an orbital period of 12 hours; thus, over a day, the satellite passes over the same location twice [4].

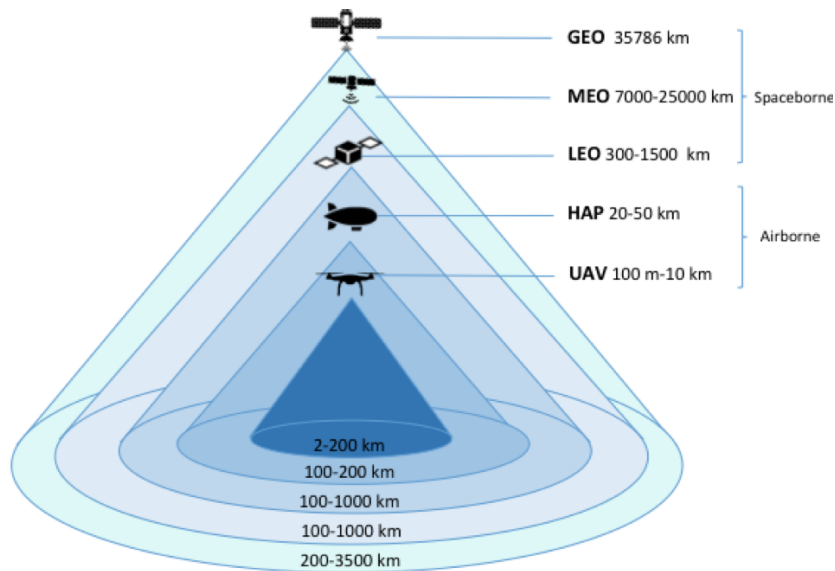


**Figure 1.2:** NTN platform category [3].

### 1.2.2 Airborne category

1. High-Altitude Platform Systems (HAPS), can be defined as vehicles stationed in the stratosphere at altitudes lower than satellites ranging between 20 to 50 km [2, 3]. They are effectively flying base stations that can provide localized coverage and help to bridge connectivity gaps in 5G/B5G NTN, particularly in areas where installing ground-based infrastructure is

challenging. HAPS can serve as relays for communication between ground stations or provide wireless connectivity to remote or disaster-stricken areas. They offer advantages such as longer mission duration compared to satellites and the ability to efficiently cover specific regions.

2. Low Altitude Platforms (LAPs), Unmanned Aerial Vehicles (UAVs), at altitudes ranging between 100 m to 10 km [2, 3], are the most prominent example of LAPs, but other systems, such as tethered balloons [5], have also been used for communication purposes. UAVs are expected to be an important component of the near-future wireless networks. They can potentially facilitate wireless broadcast and support high rate transmissions [6, 7]. The main benefits of UAVs (and LAPs) are similar to the HAPs ones, but at a cellular level: fast and flexible deployment, strong Line-of-Sight (LoS) connection links, and additional design degrees of freedom with the autonomous and controlled mobility. Despite the technological maturity of UAVs, UAV-based communication networks have not been widespread because of several limiting factors such as cost constraints, regulatory frameworks, and public acceptance [8]. The use of autonomous UAVs as 5G aerial base stations or as relays in a multi-layer vertical architecture is also a trending research topic [1].

It is worth mentioning that in the comparison between LEO and GEO/MEO satellites those which experience high propagation delays, LEO satellite systems provide a solution characterized by a lower latency and a better link budget, which can then lead to higher data rates. Furthermore, when compared to HAPS

and LAPs, LEO satellites provide broader coverage to a larger number of users on the ground. Consequently, LEO satellites have gained a significant attention in the research. In this thesis, the analysis and design specifically focus on LEO satellites within the realm of NTN types.

### 1.3 Satellite Communication System Architecture

The Satellite Communication (SatCom) system, as depicted in Fig. 1.3, consists of the following components: space segment, ground segment, and communication links.

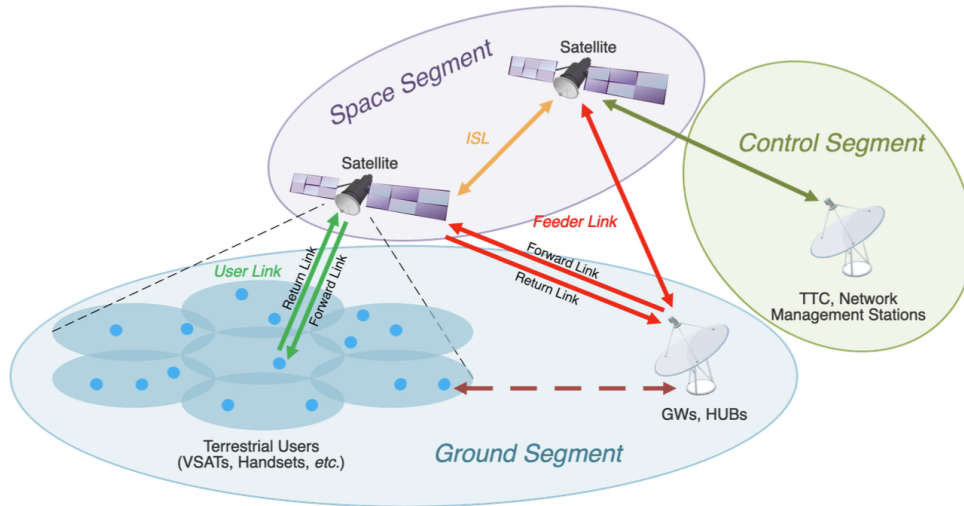


**Figure 1.3:** High level SatCom system architecture [9].

#### 1.3.1 Space Segment

This segment includes active and spare satellites organized into a constellation. Each of them is composed of the payload and the platform.

- *The payload* in a satellite communications system refers to the equipment used to provide the services for which the satellite has been launched.

It typically includes receiving and transmitting antennas, as well as all the electronic equipment supporting signal transmissions. There are two main types of payload: transparent and regenerative; as depicted in Fig. 1.4.

1. A transparent payload, also known as bent pipe, behaves as a relay in space among the devices in the ground segment, as it implements amplification and frequency conversion of the received signal before transmitting it again. Due to power constraints on the satellite payload, the total bandwidth is divided into distinct sub-bands by using a series of filters called the input multiplexer (IMUX). Within each sub-band, carriers undergo amplification through dedicated power amplifiers and then recombined in the output multiplexer (OMUX). The chain amplifier linked to each sub-band is referred to as a satellite channel or transponder [10]. Moreover, the transparent payload can perform routing of beams, and routing of the carriers from one up-beam to a given down-beam considering either routing through different satellite channels or transponder hopping mechanism.
2. A regenerative payload is a more advanced and complex node, which performs signal processing, such as modulation/demodulation, coding/decoding, filtering, frequency conversion, amplification, and/or routing, before retransmitting the signal. This allows the payload to effectively "regenerate" the incoming signals [10]. The regenera-

tive payload is capable of on-board processing, which can be beneficial for 5G satellite integration, but it also poses challenges in terms of standardization and interface management, specifically, when regenerative payload integrate diverse technologies and components which may come from different manufacturers or have different specifications and standardization.

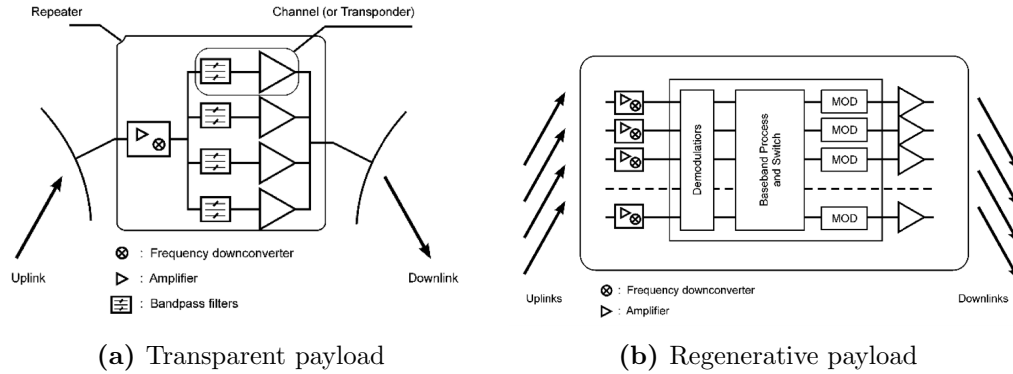


**Figure 1.4:** Payload types [10].

It is worth mentioning that the satellite payload can be utilized to generate either single-beam or multi-beam on the ground, as depicted in Fig. 1.5.

- A single-beam satellite, where each antenna generates one beam only; generally the satellite is equipped with one primary antenna that produces a concentrated beam directed toward a specific geographic area on the Earth’s surface. Single-beam satellites are often used in scenarios where the targeted coverage of a particular region is sufficient.
- A multi-beam satellite, where multiple-beam antennas generate multiple beams simultaneously. Each beam can be directed to different

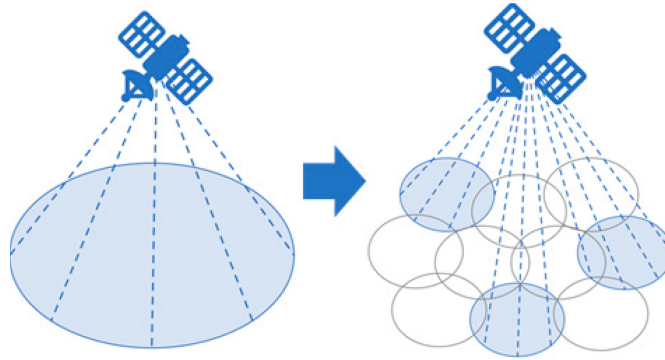


**Figure 1.5:** Single-beam and Multi-beam satellite coverage.  
[11]

regions on the Earth. This enables the satellite to cover a broader area or serve multiple users concurrently, as shown in Fig. 1.5 [11].

Single-beam satellites are simpler in design and operation compared to multi-beam satellites, making them suitable for applications with specific, well-defined communication needs. However, Multi-beam satellites offer advantages in terms of increased coverage flexibility, efficient spectrum utilization, and the ability to provide services to diverse geographical locations. Hence, in the thesis, a multiple-beam satellite scenario is assumed. If the satellite has several multiple-beam antennas, its coverage defines the satellite access area, which is directly related to the Field of View (FoV) of the satellite. However, in fact, the whole FoV can be smaller than the geometrical one due to some limitations, e.g., scan loss, mechanical limitations of the pointing mechanism, etc. Moreover, there are two types of beams [12], as depicted in Fig. 1.6 : i) Earth-fixed beams, i.e., through digitally steering of the signals, the coverage area generated by each NTN or satellite node is

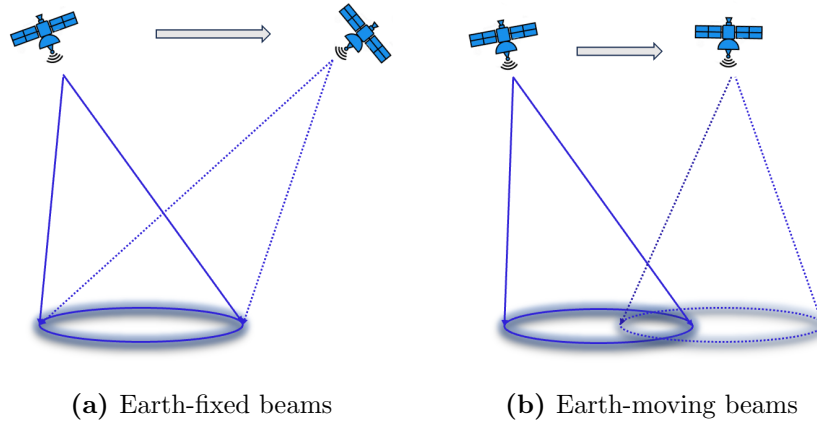


**Figure 1.6:** Types of beams.

fixed on-ground independently of its position on the orbit (as long as it falls in the node field of view); or ii) Earth-moving beams, i.e., the coverage area of each node is always centered around its Sub Node Point (SNP), i.e., the intersection between the Earth’s surface and the line connecting the satellite node with the Earth’s center, and thus, the beams move on-ground along with the node on its orbit [13].

In the context of coverage, a distinction can be made between instantaneous and long-term system coverage, as depicted in Fig. 1.7 [10]. Instantaneous coverage involves the combined coverage areas of individual satellites within the constellation at a specific moment. On the other hand, long-term coverage refers to the Earth’s region progressively monitored over time by the satellites in the constellation. For real-time services, the instantaneous system coverage consistently includes a footprint covering a geographical region where at least one element from the ground segment is present. To ensure continuous global coverage, a substantial number of satellites is necessary

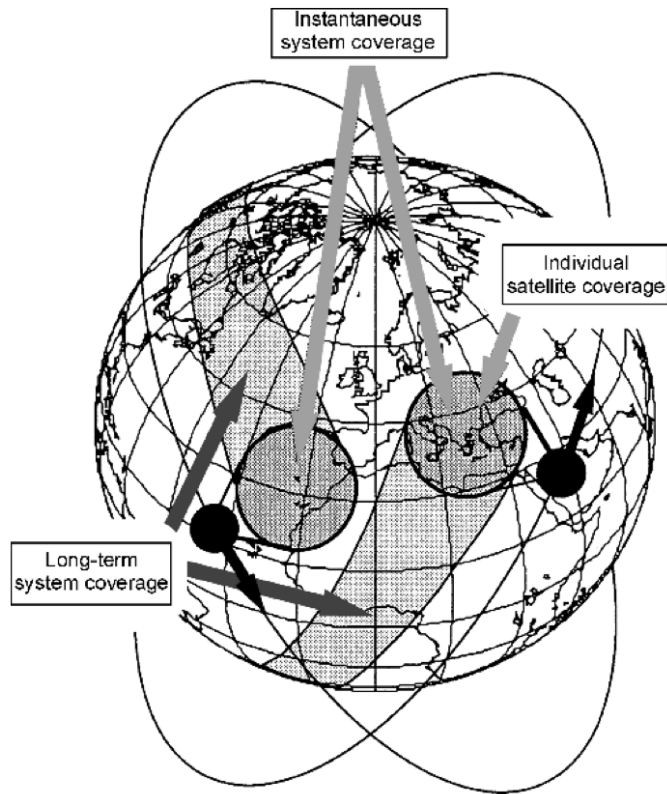


**Figure 1.7:** Types of coverage[10].

for constellations in LEO as will be discussed in Chapter 5. Regarding GEO satellite systems only require three satellites to achieve global coverage, excluding polar regions.

- *The platform:* this part is constituted by the collective subsystems facilitating the payload's operation. This encompasses elements such as: i) the fuel system ensuring the long-term satellite's functionality; ii) solar panels supplying the necessary energy for satellite operations.

### 1.3.2 Ground Segment

Ground segment or Earth stations include three categories: i) user ii) interface and iii) service. It mainly facilitates the management of the space segment and the distribution of the payload data and telemetry to relevant parties on the ground. Comprising both fixed and mobile Earth stations, it plays a pivotal role in establishing telecommunication links with all NTN nodes, including satellites. Earth stations can be categorized as follows:

- User Terminals (UTs) or User Equipments (UEs) on the ground provide the interface for end-users to connect with the non-terrestrial network. These terminals could be handheld (hh) mobile terminals, or Very Small Aperture Terminals (VSATs).
- Gateways (GW), which connect the space segment to a terrestrial network; they enable the transition of data between the non-terrestrial and terrestrial components, in which they play a crucial role in the routing and processing of data to ensure seamless communication between users on the ground and the satellite assets. However, it is worth mentioning that a direct connectivity between UEs covered by the same satellite(s), i.e., without the need for passing through a GW, is a topic currently being addressed for future 6G NTN systems.
- Service Stations, as hub or feeder stations, which are responsible for collecting and distributing the information from/to user stations through the space segment.

It is worth mentioning that there is another important section within SatCom architecture on the ground which is defined as control segment; it consists of Tracking, Telemetry, and Command (TTC) ground stations. Such stations aim to manage and monitor the space segment, i.e, satellites, through sending commands, receiving telemetry data, and ensuring satellites' operation according to mission objectives [1].

### **1.3.3 Satellite Communication Links**

Satellite communication links refer to the transmission of signals between ground-based stations and satellites orbiting in space or between the satellites in the space, as illustrated in Fig. 1.3. These links enable diverse applications such as broadcasting, telecommunications, and data exchange. They can be categorized into three types according to their role in NTN or SatCom system [14]:

1. Feeder Link: it establishes a communication link between a ground-based station and a satellite. It serves as the connection between the ground segment and the space segment, carrying signals from the ground station to the satellite UL (UpLink) or from the satellite to the ground station DL (DownLink).
2. User Link: it involves the communication link between a satellite and the UT on the ground, including the user DL from satellite to the user and the user UL from the ground users to the space.

3. Inter-Satellite Links (ISL) are communication links established between different NTN nodes or satellites within a constellation [15]. These links contribute to the coordination, synchronization, and data exchange among satellites, enhancing the overall performance of the satellite system [16]. ISLs can be classified in the following way [17]: i) Inter-Orbital Links, e.g., links between GEO and LEO satellites; ii) Intra-Orbital Links, e.g., those connect between GEO satellites or those connect between LEO satellites operating in the same orbit.

It is worth highlighting that ULs and DLs consist of radio-frequency modulated carriers, while ISLs can be either radio frequency or optical type-links [18]. Furthermore, a NTN link can be categorized based on the direction of the communication, distinguishing between forward and return links. The forward link is the connection from a GW, hub, or feeder station to a user terminal, while the return link is the reverse connection from the user terminal to other stations. Both types of connections require an UL and DL, and possibly one or more ISLs. All the aforementioned types of SatCom links are well-illustrated in Fig. 1.3. Within a satellite network, another classification of the links could be introduced as follows: i) unidirectional links, where certain stations exclusively transmit, and others solely receive; and ii) bidirectional links, where ground stations are involved in both transmitting and receiving. In networks focused on satellite broadcasting, unidirectional links are commonly used in a star topology, while bidirectional links can be utilized in either a star or mesh topology. Such bidirectional links are essential for facilitating two-way telecommunication services. Furthermore, vari-

ous connections are designated according to the type of service they provide. For example, point-to-point connectivity serves unicast purposes, point-to-multipoint is employed for multicast/broadcast scenarios, and multipoint-to-point is utilized for multiplexing and concentration. Meanwhile, multipoint-to-multipoint connections facilitate the simultaneous provision of diverse services.

#### 1.4 NTN in 3GPP Standardization

The standards of the 3rd Generation Partnership Project (3GPP) are called "releases", where each release brings new specifications. These releases are updated and revised continuously on-the-web, after thorough technical discussion and agreement, and all are available online as free-of-charge documents. The three Technical Specifications Groups (TSG) of 3GPP, each of them with a particular area of responsibility, can be identified as: i) Radio Access Networks (RAN) group, which is responsible for the technical co-ordination of the specification work in radio performance and protocol aspects; ii) Services and Systems Aspects (SA) group is responsible for the overall architecture and service capabilities of systems based on 3GPP specifications; and iii) Core Network and Terminals (CT) group, is responsible for the technical co-ordination of the specification work on terminal interfaces, user equipment, core network protocols, interworking with external networks,..etc [19].

By recognizing the added value of integrating NTN segment into the terrestrial New Radio (NR)<sup>2</sup> architecture, 3GPP initiated new activities in March 2017 to

---

<sup>2</sup>This is the 3GPP terminology for 5G and they will be interchanged throughout the thesis.

study the role of the NTN in 5G, and two study items (SI) have already been concluded [20, 21] as a part of Release 16, based on the findings and results of Release 15, TR 38.821 [22], in which they provided details about NTN architectures, challenges and the suggested solutions pertaining to Layer 1, encompassing physical layer procedures such as Random Access (RA) and Timing Advance (TA). The report also delves into radio protocols, including Hybrid Automatic Repeat reQuest (HARQ) and mobility management in the Control Plane, as well as architecture and interfaces, covering aspects like tracking area management and the handling of network identities. After two years of study phase, it was approved that NTN could be a new key feature of 5G and a work item (WI) started in January 2020 [23]. The three main categories of use cases for 5G NTN systems which have been outlined by 3GPP documents in release 16 [24], can be summarized as follows:

- NTN can significantly improve the reliability of the 5G network by ensuring service continuity in specific scenarios where be covered by standalone terrestrial network . This is particularly relevant for moving platforms such as cars, trains, airplanes, and mission-critical communications.
- Secondly, NTN can ensure the ubiquity of 5G service in unserved (e.g., deserts, oceans, forests, etc.) or underserved areas (e.g., urban areas) where a terrestrial network is either nonexistent or impractical/cost-ineffective to deploy.

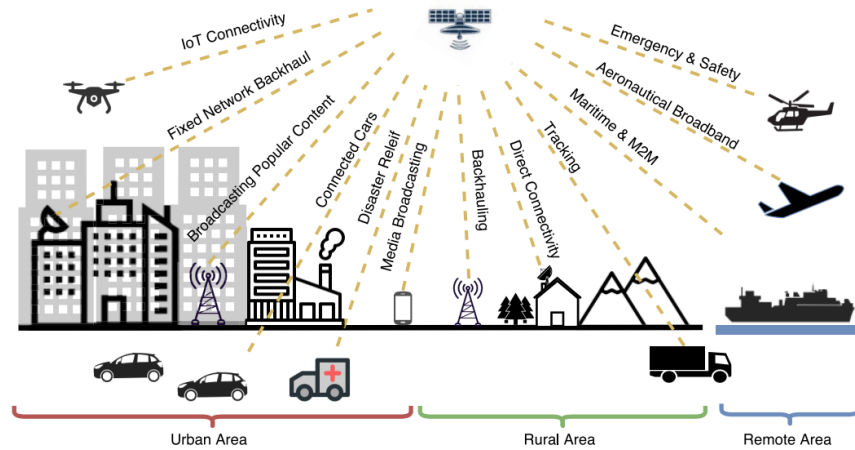


**Figure 1.8:** Examples of satellite use cases [1].

- Lastly, NTN can contribute to the scalability of 5G services by leveraging the effectiveness of satellites in multicasting or broadcasting across wider areas on the ground. This capability is beneficial for alleviating the burden on the terrestrial network, allowing the popular content to be distributed either to the network’s edge or directly to end-users. A more examples of satellite use cases for each 5G service group can be shown in Fig. 1.8.

The aforementioned studies marked a significant shift in defining a fully integrated NTN component within the 5G terrestrial system, commencing from the recently concluded Rel.17, in 2022, as depicted in Fig. 1.10. Rel.17 was driven by the minimisation of the impacts at UE, Next Generation Radio Access Network (NG-RAN), and 5G Core network (5GC) level to support NTN, by reusing as much as possible the terrestrial 5G specifications. It is considered the first NTN standard that provides the specifications for 3GPP non-terrestrial access based on both 5G NR and 4G Narrowband-Internet of Things (NB-IoT)/enhanced Machine

Type Communications (eMTC) radio protocols operating in Frequency-range 1 (FR1). In Rel.17, the NR-based satellite access is designed to serve handheld devices to provide enhanced Mobile Broadband (eMBB) services, while the NB-IoT/eMTC-based satellite access aims at providing MTC services to IoT devices for applications in agriculture, transport, logistics, and security markets. To support new scenarios and deployments above 10 GHz, as well as to introduce several enhancements for NR-NTN and IoT-NTN, a normative work is currently being carried out as part of Release 18. The support of IoT-NTN is largely aligned with that of NR-NTN in 5G System (5GS). It is worthwhile mentioning that, since access networks based on Unmanned Aerial System (UAS), including HAPS and drones, could be considered as a special case of NTN access with lower latencies and Doppler values (such NTN impairments will be explained in the next section) and variation rate, the main focus is on satellite-based NTN only. As for Rel. 19, the feature package reporting the studies that will be performed from 2024, has been defined and finalised during the 3GPP plenary in December 2023, as seen in Fig. 1.10. The evolution of NTN in the 5G ecosystem will continue in Rel.20 and beyond. Several additional features are under discussion as potential enhancements to be integrated into 5G-Advanced, e.g, the incorporation of regenerative payloads and further improvements in capacity and coverage, such as Multi-Connectivity (MC), and optimization of the downlink Peak-to-Average Power Ratio (PAPR). Further enhancements in the performance and capability of NTN system shall be assessed in B5G and 6G systems [25–28]. As illustrated in Fig. 1.9, prior to 5G, the optimization for TN and NTN was separated; then,

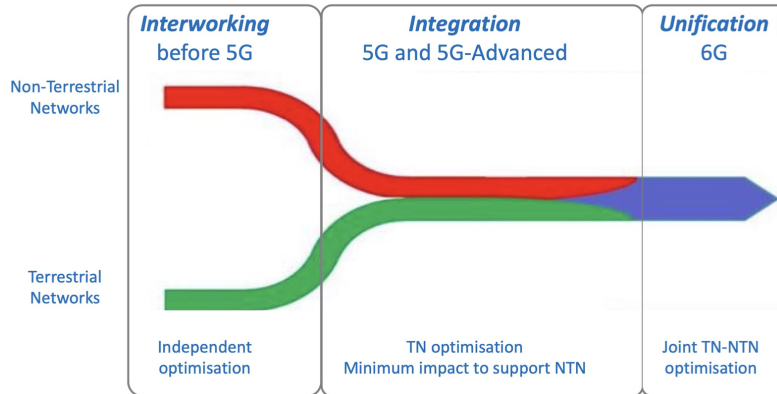


**Figure 1.9:** Interaction between TN and NTN before and beyond 5G [29].

with 5G and 5G-Advanced, the objective has been the optimisation of the TN and integration of the NTN component with minimum impact. However, in 6G systems, TN and NTN shall be jointly optimised in an unified integrated multi-layered infrastructure. In conclusion, the 3GPP acknowledged the significant role of NTN and incorporated it into Release 17. This release delineates how the integration of the NTN component facilitates the implementation of planned 5G services, paving the way towards 5G-Advanced and ultimately contributing to the development of 6G systems.

The roadmap for NTN standardization, as outlined in [29], is illustrated in Fig. 1.10, encompassing the current and expected developments up to Release 21.

## 1.5 Main NTN Impairments

In this section, we will discuss the typical satellite channel impairments that might have an impact on the NR PHY and MAC layers, as large propagation delays, Doppler shifts, and path loss.

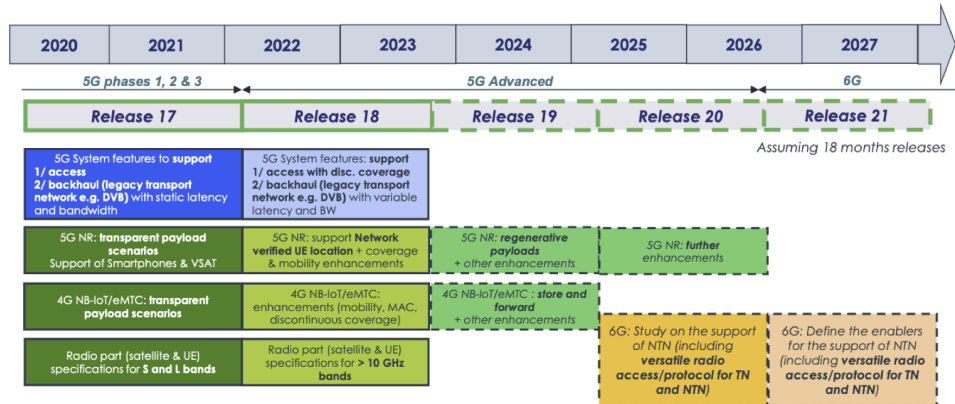


Figure 1.10: NTN 3GPP roadmap [29].

### 1.5.1 Propagation delay:

In NTN systems, different types of delay are involved considering the propagation delay, the most significant and predominant one, which is determined by the distance between the NTN node and the UE. The performance of NTN system, particularly those at higher altitudes like GEO satellites, is significantly affected by this delay. In such cases, the propagation delay becomes much greater than that in TN, having a substantial challenge in the design and analysis of SatCom systems, especially in the context of 5G NR. We consider only the propagation delay, since the signal processing delay can be assumed negligible with respect to the propagation one. Propagation delay encompasses both one-way propagation delay and Round Trip Time (RTT), depending on the specific procedure that will be considered. Before providing some examples of the the propagation delays, It is worth providing the definition of the elevation angle as the angle between the tangent to the Earth’s surface at the UE location and the satellite direction from

the UE location. By simply geometry considerations, this angle is always between  $0^\circ$  and  $180^\circ$  [4]. In the context of 3GPP NTN scenarios, for the propagation delay analyses, it is assumed that the UE and the GW minimum elevation angles, leading to the maximum delays, are given by  $\theta_{RX} = 10^\circ$  and  $\theta_{GW} = 10^\circ$ , respectively. Hence, from these values, the following equation can be used to obtain the slant range:

$$\mathbf{d} = \sqrt{(R_E + h_{sat})^2 - R_E^2 \cos^2 \theta} - R_E \sin \theta \quad (1.1)$$

Where:  $R_E$  denotes Earth radius and  $h_{sat}$  is the satellite altitude.

Scenario	Path	Slant range [km]	Latency [ms]
<b>GEO</b>	GW-sat	41121	137.07
	sat-RX	40581	135.27
	one-way	-	272.53
	RTT	-	545.06
<b>LEO</b>	GW-sat	2328	7.77
	sat-RX	1931	6.44
	one-way	-	14.19
	RTT	-	28.39

**Table 1.1:** The summarize of one-way and RTT delays for GEO and LEO satellites at  $h_{sat}=600$  km, with transparent payloads.

By assuming transparent payloads, in which the satellite behaves as a relay or

Scenario	Path	Slant range [km]	Latency [ms]
<b>GEO</b>	sat-RX	40581	135.27
	one-way	-	135.27
	RTT	-	270.54
<b>LEO</b>	sat-RX	1931	6.44
	one-way	-	6.44
	RTT	-	12.88

**Table 1.2:** The summarize of one-way and RTT delays for GEO and LEO satellites at  $h_{sat}=600$  km, with regenerative payloads.

repeater and hence the overall RTT can be computed between GW and the user as follows [30]:

$$RTT \simeq 2T_{owp} = 2 \frac{d_{GW-sat}(\theta_{GW}) + d_{sat-RX}(\theta_{RX})}{c}. \quad (1.2)$$

where:

- $T_{owp}$  is the one-way propagation delay.
- $d_{GW-sat}(\theta_{GW})$  is the distance between the GW and the satellite as a function of its elevation angle  $\theta_{GW}$ .
- $d_{sat-RX}(\theta_{RX})$  is the distance between the satellite and the receiver as a function of its elevation angle  $\theta_{RX}$ .

- $c$  is the speed of light.

For satellites with regenerative payloads, the connection is established between the UE and the satellite and, thus the overall RTT is:

$$RTT \simeq 2T_{owp} = 2 \frac{d_{sat-RX}(\theta_{RX})}{c}. \quad (1.3)$$

It is worth mentioning that, with regenerative payloads, the RTT could also be computed between the UE and the GW which is linked to gNB. In the 3GPP specifications, scheduling of both uplink and downlink transmissions is defined and performed at the Medium Access Control (MAC) layer in the gNB. To perform such operation, the gNB gathers all the required measurements from the served UEs and, based on the implemented scheduling algorithm, allocates the resources to the users. In the next chapters in particular Chapter 5, more details will be provided about this concept by discussing the possible options for regenerative payload architectures and considering either full gNB or introducing the functional splits on distributed gNBs (on board and on-ground) and its impact on the propagation delay and consequently on the system performance.

Tab. 1.1, Tab. 1.2 report the specific slant ranges, one-way delay, and RTT for GEO and LEO satellites at altitude  $h_{sat} = 600$  km, with transparent and regenerative payloads, respectively [4].

### 1.5.2 Doppler effect:

In differentiating between GEO and LEO satellite systems, the Doppler shift is particularly pronounced in LEO systems when the UE is positioned on the ground track, which is the projection of the orbital plane on the Earth's surface. In this scenario, a simplified formula for calculating the Doppler shift is proposed in [31]:

$$f_d(t) = \frac{f_0 \omega_{sat} \cdot R_E \cdot \cos \theta_{UE}(t)}{c} \quad (1.4)$$

where:  $f_0$  is the carrier nominal frequency,  $R_E$  is the Earth radius,  $\omega_{sat}$ , is the angular velocity of the satellite, and finally  $\theta_{UE}(t)$  is the elevation angle as a function of time, which is obtained assuming a fixed on-ground receiver; in case the receiver is moving, then the angular speed  $\omega_{sat}$  shall be modified so as to take into account the user's speed. In GEO (as well as HAPS) systems, the main factor contributing to the overall Doppler shift is the movement of the users. However, in LEO systems, the most significant factor affecting the Doppler shift is the high orbital speed of the satellite. In the Tab. 1.3 [4], we can notice that exist different expected maximum values of Doppler values for FR1 (less than 6 GHz) and Frequency-range 2 (FR2) (more than 6 GHz) for LEO satellite at altitude 600 km.

### 1.5.3 Path Loss

When assessing the losses in a satellite communication link between a ground-based UE and the satellite, the overall losses (L) can be determined as

Frequency (GHZ)	Max Doppler	Relative Doppler	Max Doppler Shift Variation
2	+/- 48 kHz	0.0024%	-544 Hz/s
20	+/- 480 kHz	0.0024%	-5.44 kHz/s
30	+/- 720 kHz	0.0024%	-8.16 kHz/s

**Table 1.3:** Doppler characterization for LEO satellites at altitude 600 km.

follows:

$$L = PL + L_E = \underbrace{L_B + L_A + L_{POL}}_{PL} + \underbrace{L_F + L_D}_{L_E} \quad (1.5)$$

where,  $PL$  denotes losses attributed to channel impairments, while  $L_E$  corresponds to losses associated with the equipment configuration; specifically:

- $L_B$  represents the basic path loss [32], including Free Space Loss (FSL), denoted as  $L_{fs}$ , Clutter Loss (CL),  $L_{CL}$ , and log-normal shadowing, ( $L_\sigma$ );

$$L_B = L_{cl} + L_{fs} + L_\sigma \quad (1.6)$$

- $L_A$  accounts for losses due to atmospheric conditions.
- $L_{POL}$  represents the loss due to polarization mismatch.
- $L_F$  represents losses within the equipment

- $L_D$  corresponds to depointing losses.

The clutter loss characterizes the signal power attenuation due to nearby buildings and obstacles on the ground. It is impacted by factors such as the elevation angle, the operational frequency of the system ( $f_c$ ), and the specific environmental conditions. The values of this parameter can be found in [33] for different scenarios, and it is conventionally considered negligible in Line of Sight (LOS) conditions. For a user positioned at a slant range  $d$  from the satellite, the Free Space Loss (FSL) is determined by:

$$L_{fs} = 20 \log_{10} \left( \frac{4\pi d f_c}{c} \right) \quad (1.7)$$

Regarding the shadowing loss,  $L_\sigma$ , is represented as a log-normal random variable with a mean of zero and a variance that corresponds to the harshness of the shadowing environment, that is,  $L_\sigma \sim (0, \sigma_s^2)$ . The values for  $\sigma_s^2$  are provided by 3GPP for various scenarios such as dense urban, urban, and rural, and these values are dependent on the elevation angle [33]. Atmospheric losses encompass factors such as absorption by atmospheric gases, denoted as  $L_{gas}$ , attenuation due to rain/snowfall and cloud, expressed as  $L_{rain}$ , and losses associated with scintillation, represented by  $L_s$ :

$$L_A = L_{gas} + L_{rain} + L_s \quad (1.8)$$

Moreover, rain attenuation is regarded as negligible for frequencies below 6 GHz, as highlighted in [33]. Scintillation is the rapid variation of the amplitude and

phase of the the received signal, associated with the fluctuations in the refractive index in the troposphere and ionosphere [34]. It is modeled as follows:

- Tropospheric scintillations, affecting signals in the Ka-band, are modeled as a fixed term dependent on the user's elevation angle, and these values are determined using the procedure outlined in ITU-R P.618 [35].
- Ionospheric scintillations, impacting signals in the S-band, are modeled as a fixed term with a magnitude of 2.2 dB, as per [33], and this modeling approach is described in ITU-R P.531-13 [36].

Moreover, polarization mismatch loss should be be considered when the receiving antenna is not aligned with the polarization of the received wave. This can happen due to the fact that the propagation through the atmosphere can affect the polarization. For instance, the ionosphere can cause a rotation of the plane of polarization of an angle,  $\Delta\psi$ , which is inversely proportional to the square of the frequency. This rotation can be particularly problematic for linear polarization. In general, the polarization mismatch loss can be defined as [10]:

$$L_{POL} = -20 \log_{10}(\cos \Delta\psi) \quad (1.9)$$

The equipment losses, also known as feeder losses, refer to the losses in the transmitting and receiving equipment, typically occurring in the feeder between the power amplifier and the antenna:

$$L_F = L_{FTX} + L_{FRX} \quad (1.10)$$

In particular,  $L_{FTX}$  is the feeder loss between the transmitter and the antenna, while  $L_{FRX}$  is the feeder loss between the antenna and the receiver.

Finally, the depointing losses are functions of transmitting and receiving angular misalignment,  $\epsilon_T$  and  $\epsilon_R$  respectively, with respect to the antenna boresight. The result is arises from the decrease in antenna gain with respect to both the maximum gain during transmission and reception, which can be formulated as a function of the  $\epsilon_{3dB}$  as follows:

$$L_D = L_T + L_R = 12 \left( \frac{\epsilon_T}{\epsilon_{3dB}} \right) + 12 \left( \frac{\epsilon_R}{\epsilon_{3dB}} \right) \quad (1.11)$$

## 1.6 Frequency Reuse (FR) schemes in NTN

To define the concept of Frequency Reuse (FR) schemes, we consider multi-beam satellite architecture which allows to reuse the same bandwidth in different beams. In this case, the service area is divided into small beams in order to reuse the frequency spectrum and thus to improve the spectral efficiency. Fig. 1.11 shows an example of typical 71-beam coverage of Europe, adopted by broadcast and unicast systems.

Frequency reuse schemes can effectively reuse the available frequency spectrum across different beams with the same polarization or considering dual polarization scenario. The term of "color" in this context refers to a subset of channels (users) that utilize the same bandwidth or polarization. Each coloring scheme defines a base coloring pattern by assigning each beam to a color, thereby enhancing the efficiency and capacity of the system [37].

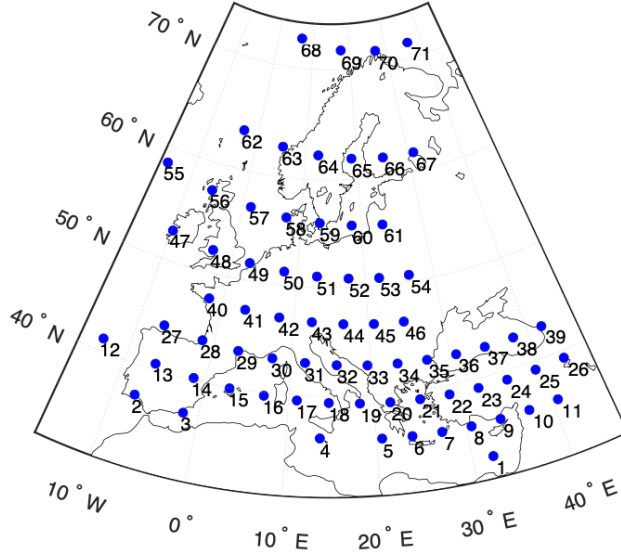


**Figure 1.11:** Example of typical 71-beam coverage of Europe.

- Frequency Reuse schemes with the same polarization:** Four-Color scheme FR4; which is the commonly adopted solution in most of High Throughput Systems (HTS) within NTN, is chosen due to its ability in ensuring a low level of interference [38]. Fig. 1.12a shows an example of FR4 reuse scheme, in which the interference is very limited and can be neglected at the receiver. By considering Lower frequency reuse factors, we can also define, as shown in Fig. 1.12b, the 2-color frequency reuse scheme, or as known as FR2. Moreover, using more aggressive frequency reuse schemes, i.e., 1-color scheme or Full Frequency Reuse (FFR) scheme, can increase the bandwidth more efficiently, and introduce higher interference as all users in the co-channel share the same spectral resources. Managing such interfer-

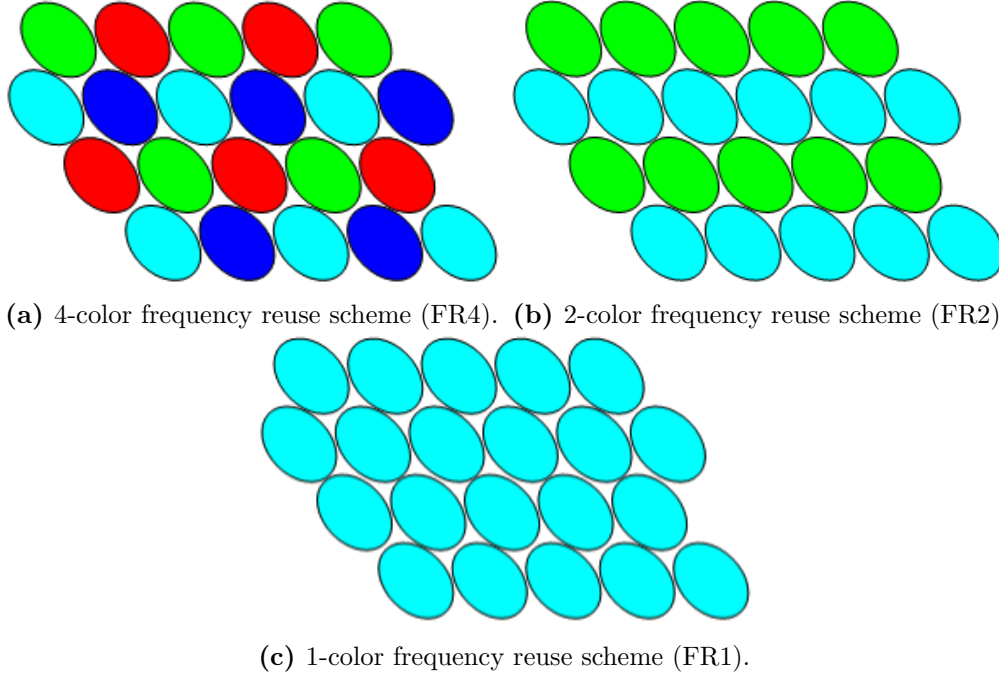


**Figure 1.12:** Frequency reuse schemes with the same polarization.

ence is essential, either at the receiver side and/or at the transmitter side, as will be discussed later.

- **Frequency reuse schemes with dual polarization:**

A 4-color scheme represents in the previous scheme 4 sub-bands and one polarization, however, in dual polarization scenario, it refers to 2 sub-bands and 2 polarization, i.e., Right Hand Circular Polarization (RHCP) or Left Hand Circular Polarization (LHCP), as shown on Fig. 1.13a. The signals in the FR4 scheme occupy half of the available bandwidth. This coloring scheme has excellent interference isolation properties, i.e., the CCI is very low, but is inherently limited in per-beam bandwidth (FR factor= 1/4)

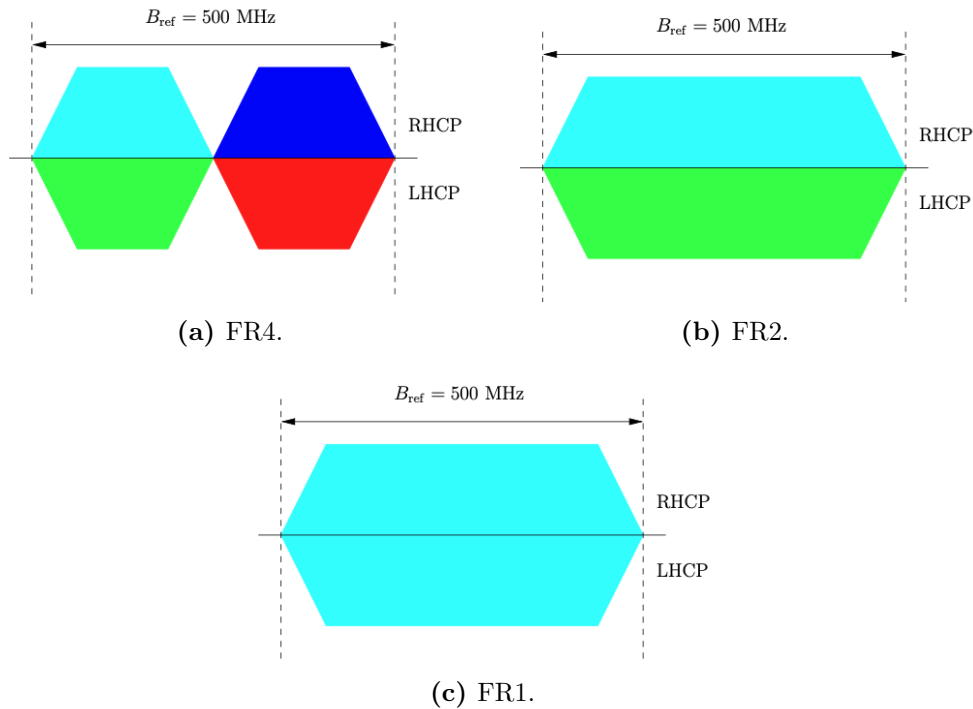


**Figure 1.13:** Available bandwidth for FR schemes with two polarizations.

and hence in performance [37]. Therefore, using more aggressive coloring schemes such as a 2-color scheme, i.e., 1 sub-band (the whole band) per each polarization (FRF = 1/2) will be essential to increase the system capacity by providing twice as much bandwidth to each beam. An example of a 2-color scheme in this scenario is depicted in Fig. 1.13b. Finally, in 1-color scheme, the same user is served by both polarizations, as shown in Fig. 1.13c.

In the context of NTN systems, particularly when adopting the FFR scheme (as assumed in our thesis), the challenge of CCI becomes notably prominent. Hence, it is imperative to employ techniques to mitigate and manage such interference, these techniques can be implemented either at: i) at the transmitter

side, e.g., multi-user MIMO such as coordinated MultiPoint (coMP) transmission techniques [39–42], Non Orthogonal Multiple Access (NOMA) for 5G systems [43–47], time-frequency packing for satellite systems [48, 49]; and/or ii) at the receiver such as Multi-User Detection (MUD) schemes [50–52]. The main focus of the next chapters in the thesis will be on design and evaluation of MU-MIMO algorithms at the transmitter, i.e, at the LEO NTN node/nodes including advanced analysis of beamforming schemes.

## Chapter 2 - System Characterization of Single LEO Satellite Scenario

This chapter describes the system model of standalone LEO satellite nodes in 5G and beyond. Such LEO satellite will implement MIMO BeamForming (BF) techniques that are discussed in the next chapter.

Firstly, we provide a general definition of the assumed satellite system architecture and then describe the considered antenna array and the channel model. Secondly, the classification of MIMO beamforming architecture in SatCom will be explained. Finally, we highlight the main Key Performance Indicators (KPIs) utilized in the system level performance.

The content of this chapter is included in the following published paper:  
M.R. Dakkak, D. G. Riviello , A. Guidotti, and A. Vanelli-Coralli, “ Evaluation of MU-MIMO digital beamforming algorithms in B5G/6G LEO satellite systems”, *2022 11th Advanced Satellite Multimedia Systems Conference and the 17th Signal Processing for Space Communications Workshop (ASMS/SPSC)*, Graz, Austria, 2022.

## 2.1 Notation

Throughout this thesis, unless stated otherwise, the utilized notation is as follows: vectors are represented as bold lowercase letters and matrices as bold uppercase letters.  $\mathbf{A}^\top$  and  $\mathbf{A}^H$  denote the transpose and the conjugate transpose of  $\mathbf{A}$ , respectively.  $\mathbf{A}_{i,:}$  and  $\mathbf{A}_{:,i}$  refer to the  $i$ -th row and the  $i$ -th column of matrix  $\mathbf{A}$ , respectively. Finally,  $\text{tr}(\mathbf{A})$  denotes the trace of matrix  $\mathbf{A}$ .

## 2.2 System architecture

We consider a single multi-beam LEO satellite at altitude  $h_{sat}$  providing connectivity to  $K$  uniformly distributed on-ground UEs by means of  $N_B$  beams, as illustrated in Fig. 2.1. In our system scenario, FFR is assumed and, thus, all beams use the same spectral resources. Notably, the such solution introduces substantial CCI from adjacent beams, thus necessitating the use of advanced interference management techniques, either at the transmitter-side, such as precoding and beamforming, or at the receiver, such as Multi-User Detection (MUD)(which is out of the scope of this work). In the context of NTN, a LEO satellite is required to continuously maintain a logical connection with a ground-based gNB. This connection is essential for providing connectivity and the necessary content to users on the ground, as well as for collecting all the signaling and information required to implement the beamforming schemes. The satellite can establish this link either through a direct connection to a ground-based gateway (GW) or by connecting to other LEO satellites within the constellation via ISLs; the latter

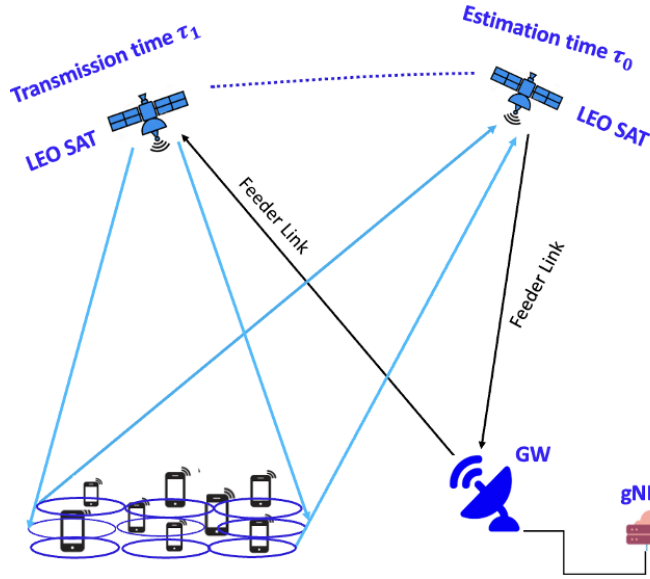


**Figure 2.1:** Single LEO satellite system architecture.

scenario will be explored in detail in the fifth chapter. The LEO satellite is presumed to implement digital beamforming techniques. These techniques, which will be explained in detail in the next chapter 3, necessitate the estimation of either the CSI or the locations of the users. As shown in Fig. 2.1, these estimates are computed by the users from known pilot signals at a generic time instant  $\tau_0$  in which the satellite is in a given orbital position. Then, the estimates are provided to the network entity for computing the beamforming coefficients, which in the following is assumed to be at the GW (or at the gNB to which the GW is directly connected). It is worth mentioning that when the satellite is no longer in the visibility of the GW, handover procedures are needed so as to switch the serving GW. For the sake of simplicity, only a single GW is assumed, without impacting the generality of this work. The calculated beamforming coefficients

are sent back to the satellite to be used in the beamforming scheme. As depicted in the architecture in Fig. 2.1, the satellite moved to a new position within its orbit. Hence, the actual beamformed transmission takes place at a time instant denoted as,  $\tau_1 = \tau_0 + \Delta\tau$ . The latency, represented as  $\Delta\tau$ , between the phase of estimating the channel or location and the phase of transmission, results in a misalignment between the channel on which the beamforming matrix is computed and the actual channel used for transmission. This misalignment affects the performance of the system. The latency  $\Delta\tau$  can be calculated as follows:

$$\Delta\tau = \tau_{ut,max} + 2\tau_{feeder} + \tau_p + \tau_{ad} \quad (2.1)$$

where: i)  $\tau_{ut,max}$  represents the maximum propagation delay for the UEs seeking the connectivity in the coverage area, i.e, on the user return link; ii)  $\tau_{feeder}$  denotes the delay on the feeder link, this factor is considered twice since the estimates are to be sent to the GW on the feeder downlink (DL) and then the beamformed symbols are sent back on the feeder uplink (UL) to the satellite<sup>3</sup>; iii)  $\tau_p$  refers to the processing delay needed to calculate the beamforming coefficients; and iv)  $\tau_{ad}$  represents any additional delay.

It is worth highlighting that the impact of the phase variation resulting from payload chains or different on-board Local Oscillators (LOs) can be controlled by adopting a configuration where a single stable oscillator acts as a common reference for individual frequency converters. This design is commonly utilized

---

<sup>3</sup>The same value is taken twice since the distance travelled by the satellite in the considered time intervals can be negligible.

in multibeam satellite architectures [53]. Notably, in case phase perturbations are modelled (e.g., as those introduced by scintillation), the following proposed algorithms might need some adjustments, in particular related to signalling and procedures. This is not considered in this work.

### 2.3 Antenna array model

The antenna array model is based on ITU-R Recommendation M.2101, [54]. The coordinate system for the Uniform Planar Array (UPA) is shown in Fig. 2.2. The planar array boresight direction is defined by the direction of the Sub Satellite Point (SSP).

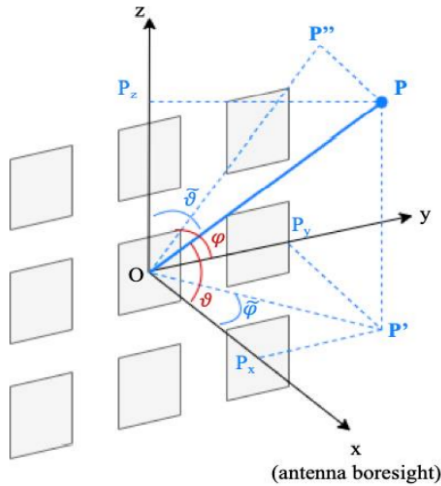


**Figure 2.2:** Coordinate system for the Uniform Planar Array model.

The center of the reference system is on-board the satellite at the center of the antenna array and  $\mathbf{P}$  denotes the position of the on-ground UT, identified by the direction  $(\tilde{\vartheta}, \tilde{\varphi})$ . In the following, we refer to the user direction in terms of the

$(\vartheta, \varphi)$  angles, in which the boresight direction is  $(0, 0)$  and that allows to easily derive the direction cosines for the considered user as follows:

$$u = \frac{P_y}{\|\mathbf{P}\|} = \sin \vartheta \cos \varphi \quad (2.2)$$

$$v = \frac{P_z}{\|\mathbf{P}\|} = \sin \vartheta \sin \varphi \quad (2.3)$$

We can express the array response of the UPA for the generic direction  $(\vartheta_i, \varphi_i)$  as the Kronecker product of the array responses of the 2 Uniform Linear Array (ULA) lying on the  $y$ - and  $z$ -axis [55, 56]. Let us first define the  $1 \times N_H$  Steering Vector (SV) of the ULA along the  $y$ -axis  $\mathbf{a}_H(\vartheta_i, \varphi_i)$  and the  $1 \times N_V$  SV of the ULA along the  $z$ -axis  $\mathbf{a}_V(\vartheta_i, \varphi_i)$ :

$$\mathbf{a}_H(\vartheta_i, \varphi_i) = [1, e^{jk_0 d_H \sin \vartheta_i \cos \varphi_i}, \dots, e^{jk_0 d_H (N_H - 1) \sin \vartheta_i \cos \varphi_i}] \quad (2.4)$$

$$\mathbf{a}_V(\vartheta_i, \varphi_i) = [1, e^{jk_0 d_V \sin \vartheta_i \sin \varphi_i}, \dots, e^{jk_0 d_V (N_V - 1) \sin \vartheta_i \sin \varphi_i}]. \quad (2.5)$$

In the above equations,  $k_0 = 2\pi/\lambda$  is the wave number,  $\lambda$  is the wavelength,  $(N_H, N_V)$  denote the number of array elements on the horizontal ( $y$ -axis) and vertical ( $z$ -axis) directions, respectively, with  $N = N_H N_V$ , and  $(d_H, d_V)$  denote the distance between adjacent array elements on the horizontal and vertical directions, respectively. We assume that the array is equipped with directive antenna elements, whose radiation pattern is denoted by  $g_E(\vartheta_i, \varphi_i)$ . Therefore, we can express the total array response, i.e., the  $(1 \times N)$  SV of the UPA at the satellite targeted for the  $i$ -th user as the Kronecker product of the 2 SV's along each axis

multiplied by the element radiation pattern:

$$\mathbf{a}(\vartheta_i, \varphi_i) = g_E(\vartheta_i, \varphi_i) \mathbf{a}_H(\vartheta_i, \varphi_i) \otimes \mathbf{a}_V(\vartheta_i, \varphi_i) \quad (2.6)$$

For the sake of clarity, it is worth providing the description of the 3-D radiation power pattern  $g_{E,\text{dB}}(\vartheta, \varphi)$  of each array antenna element at the satellite, [57, 58] which can be expressed in terms of vertical cut  $g_{E,\text{dB}}(\vartheta, \varphi = 0^\circ)$  and horizontal cut  $g_{E,\text{dB}}(\vartheta = 90^\circ, \varphi)$ . The vertical cut is obtained by fixing  $\varphi$  to  $0^\circ$ :

$$g_{E,\text{dB}}(\vartheta, \varphi = 0^\circ) = -\min \left\{ 12 \left( \frac{\vartheta - 90^\circ}{\vartheta_{3\text{dB}}} \right)^2, SLA_V \right\} \quad [\text{dB}] \quad (2.7)$$

with  $\vartheta_{3\text{dB}} = 90^\circ$ ,  $\vartheta \in [0^\circ, 180^\circ]$  and  $SLA_V = 30$  dB is the side-lobe attenuation in the vertical direction. The horizontal cut is obtained by fixing  $\vartheta$  to  $90^\circ$ :

$$g_{E,\text{dB}}(\vartheta = 90^\circ, \varphi) = -\min \left\{ 12 \left( \frac{\varphi}{\varphi_{3\text{dB}}} \right)^2, A_{\text{max}} \right\} \quad [\text{dB}] \quad (2.8)$$

with  $\varphi_{3\text{dB}} = 90^\circ$ ,  $\varphi \in [-180^\circ, 180^\circ]$  and  $A_{\text{max}} = 30$  dB is the maximum attenuation. The total 3-D radiation power pattern can be finally expressed as:

$$g_{E,\text{dB}}(\vartheta, \varphi) = G_{E,\text{max}} - \min \{ -(g_{E,\text{dB}}(\vartheta, \varphi = 0^\circ) + g_{E,\text{dB}}(\vartheta = 90^\circ, \varphi), A_{\text{max}}) \} \quad (2.9)$$

where  $G_{E,\text{max}}$  is the maximum directional gain of an antenna element and lastly,  $g_E(\vartheta, \varphi) = 10^{\frac{g_{E,\text{dB}}(\vartheta, \varphi)}{20}}$ .

## 2.4 Channel model

The CSI vector,  $\mathbf{h}_i = [h_{i,1}, \dots, h_{i,n}, \dots, h_{i,N}]$ , represents the channel between the  $N$  radiating elements and the generic  $i$ -th on-ground UE, with  $i = 1, \dots, K$ , and can be expressed as:

$$\mathbf{h}_i = G_i^{(rx)} \frac{\lambda}{4\pi d_i} \sqrt{\frac{L_i}{\kappa B T_i}} e^{-j \frac{2\pi}{\lambda} d_i} \mathbf{a}(\vartheta_i, \varphi_i) \quad (2.10)$$

where: i)  $d_i$  is the slant range between the  $i$ -th user and the satellite; ii)  $\kappa B T_i$  denotes the equivalent thermal noise power, with  $\kappa$  being the Boltzmann's constant,  $B$  the user bandwidth which is assumed to be the same for all users, and  $T_i$  the equivalent noise temperature of the  $i$ -th user receiving equipment; iii)  $L_i$  denotes the additional losses considered between the  $i$ -th user and the  $n$ -th antenna feed (e.g., atmospheric and antenna cable losses) and, for a single satellite, we can assume  $L_{i,n} = L_i, \forall n$ ; and iv)  $G_i^{(rx)}$  denotes the receiving antenna gain for the  $i$ -th UT. The additional losses, considered in our system model, are computed as:

$$L_i = L_{sha,i} + L_{atm,i} + L_{sci,i} + L_{CL,i} \quad (2.11)$$

where  $L_{sha,i}$  represents the log-normal shadow fading term,  $L_{atm,i}$  the atmospheric loss,  $L_{sci,i}$  the scintillation, and  $L_{CL,i}$  the Clutter Loss (CL), these terms are computed as per TR 38.811 [59] and 3GPP TR 38.821 [23]. Noting that the CL is included only in NLOS scenario.

Collecting all of the  $K$  CSI vectors, the system-level  $K \times N$  complex channel

matrix  $\mathbf{H}_{Sys}$  can be built as follows:

$$\mathbf{H}_{Sys} = \begin{bmatrix} \mathbf{h}_1 \\ \vdots \\ \mathbf{h}_k \\ \vdots \\ \mathbf{h}_K \end{bmatrix} = \begin{bmatrix} h_{1,1} & \cdots & h_{1,n} & \cdots & h_{1,N} \\ \vdots & \ddots & \vdots & & \vdots \\ h_{k,1} & \cdots & h_{k,n} & \cdots & h_{k,N} \\ \vdots & & \vdots & \ddots & \vdots \\ h_{K,1} & \cdots & h_{K,n} & \cdots & h_{K,N} \end{bmatrix} \quad (2.12)$$

where the generic  $i$ -th row contains the CSI vector of the  $i$ -th user and the generic  $n$ -th column contains the channel coefficients from the  $n$ -th on-board feed towards the  $K$  on-ground users. For each time frame, the Radio Resource Management (RRM) algorithm identifies a subset of  $K_{sch}$  users to be served, leading to a  $K_{sch} \times N$  complex scheduled channel matrix,  $\mathbf{H} = \mathcal{F}(\mathbf{H}_{Sys})$ , where  $\mathcal{F}(\cdot)$  denotes the RRM scheduling function, which is a sub-matrix of  $\mathbf{H}_{Sys}$ , i.e.,  $\mathbf{H} \subseteq \mathbf{H}_{Sys}$ , where  $\mathbf{H}$  contains only the rows of the scheduled users, i.e.,  $\mathbf{H} = [\mathbf{h}_1^\top | \mathbf{h}_2^\top | \cdots | \mathbf{h}_{K_{sch}}^\top]^\top$ , where the symbol  $|$  indicates horizontal concatenation.

## 2.5 MIMO beamforming in standalone LEO satellite scenario

In general, beamforming can be categorized based on:

1. The location where the beamforming/precoding matrix is applied on users' signals:
  - On-Ground Beamforming (OGBF): implemented at the ground control segment.

- On-Board Beamforming (OBBF): implemented on-board.
2. The signal space in which the beamforming/precoding matrix is calculated.
- Feed Space: when the channel coefficients between each on-board antenna feed and each user is available, the beamforming and precoding matrices can be jointly optimised to linearly combine the users' signals at feed level.
  - Beam space: in this scenario, the beamforming matrix is initially optimized to establish a predefined on-ground beam lattice based on coverage requirements. Subsequently, the precoding matrix is computed using the knowledge obtained by beamforming between each on-board equivalent antenna and each user to linearly combine the users' signals at the beam level.

In this thesis, we assume in the analysis only feed space beamforming. Fig. 3.3 depicts a block diagram of feed space beamforming, encompassing both OGBF and OBBF scenarios.

In the case of OGBF, the beamforming matrix is computed and applied to the users' signals at the ground segment, i.e., at the GW side. As a result, the precoded users' signals are transmitted on the feeder link, considering that each user is served with the entire beam bandwidth,  $B_{beams}$ . This implies that the signals of  $K_{sch}$  users are projected onto an  $N$ -dimensional space, leading to a bandwidth requirement on the feeder link given by  $NB_{beams}$  with OGBF.

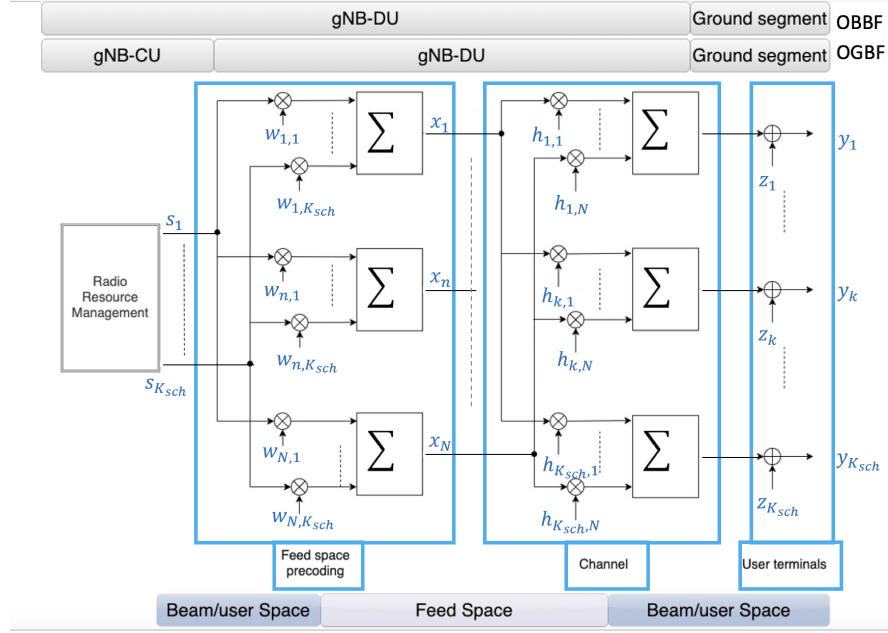


**Figure 2.3:** Block diagram of feed space beamforming considering OGBF and OBBF.

In the case of OBBF, the beamforming coefficients are computed at the GW, but their application to the users' signals is carried out on-board. As a result, there is a less stringent requirement in terms of bandwidth occupancy on the feeder link, as only the users' signals in their original  $K_{sch}$ -dimensional space are transmitted, leading to the required  $K_{sch}B_{beams}$  bandwidth. In the context of feed space beamforming, the considered beamforming algorithm calculates an  $N \times K_{sch}$  complex beamforming matrix  $\mathbf{W}$ , which projects  $K_{sch}$  dimensional column vectors,  $\mathbf{s} = [s_1, \dots, s_{K_{sch}}]^T$ , containing the unit-variance user symbols onto the  $N$ -dimensional space defined by the antenna feeds. In particular, from the on-board antenna feeds we transmit:

$$\mathbf{x} = \mathbf{W}_{\tau_0} \mathbf{s} \quad (2.13)$$

where  $\mathbf{x}$  is the  $N$ -dimensional vector of transmitted symbols from the antenna feeds, in which it can be noticed that the signal transmitted by the generic  $n_{th}$  antenna feed is a linear combination of the  $K_{sch}$  symbols intended for the scheduled users: The  $K_{sch}$ -dimensional vector of received symbols is:

$$\mathbf{y} = \mathbf{H}_{\tau_1} \mathbf{W}_{\tau_0} \mathbf{s} + \mathbf{z} \quad (2.14)$$

with  $\mathbf{z} = [z_1, \dots, z_k, \dots, z_{K_{sch}}]$ , where  $z_k$  is a circularly symmetric Gaussian random variable (r.v.) with zero mean and unit variance. The unit variance is motivated by observing that the channel coefficients in (2.10) are normalised to the noise power. It is important to observe that, the channel matrix  $\mathbf{H}_{\tau_0}$  is utilized to calculate the beamforming matrix during the estimation phase at the time instant  $\tau_0$ . However, the beamformed symbols are transmitted to the users at a different time instant,  $\tau_1$ , where the corresponding channel matrix is distinct and identified as  $\mathbf{H}_{\tau_1}$ . Finally, the signal received by generic  $k$ -th user can be expressed as follows:

$$y_k = \underbrace{\mathbf{h}_k \mathbf{W}_{:,k}}_{\text{intended}} s_k + \underbrace{\sum_{i=1, i \neq k}^{K_{sch}} \mathbf{h}_k \mathbf{W}_{:,i}}_{\text{interfering}} s_i + z_k \quad (2.15)$$

## 2.6 Key Performance Indicators (KPIs) of the system

Based on the received symbols, the KPIs of each scheduled user in each time frame can be obtained starting from the power transfer matrix as follows:

$$\mathbf{A} = |\mathbf{HW}|^2 \quad (2.16)$$

The power transfer matrix is a  $K_{sch} \times K_{sch}$  real matrix in which the generic  $a(i, k)$ -th element represents the power directed towards the  $i$ -th user and received, as interference, at the  $k$ -th terminal, normalised to the noise power. Thus, all of the diagonal elements of the power transfer matrix represents the useful powers to the intended users, while the sum of all of the off-diagonal elements on a given row corresponds to the interference experienced by that user, normalised to the noise power. Based on  $\mathbf{A}$ , it is possible to define the received Signal-to-Noise-Ratio (SNR) and the Interference-to-Noise Ratio (INR), as follows:

$$\begin{aligned} \text{SNR}_k &= a(k, k) \\ \text{INR}_k &= \sum_{i=1, i \neq k}^{K_{sch}} a(k, i) \end{aligned} \quad (2.17)$$

Then, the Signal-to-Interference Ratio (SIR), can be defined as the ratio between SNR and INR:

$$\text{SIR}_k = \text{SNR}_k / \text{INR}_k \quad (2.18)$$

From (2.17) and (2.15), the Signal-to-Interference-Plus-Noise-Ratio (SINR) can be computed as:

$$\text{SINR}_k = \frac{\text{SNR}_k}{1 + \text{INR}_k} = \frac{\|\mathbf{h}_k \mathbf{W}_{:,k}\|^2}{1 + \sum_{i=1, i \neq k}^{K_{sch}} \|\mathbf{h}_k \mathbf{W}_{:,i}\|^2} \quad (2.19)$$

Based on the aforementioned SINR, the spectral efficiency for serving each user in each time frame can be derived using either the Shannon bound formula (representing unconstrained capacity) or relying on the Modulation and Coding (Mod-Cod) scheme for the considered air interface. In the subsequent discussion, we adopt the unconstrained capacity approach, and thus the spectral efficiency is computed as follows:

$$\eta_k = \log_2(1 + \text{SINR}_k) \quad (2.20)$$

## **Chapter 3 - Benchmark Beamforming Schemes and Proposed SLNR Beamforming Scheme for NTN systems**

To address the potential co-channel interference associated with the FFR approach, the LEO satellite is assumed to implement linear beamforming schemes based on MU-MIMO focusing in this chapter on a standalone satellite scenario. Initially, the discussion of this chapter will focus on benchmark beamforming schemes, which are implemented based on the knowledge of CSI estimates, such as Zero-Forcing (ZF) and Minimum Mean Square Error (MMSE). Subsequently, the beamforming schemes based on the users' locations on ground, such as Multi-Beam (MB) and the analog Conventional Beamforming (CBF), will be presented. Thereafter, we design and propose the Signal-to-Leakage-plus-Noise Ratio (SLNR) beamforming scheme for a unicast approach of a LEO satellite, considering both Line Of Sight (LOS) and Non-Line Of Sight (NLOS) propagation scenarios. Finally, simulation results of the proposed scheme will be provided, comparing its performance with the aforementioned benchmark schemes in terms of the system KPIs, i.e., SINR and per-user spectral efficiency, demonstrating the superiority of the proposed scheme and its significant role in improving the performance of the considered NTN system.

The content of this chapter is based on the following published papers:

M.R. Dakkak, D. G. Riviello, A. Guidotti, A. Vanelli-Coralli, “Evaluation of multi-user multiple-input multiple-output digital beamforming algorithms in B5G/6G low Earth orbit satellite systems”, in *Int. J. Satell. Commun. Network.*, pp. 1-17, 2023.

M.R. Dakkak, D. G. Riviello , A. Guidotti, and A. Vanelli-Coralli, “ Evaluation of MU-MIMO digital beamforming algorithms in B5G/6G LEO satellite systems”, *2022 11th Advanced Satellite Multimedia Systems Conference and the 17th Signal Processing for Space Communications Workshop (ASMS/SPSC)*, Graz, Austria, 2022.

### 3.1 Benchmark beamforming algorithms

The MIMO beamforming schemes in NTN could be classified into two main categories based on the type of ancillary information utilized in computing the beamforming coefficients.

#### 3.1.1 CSI-based beamforming schemes

In this type of beamforming strategies, the estimation of CSI is required. These estimates are provided by the users to the on-ground gateway (in OGBF scenario) in order to compute the beamforming matrix. The CSI-based beamforming strategies considered in this work are: Zero Forcing (ZF) and the Minimum Mean Square Error (MMSE).

- **Zero Forcing (ZF):** the initial implementation of the ZF algorithm relies on the inversion of the channel matrix  $\mathbf{H}$ . Notably, this approach encounters numerical challenges as the  $\mathbf{H}^H\mathbf{H}$  matrix is often ill-conditioned, characterized by a very large condition number, leading to a close-to-singular matrix. In such cases, the computation of the inverse matrix is susceptible to significant numerical errors, resulting in a notable performance decline due to the inaccuracies in matrix inversion. To address this issue, we turn our attention to an alternative implementation of ZF as discussed in [60]:

$$\mathbf{W}_{ZF} = (\mathbf{H}^H\mathbf{H})^\dagger\mathbf{H}^H \quad (3.1)$$

where  $\dagger$  represents the Moore-Penrose pseudo-inverse matrix. It is worth highlighting that ZF scheme is susceptible to noise enhancement, leading to potential performance degradation in low SNR scenarios. This is because the scheme does not incorporate consideration for noise power in its formulation. This lack significantly affects its performance in NTN, as will be indicated in the subsequent section when presenting the numerical results.

- **Minimum Mean Square Error (MMSE):** MMSE beamformer, also known as Regularized Zero Forcing (RZF), is designed to solve the MMSE problem as follows:

$$\mathbf{W}_{MMSE} = \arg \min_{\mathbf{W}} \mathbb{E} \|\mathbf{H}\mathbf{W}\mathbf{s} + \mathbf{z} - \mathbf{s}\|^2, \quad (3.2)$$

for which the solution is given by:

$$\mathbf{W}_{MMSE} = (\mathbf{H}^H \mathbf{H} + \text{diag}(\alpha) \mathbf{I}_N)^{-1} \mathbf{H}^H \quad (3.3)$$

Here,  $\mathbf{H}$  is the estimated channel matrix and  $\alpha$  is a vector of regularization factors. Since the channel coefficients are normalized to the noise power, the optimal value of  $\alpha$  is given by  $\alpha = N/P_t$  [61], where  $P_t$  is the available transmitted power of the satellite. The equation above leads to a large dimension of the Gram matrix  $\mathbf{H}^H \mathbf{H}$ , containing  $N \times N$  coefficients. To address this, an alternative formulation that leads to a  $K_{sch} \times K_{sch}$  matrix,

is proposed in [62]:

$$\mathbf{W}_{MMSE} = \mathbf{H}^H (\mathbf{H}\mathbf{H}^H + \text{diag}(\alpha)\mathbf{I}_{K_{sch}})^{-1} \quad (3.4)$$

This formulation is computationally efficient since  $K_{sch} \ll N$ .

### 3.1.2 Location-based beamforming schemes

In this type of beamforming strategies, only the estimates of the users' locations are needed. These estimates are provided by the users to the on-ground gateway (in OGBF scenario) in order to calculate the beamforming matrix. We consider two location-based beamforming approaches: the switchable Multi-Beam (MB) scheme and the analog Conventional Beamforming (CBF) scheme.

- **The switchable Multi Meam (MB):** in this algorithm, as described in [63], beamforming vectors are computed in an approximated version. Specifically, a predefined codebook of beamforming vectors is generated through the following steps: i) spatially sampling the coverage area by defining a given beam lattice on the ground made of  $N_B$  beams; ii) identifying the beam center locations in terms of  $(u, v)$  coordinates denoted as  $\mathbf{c}_q$  for  $q = 1, \dots, N_B$  (as illustrated in Fig. 3.3); iii) computation the beamforming coefficients that are needed to form signals with the required spatial signatures, enabling the formation of beams in these specified directions. It is important to note that while this technique is implemented in the feed space, it still necessitates the definition of the beam lattice, aligning with

the beam space approach. The predetermined beamforming codebook is constructed as  $\mathbf{B} = [\mathbf{b}_1, \dots, \mathbf{b}_q, \dots, \mathbf{b}_{N_B}]$ , where each  $\mathbf{b}_q = \frac{1}{\sqrt{N}} \mathbf{a}(\vartheta_i, \varphi_i)$  comprises the  $N$ -dimensional beamforming vector responsible for steering the radiation pattern toward the center of the  $q$ -th beam. For the generic  $k$ -th user to be served, the relevant beamforming column vector within the beamforming matrix is chosen based on the column in the beamforming codebook that aligns with the closest beam center to the location of the  $k$ -th user, i.e.,

$$\mathbf{W}_{MB} = [\mathbf{W}_{:,1}, \dots, \mathbf{W}_{:,q}, \dots, \mathbf{W}_{:,N_B}] \quad (3.5)$$

with

$$\begin{aligned} \mathbf{W}_{:,k} &= \mathbf{B}_{:,j} \\ j &= \arg \min_{i=1, \dots, N} \|\mathbf{c}_i - \mathbf{p}_k\|^2 \end{aligned}$$

where  $\mathbf{c}_i$  is the center of the  $i$ -th beam and  $\mathbf{p}_k$  the position of the  $k$ -th user. It is noteworthy to highlight that the performance of the MB approach is impacted by the resolution of the spatial sampling. Specifically, a lower number of beams results in a larger approximation, leading to a degradation in performance. Lastly, it is important to observe that selecting one user per beam in each time frame results in  $K_{sch} = N_B$ . Nonetheless, this technique is considered as a short-term solution owing to its significant advantage of not requiring the CSI estimates.

- **Conventional Beamforming (CBF) scheme:** also referred to as beam steering, this method generates weights to create a phase shift that com-

compensates for the delay in the direction  $(\theta_i, \varphi_i)$  of the intended user. The weights can be represented as:

$$\mathbf{W}_{:,i} = \frac{1}{\sqrt{N_H N_V}} \mathbf{a}_H(\vartheta_i, \varphi_i) \otimes \mathbf{a}_V(\vartheta_i, \varphi_i) \quad (3.6)$$

Since the weights only consist of complex exponentials with equal amplitude, this is a fully analog beamforming scheme. Conventional Beamforming (CBF) is essentially a location-based technique, as the direction  $(\theta_i, \varphi_i)$  of the  $i$ -th user can be easily determined by knowing its location.

## 3.2 Proposed SLNR-based beamforming

### 3.2.1 Literature

The conventional approach to design an optimal MU-MIMO beamforming scheme typically involves maximizing the SINR for each user. However, this optimization problem is known to be challenging due to its coupled nature, and a closed-form solution does not yet exist. To address this issue, alternative beamforming schemes, such as the Signal-to-Leakage-plus-Noise Ratio (SLNR) are introduced. This scheme splits the interconnected optimization problem into a completely decoupled one. SLNR-based beamforming or precoding approach has been discussed in some studies and applications related to TN [64–67] and, more recently, in NTN [68–71]. For example, in [68], the SLNR metric was utilized to address Secure and Energy Efficient (SEE) beamforming in multibeam satellite systems. The authors in [69] investigated the secrecy performance of a cogni-

tive satellite terrestrial network, introducing a hybrid approach involving ZF and partial ZF to solve the optimization problem and obtain BF weight vectors in a closed form. In this study [71], it was investigated the design of a generalized SLNR (G-SLNR) beamformer for multigroup-multicast transmission, focusing on a single SLNR beamformer design for a group of users with similar channel coefficients, specifically targeting MEO satellite communication systems under clear sky propagation conditions.

### 3.2.2 Contribution

In this chapter, we design transmit beamforming vectors based on maximization of the figure of merit (SLNR) considering a unicast approach for single LEO satellite systems, taking into account both LOS and NLOS propagation scenarios. It is worth noting that, to the best of our knowledge, the proposed scheme has not been introduced before in the state of the art for NTN under the same assumptions regarding system and channel conditions and with the same objective. Furthermore, the movement of the satellite and UEs is considered in the analysis, which adds a further contribution in literature.

### 3.2.3 Mathematical definition

The power transfer matrix in (2.16) defines the CCI for a given user  $k$  as the interference caused by all other users, i.e.,  $\sum_{i,i \neq k} a(k, i)$ . On the other hand, the "leakage" refers to the interference that user  $k$  causes to all other users, i.e.,  $\sum_{i,i \neq k} a(i, k)$  and thus it measures the amount of leaking power from that user

to all other users sharing the same channel. As emphasized before, the problem of maximizing the SINR for all users in downlink beamforming is well-studied, and no closed-form solutions are available yet. In contrast, SLNR-based beamforming maximizes the SLNR for all users simultaneously, leading to a decoupled optimization problem with an analytical closed-form solution [72]. SLNR-based beamforming considers noise power in implementing beamforming vectors, unlike ZF scheme, and does not impose any dimension condition on the number of transmission/receiving antennas. Furthermore, SLNR beamforming can be classified as a regularized channel inversion scheme, with customized regularization factors for each user based on their operating SNR [73], whereas the MMSE scheme utilizes the same regularization factor for all users which is given by the inversion of the average SNR value for all users. Fig. 3.1 depicts the schematic of the signal leakage from user 1 to other users in a downlink multi-user scenario, where a standalone LEO satellite with  $N$  transmit antennas is deployed to serve  $K_{sch}$  scheduled users.

Considering equation (2.19), it can be observed that the power of the desired signal component for user  $k$  is given by  $\|\mathbf{h}_k \mathbf{W}_{:,k}\|^2$ . Simultaneously, the interfering power caused by the  $k$ -th user on the signal received by the generic  $i$ -th user is given by  $\|\mathbf{h}_i \mathbf{W}_{:,k}\|^2$ . Consequently, the quantity, a leakage for user  $k$ , is defined as the whole power leaked from this user to all other users, expressed as:

$$\sum_{i=1, i \neq k}^{K_{sch}} \|\mathbf{h}_i \mathbf{W}_{:,k}\|^2. \quad (3.7)$$

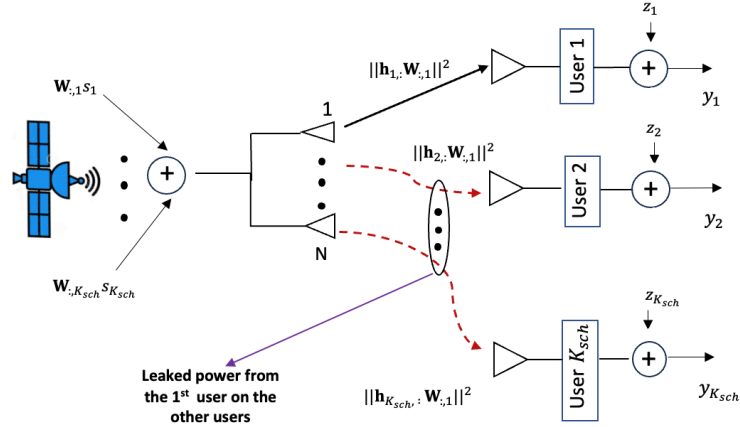


**Figure 3.1:** Block diagram depicting the leakage from user 1 on other users.

For the generic  $k$ -th user, the useful signal power  $\|\mathbf{h}_k \mathbf{W}_{:,k}\|^2$  is intended to be significantly larger than the noise power at its receiver, and in comparison to the power leaked from this user to all other scheduled users which is indicated in equation (3.7). Hence, based on these considerations, it can be introduced as a figure of merit in terms of SLNR:

$$\text{SLNR}_k = \frac{\|\mathbf{h}_k \mathbf{W}_{:,k}\|^2}{\beta + \sum_{i=1, i \neq k}^{K_{sch}} \|\mathbf{h}_i \mathbf{W}_{:,k}\|^2}. \quad (3.8)$$

For the sake of simplicity, the SLNR expression can be reformulated as:

$$\text{SLNR}_k = \frac{\|\mathbf{h}_k \mathbf{W}_{:,k}\|^2}{\beta + \|\mathbf{Z}_k \mathbf{W}_{:,k}\|^2} \quad (3.9)$$

where

$$\mathbf{Z}_k = [\mathbf{h}_1 | \cdots | \mathbf{h}_{k-1} | \mathbf{h}_{k+1} | \cdots | \mathbf{h}_{K_{sch}}]$$

is an extended channel matrix that excludes  $\mathbf{h}_k$  only (the vertical bar denotes a vertical concatenation), while  $\beta = \frac{K_{sch}}{P_t}$  denotes the SLNR regularization factor. The beamforming matrix aimed at maximizing SLNR for user  $k$  is provided by:

$$\hat{\mathbf{W}}_{:,k} = \arg \max_{\mathbf{W}} \text{SLNR}_k = \arg \max_{\mathbf{W}} \frac{\|\mathbf{h}_k \mathbf{W}_{:,k}\|^2}{\beta + \|\mathbf{Z}_k \mathbf{W}_{:,k}\|^2} \quad (3.10)$$

In [72], it is demonstrated that the optimal beamformer is associated with a closed-form solution of the generalized eigenvalue problem, given by:

$$\hat{\mathbf{W}}_{:,k} \propto \text{max eigenvector} \{ (\beta \mathbf{I} + \mathbf{Z}_k^H \mathbf{Z}_k)^{-1} \mathbf{h}_k^H \mathbf{h}_k \} \quad (3.11)$$

Regarding the eigenvector corresponding to the largest eigenvalue of the matrix  $(\beta \mathbf{I} + \mathbf{Z}_k^H \mathbf{Z}_k)^{-1} \mathbf{h}_k^H \mathbf{h}_k$ , denoted as  $\lambda_{\max}$ , the column vector  $\hat{\mathbf{W}}_{:,k}$  is selected according to (3.10). This choice results in the maximum SLNR value, expressed as:

$$\text{SLNR} = \lambda_{\max}$$

In the Table 3.1, we report the main pros and cons of all benchmark BF schemes as a comparison with respect to the proposed SLNR BF scheme.

### 3.3 Complexity analysis

The analysis of the beamforming complexity is fundamental for the practical deployment and optimization of the beamforming algorithms in NTN systems.

**Table 3.1:** Comparison of BF schemes

ZF	MMSE	MB	SLNR
<ul style="list-style-type: none"> <li>✓ Good performance in high SNR regime</li> </ul>	<ul style="list-style-type: none"> <li>✓ Good performance in both low and high SNR regime</li> </ul>	<ul style="list-style-type: none"> <li>✓ Doesn't require CSI knowledge, only users' locations</li> </ul>	<ul style="list-style-type: none"> <li>✓ Good performance in both low and high SNR regime</li> <li>✓ Uses a customized regularization factor for each user</li> </ul>
<ul style="list-style-type: none"> <li>✗ Noise enhancement in low SNR regime</li> <li>✗ Requires CSI knowledge</li> </ul>	<ul style="list-style-type: none"> <li>✗ Requires CSI knowledge</li> </ul>	<ul style="list-style-type: none"> <li>✗ Approximated scheme</li> <li>✗ Poor performance with a small number of beams</li> </ul>	<ul style="list-style-type: none"> <li>✗ Requires CSI knowledge</li> <li>✗ Computationally expensive (requires eigen-decomposition for each user)</li> </ul>

It facilitates the comparison of different beamforming schemes and the identification of trade-offs between complexity, applicability and performance. Hence, we provide a comparison between the proposed SLNR-BF scheme with respect to the ideal MMSE beamforming in terms of the complexity. We focused only on MMSE BF in the comparison since it is considered as the best performing BF technique in the literature, as we will see in the subsequent simulation results. The complexity of the SLNR BF algorithm is expressed as:  $O(K_{sch}N^2(P + K_{sch} + N + 1))$ , where  $P$  represents the number of iterations required to find the eigenvector associated with the largest eigenvalue, as indicated in (3.11) by using the power

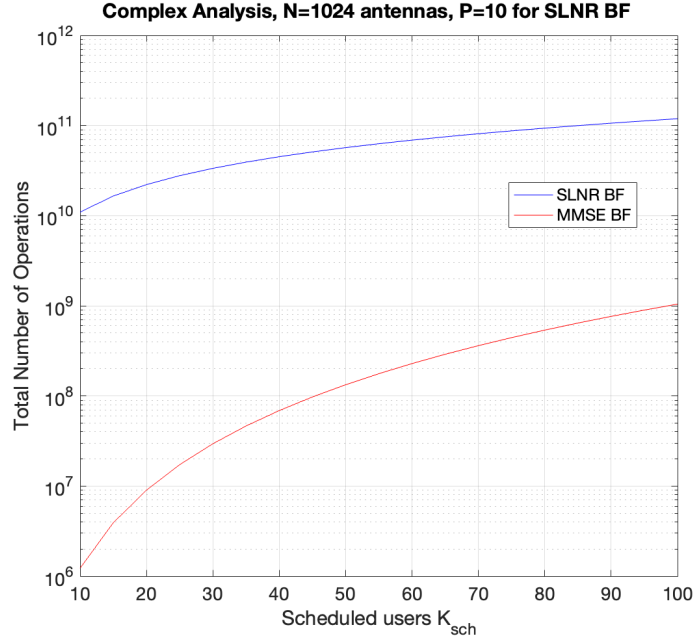


**Figure 3.2:** complexity analysis for SLNR and MMSE BF.

iteration algorithm. It is worth noting that such complexity includes: i) the whole matrix multiplications and inversions, i.e.,  $O(N^2(K_{sch} + N + 1))$  [74], and ii) the power iteration algorithm adds a complexity of  $O(PN^2)$  for each user [75]. Whereas the complexity of MMSE BF can be expressed as:  $O(K_{sch}^2 N(K_{sch} + 2))$ . In Fig. 3.2, we provide an analytical comparison in the complexity between SLNR and MMSE BF showing that the proposed SLNR BF scheme is computationally more expensive than MMSE BF as it requires eigen-decomposition for each user.

### 3.4 Power Normalization Algorithms

The power normalization process is a critical step in beamforming [76], ensuring that the power emitted by the satellite and each antenna is properly taken into account. Three options for power normalization are considered:

1. Sum Power Constraint (SPC): this approach imposes an upper bound on the total on-board power  $P_t$ , as follows:

$$\tilde{\mathbf{W}} = \frac{\sqrt{P_t} \mathbf{W}}{\sqrt{\text{tr}(\mathbf{W}\mathbf{W}^H)}} \quad (3.12)$$

Such normalization scheme preserves the orthogonality of the beamformer columns but does not guarantee an upper bound on the power transmitted from each feed. This may result in working in a non-linear regime.

2. Per-Antenna Power Constraint (PAC): the limitation is imposed per antenna with

$$\tilde{\mathbf{W}} = \sqrt{\frac{P_t}{N}} \text{diag} \left( \frac{1}{\|\mathbf{W}_{1,:}\|}, \dots, \frac{1}{\|\mathbf{W}_{N,:}\|} \right) \mathbf{W}. \quad (3.13)$$

However, the orthogonality in the beamformer columns here is disrupted.

3. Maximum Power Constraint (MPC) solution: This approach ensures that the power per antenna is upper bounded,

$$\tilde{\mathbf{W}} = \frac{\sqrt{P_t} \mathbf{W}}{\sqrt{N \max_j \|\mathbf{W}_{j,:}\|^2}}. \quad (3.14)$$

In this normalization, the orthogonality is preserved, but it may not exploit the entire available on-board power.

It is important to note that with the MB and the Conventional BF algorithm, the three normalization schemes lead to the same beamforming matrix, as the beamforming vectors are normalized by definition.

### 3.5 Numerical results

#### 3.5.1 Assumptions and System parameters

Before discussing the simulation results, we provide a general definitions of all the parameters related to the assumed standalone LEO satellite scenario according to ITU-R and 3GPP standardization.

1. *Satellite's related parameters*

- Satellite altitude: this refers to the height of the satellite above the ground level, denoted as  $h_{sat}$ .
- SSP coordinates: refer to the coordinates for the satellites' SSP, which include latitude and longitude.

2. *Satellite's antenna array*: we summarize the main parameters necessary for defining each satellite's on-board antenna array that have been discussed in the previous chapter.

- The number of radiating elements along the horizontal and vertical array axes is denoted by  $N_H$  and  $N_V$ , respectively.

- The horizontal and vertical spacing between elements is specified as  $d_H = 0.55\lambda$  and  $d_V = 0.55\lambda$ , where  $\lambda = c/f_c$  represents the signal wavelength.
- The half power beamwidth of a single element on the array's horizontal and vertical axis is given by  $\tilde{\vartheta}_{3dB} = 90^\circ$  and  $\tilde{\varphi}_{3dB} = 90^\circ$ , respectively.
- The front-to-back ratio on the array's horizontal and vertical axis is designated as  $A_m = 30$  dB and  $SLA_m = 30$  dB, respectively.
- The gain of the radiating element is  $G_{el}[dBi] = 5.3$  dBi.
- Satellite antenna gain: the maximum antenna gain obtained by the on-board array is defined as

$$G_{max}^{(tx)} = G_{el} + 10 \log_{10} N_H N_V \approx 35.4 \text{ dBi} \quad (3.15)$$

3. *UT antenna parameters*: Depending on type of the receiver, i.e, VSATs or handheld, the antenna parameters are determined based on TR 38.821 [77]. The total noise power at the receiver,  $P_N[dB]$ , can be computed in dB by the following equation:

$$P_N[dB] = N_f[dB] + 10 \log_{10} \left( T_0[K] + (T_a[K] - T_0[K])^{-0.1N_f[dB]} \right) \quad (3.16)$$

where  $T_0 = 290$  K represents the reference ambient temperature, and  $N_f$  denotes the noise figure. Table 3.2 presents the main antenna configuration parameters for both VSATs and handheld terminals [59]. These parameters

**Table 3.2:** Receiving antenna parameters.

Parameter	VSAT	Handheld
Antenna type	Directional	Omnidirectional
Polarisation	Circular	Linear
RX antenna gain $G_{max}^{(rx)}[dBi]$	39.7 dBi	0 dBi per element
Antenna temperature $T_a[K]$	159 K	290 K
Noise figure $N_f[dB]$	1.2 dB	7 dB

include the antenna type, polarization type, reception antenna gain value, temperature, and noise figure. It is worth mentioning that, throughout the thesis, VSATs are assumed in all simulation results.

4. *Beam lattice generation (parameters)*: To generate the beam lattice within the MB beamforming scheme, the beam radius is determined through the following process:

- A single beam is generated towards the Satellite’s SSP direction, denoted with the angle pair  $(\vartheta_{SSP}, \varphi_{SSP})$ .
- Based on the antenna model and MU-MIMO design discussed in the previous chapter, if we denote with the angle pair  $(\vartheta_i, \varphi_i)$  a generic  $i$ -th direction, the radiation pattern computed for the  $i$ -th direction

without beamforming is given by:

$$g^{(tx)}(\vartheta_i, \varphi_i) = \mathbf{1}^\top \mathbf{a}(\vartheta_i, \varphi_i) \quad (3.17)$$

where  $\mathbf{1}$  denotes a  $N_H N_V \times 1$  all-ones vector, while  $\mathbf{a}(\vartheta_i, \varphi_i)$  is computed as in (2.6).

- The  $N_H, N_V$ -dimensional unit-norm beamforming vector in the direction of the SSP  $(\vartheta_{\text{SSP}}, \varphi_{\text{SSP}})$ , is given by:

$$\mathbf{b} = \frac{1}{\sqrt{N_H N_V}} \mathbf{a}_H(\vartheta_{\text{SSP}}, \varphi_{\text{SSP}}) \otimes \mathbf{a}_V(\vartheta_{\text{SSP}}, \varphi_{\text{SSP}}) \quad (3.18)$$

- The radiation pattern calculated for the  $i$ -th direction, when beamforming is implemented to obtain a beam directed toward the SSP, can be written as:

$$g_{bf}^{(tx)}(\vartheta_i, \varphi_i) = \mathbf{b}^H \mathbf{a}(\vartheta_i, \varphi_i) \quad (3.19)$$

- The beamwidth,  $\vartheta_{edge}$ , which sets the radiation pattern value at the beam edge with respect to the beam center, is determined by finding the coordinates of the directions at which the above radiation pattern is  $(\Delta G_{edge} \text{ dB})$  below the value at the beam boresight direction as follows:

$$\{(u, v) : 20 \log_{10} |g_{bf}^{(tx)}| - G_{max}^{(tx)} \leq -\Delta G_{edge}\} \quad (3.20)$$

Subsequently, since many coordinates will satisfy this condition, the angle is obtained as the angle between the beam center direction SSP and the direction at which the value of  $20 \log_{10} \left| g_{bf}^{(tx)}(u, v) \right| - G_{max}^{(tx)}$  achieves the closest value to  $-\Delta G_{edge}$ . Once  $\vartheta_{edge}$  is known, the beam lattice is constructed using the procedure outlined in TR 38.821 [20]. It's noteworthy that, unless specified otherwise,  $\vartheta_{edge}$  is identified at  $\Delta G_{edge} = -3$  dB. Now, let us define the Adjacent Beam Spacing (ABS) in  $(u, v)$  coordinates as:

$$ABS = \sqrt{3} \sin \vartheta_{edge} \quad (3.21)$$

This value establishes the beam radius on the  $(u, v)$  plane, facilitating the generation of the desired hexagonal beam lattice with  $n_{tier}$  tiers.

As an illustrative example, assuming operation in the S-band with  $f_c = 2$  GHz and  $\lambda = 0.1499$  m, and utilizing the antenna model from the previous chapter with  $N_H = N_V = 32$ , the described procedure leads to  $\vartheta_{edge} = 1.4325^\circ$  and, consequently,  $ABS = 0.0433$ .

Fig. 3.3, shows an example of the beam lattice obtained with the explained procedure for a LEO satellite with SSP located at  $5.1863^\circ\text{E}$  and  $51.7757^\circ\text{N}$ , in which  $n_{tier} = 5$  tiers around the Sub-Satellite Point (SSP) are generated.

It is worth emphasizing that in the simulation results, the UEs are uniformly distributed with a density of  $0.5$  users/ $\text{km}^2$ , resulting in an average of  $K = 28500$  users to be served in each Monte Carlo iteration. The evaluation is performed

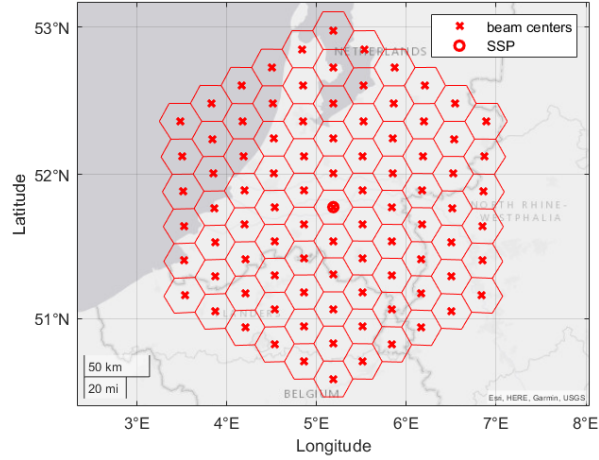


**Figure 3.3:** Beam lattice generated by LEO satellite in S-band.

under full buffer conditions, representing infinite traffic demand. Under these conditions, users are randomly scheduled using a position-based scheduler, in which each user is selected for each beam at each time frame. The total number of time frames is calculated to ensure that all users are served. In Table 3.3, we summarize the main simulation parameters of the standalone LEO satellite scenario.

### 3.5.2 Discussion and results

The numerical assessment is provided for SLNR-based beamforming and the performance is compared to the benchmark BF schemes, i.e, MMSE, ZF, and MB beamforming, assuming ideal CSI/location estimates at the transmitter side. Notably, the CBF is not considered in the simulation results of this chapter where it will be considered as location-based BF scheme in Chapters 4 and 5. It is worth highlighting that, when considering VSATs as a receiving terminals, we don't

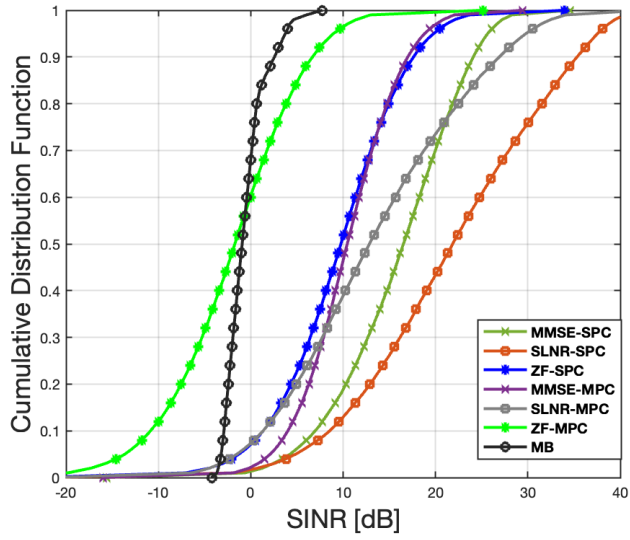
**Table 3.3:** Simulation parameters (proposed SLNR BF).

Parameter	Range
Operating band	S-band (2 GHz)
User bandwidth	30 MHz
Beamforming space	feed
Receiver type and scenario	Fixed VSATs, Travelling VSATs
Receiver speed, $\nu_{UE}$	(0, 250) km/h
Propagation scenario	LOS, NLOS
System scenario	urban
Total on-board power density, $P_{t,dens}$	(1,4,7) dBW/MHz
Number of tiers	5
Number of beams $S$	91
Number of scheduled users $K_{Sch}$	91
Number of transmitters $N$	1024 (32 $\times$ 32 UPA)
User density	0.5 user/km <sup>2</sup>

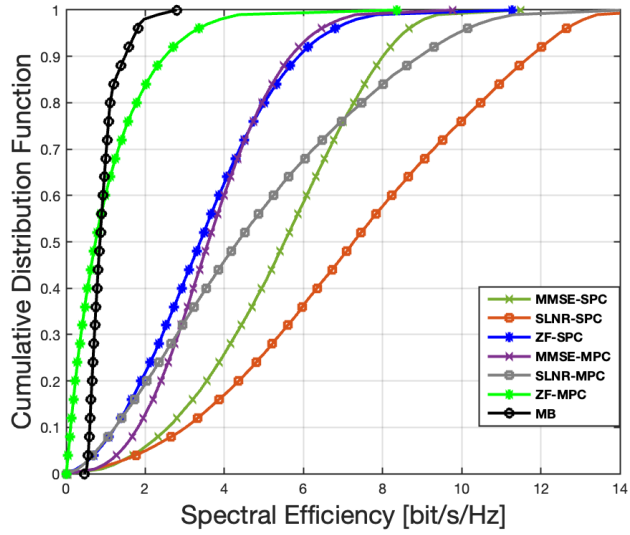
have any interference rejection advantages associated with the directive radiation pattern. This is because it is assumed that all UEs' antennas are directed towards a single satellite, with co-located antenna feeds on-board.

We first assume VSATs as fixed terminals and focus on LOS propagation scenario in an urban environment, in which the channel coefficients include free space loss, log-normal shadow fading, atmospheric loss, and scintillation according to TR 38.811 [59], and 3GPP TR 38.821 [77].

Fig. 3.4 shows the Cumulative Distribution Function (CDF) of the users' SINR and spectral efficiency for all the considered beamforming schemes with SPC and MPC normalization. The results demonstrate that the proposed SLNR-based beamforming outperforms MMSE, ZF and MB. Notably, ZF with SPC normalization exhibits superior performance compared to MB scheme. Additionally, it can be noticed that SPC normalization, for all schemes, is regarded as the most effective in terms of performance. However, SPC normalization does not ensure that each antenna element or feed does not exceed its allowed power emission limits. Therefore, MPC and PAC solutions may be preferred in this regard. However, comparing between MPC and PAC, it becomes evident that MPC performs significantly better, especially when the interference in the system is high, such as for large transmission power and VSAT terminals with high antenna gains. In such scenarios, maintaining the orthogonality between the columns in the beamforming matrix is crucial. Consequently, for all beamforming algorithms, PAC presents the worst performance. Hence, we focus in the analysis only on SPC and MPC for the power normalization. Figure 3.5 presents a comparative analysis of the spectral efficiency performance between SLNR and MMSE beamforming for various values of transmitted power density  $P_t = \{1, 4, 7\}$  dBW/MHz. Notably, doubling the transmitted power in the SLNR scheme yields a gain in the range of 0.7-0.8



(a) SINR.



(b) Spectral efficiency.

**Figure 3.4:** CDF of users' SINR and spectral efficiency for fixed VSATs in LOS scenario, at  $P_t = 4$  dBW/MHz.

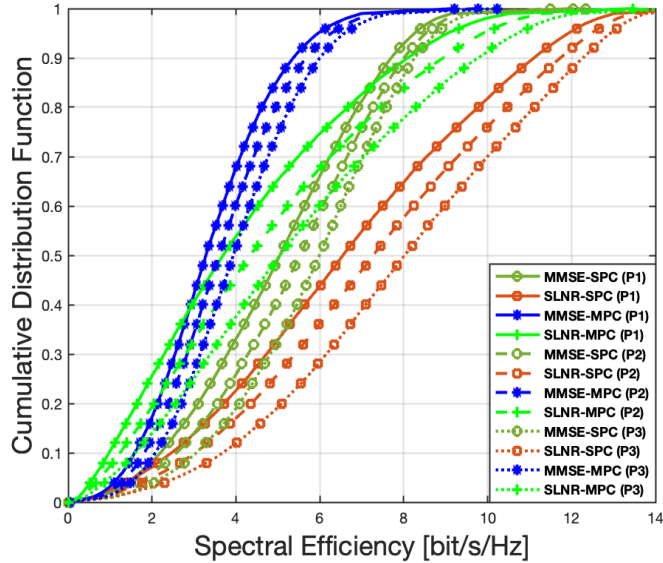
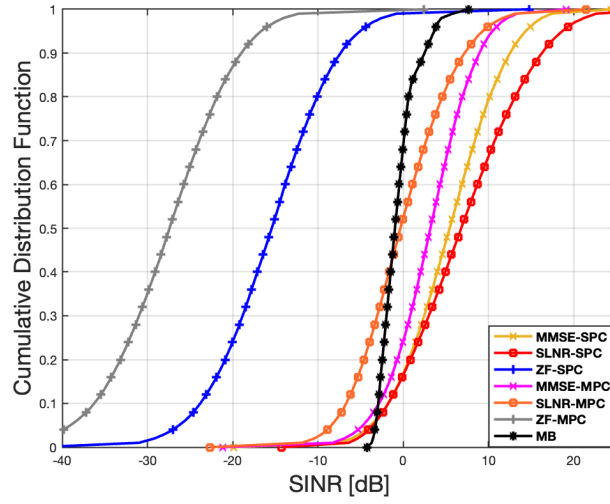


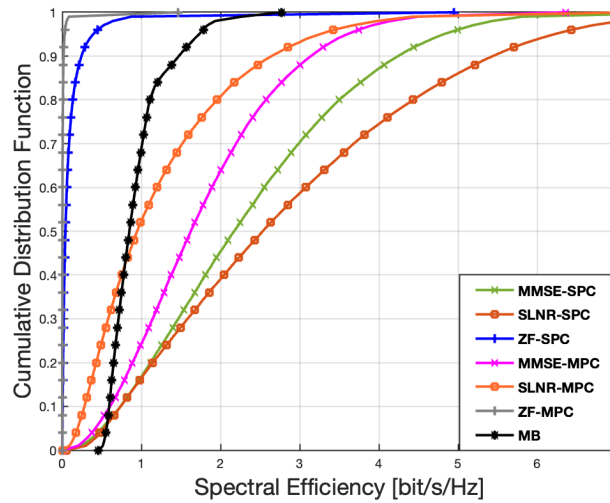
**Figure 3.5:** CDF of users' spectral efficiency for fixed VSATs in LOS scenario for SLNR and MMSE beamforming with different power density values,  $P_1 = 1$  dBW/MHz (solid line),  $P_2 = 4$  dBW/MHz (dashed line), and  $P_3 = 7$  dBW/MHz (dotted line).

bit/sec/Hz, while for MMSE, the gain is in the order of 0.35-0.45 bit/sec/Hz. These findings underscore the additional advantage and superior performance of the SLNR BF algorithm. In contrast, the situation is different for PAC, in which a higher transmission power results in worse spectral efficiency. This observation indicates a considerable sensitivity to the loss of orthogonality in the columns of the beamforming matrix in scenarios with increased interference.

Furthermore, by assuming NLOS propagation scenario in an urban environment, the users experience in addition to the impairments already present in LOS scenario, the Clutter Loss (CL), [59, 77]. The CDF of the users' SINRs and spectral efficiencies for all the evaluated beamforming schemes in NLOS scenario considering fixed VSATs are shown in Fig. 3.6. In NLOS scenario as well,



(a) SINR



(b) Spectral efficiency

**Figure 3.6:** CDF of users' SINR and spectral efficiency for fixed VSATs in NLOS scenario with  $P_t = 4$  dBW/MHz.

the SLNR-based beamforming scheme performs better than the optimal MMSE scheme, followed by MB. Notably, ZF exhibits poor performance due to its high

sensitivity to shadowing and clutter loss. Such superiority of the SLNR scheme in both LOS and NLOS scenarios demonstrates its robustness against different propagation conditions. It is worth emphasizing that the improved performance of SLNR-based beamforming with respect to MMSE-BF is motivated by the fact that SLNR utilizes a customized regularization factor for each user, while the MMSE scheme employs the same regularization factor for all users. This distinction is crucial in the presented NTN scenario, in which the users experience non-uniform and extremely fluctuating SNRs. Fig. 3.7 illustrates a significant degradation in performance under NLOS conditions compared to LOS scenarios. The spectral efficiency degradation is approximately 4-4.5 bit/s/Hz for SLNR-based beamforming (for both SPC and MPC), 3-4 bit/s/Hz for MMSE-SPC, and 1-2 bit/s/Hz for MMSE-MPC. This decline in performance is due to the challenges posed by NLOS conditions, highlighting the impact of the environment on the effectiveness of the different beamforming schemes.

Moreover, we extend the analysis to encompass not only fixed VSATs but also VSATs traveling at  $\nu_{UE} = 250$  Km/h as defined in 3GPP TS 22.261 [78]. Figure 3.8 presents the CDFs of the spectral efficiency for vehicular VSATs, considering all the beamforming schemes in both LOS and NLOS scenarios. The results indicate once again that the SLNR beamforming outperforms MMSE, followed by MB and ZF beamforming schemes. Finally, as previously described in the system model, all beamforming coefficients are calculated based on the channel matrix estimated at time instant  $\tau_0$ , while transmission takes place at time instant  $\tau_1$ , when the satellite has moved in its orbit to a new position. Table 3.4 presents

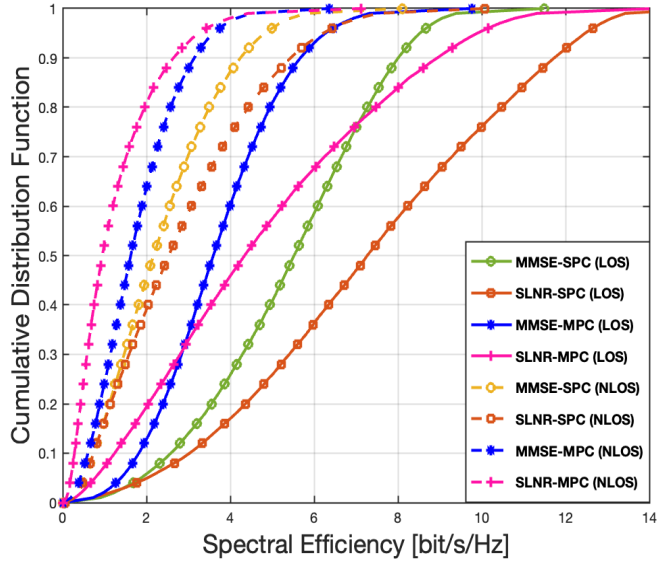
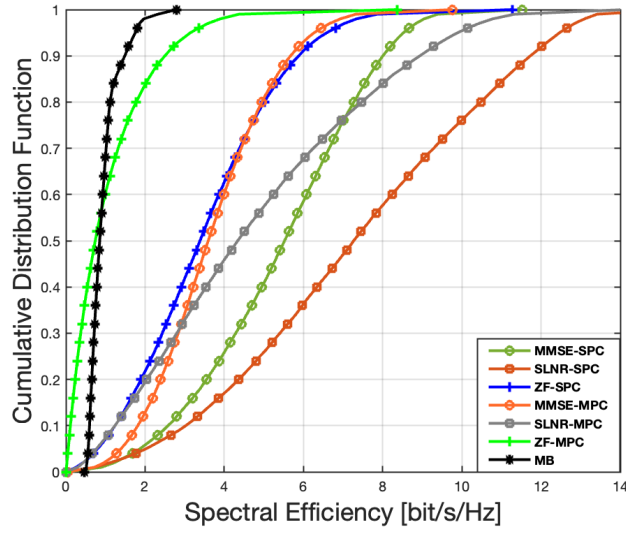
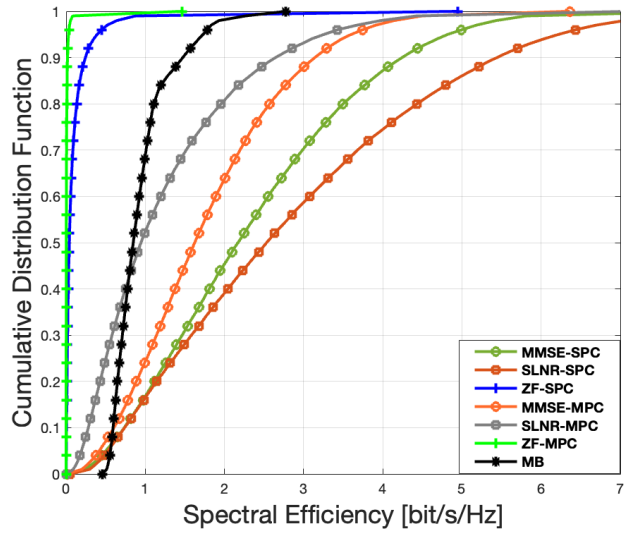


**Figure 3.7:** CDF of users' spectral efficiency for fixed VSATs and MMSE/SLNR beamforming schemes with  $P_t = 4$  dBW/MHz in LOS scenario (solid line) and NLOS scenario (dashed line).

a performance comparison of the beamforming schemes between our scenario (CSI estimation with channel aging) and the genie-aided CSI estimation scenario, where the channel coefficients can be estimated and transmitted simultaneously. From the average SINR and spectral efficiency values in Table 3.4, a minimal degradation in performance is observed compared to the genie-aided CSI case. Specifically, for SLNR-SPC, the average SINR experiences a degradation of 1.18 dB, and for MMSE-SPC, it is degraded of 1.22 dB. However, we will discuss the channel aging issue and the possible technologies to mitigate it in Chapters 5 and 6.



(a) LOS



(b) NLOS

**Figure 3.8:** CDF of users' spectral efficiency for vehicular VSATs and all considered BF schemes in LOS and NLOS scenarios with  $P_t = 4$  dBW/MHz.

**Table 3.4:** Average performance of BF schemes in case of CSI estimation with channel aging vs. genie-aided CSI estimation.

KPIs	BF Schemes					
	Genie-aided CSI					
	SLNR-SPC	SLNR-MPC	MMSE-SPC	MMSE-MPC	ZF-SPC	ZF-MPC
SINR [dB]	22.97	13.80	17.17	11.36	9.92	-1.92
Rate [bit/s/Hz]	7.71	4.84	5.80	3.93	3.49	0.84

---

KPIs	CSI with channel aging					
	SLNR-SPC	SLNR-MPC	MMSE-SPC	MMSE-MPC	ZF-SPC	ZF-MPC
SINR [dB]	21.79	13.48	15.95	10.47	9.56	-1.96
Rate [bit/s/Hz]	7.32	4.75	5.41	3.69	3.50	1.1

### 3.6 Conclusions

In this chapter, we introduced and evaluated MU-MIMO beamforming algorithms for a standalone LEO scenario. Furthermore, we proposed SLNR beamforming for NTN systems, which addresses the challenge of joint optimization between beamforming vectors by splitting it into multiple separate optimization problems for the targeted users. We performed a comparative analysis with benchmark algorithms, including both CSI-based (MMSE and ZF) and location-based beamforming (MB). The numerical results demonstrated the superior performance of SLNR beamforming in terms of spectral efficiency and SINR, outperforming MMSE, MB, and ZF beamforming schemes in both LOS and NLOS

condition scenarios. The assessment considered the satellite's movement with both fixed and moving or travelling VSATs, showing a performance degradation when transitioning from LOS to NLOS propagation scenarios. Regarding normalizations, SPC approach proved the best performance across all beamforming algorithms, followed by MPC one, while PAC provided the worst performance. Moreover, a slight improvement for the SLNR BF with respect to the MMSE BF was observed when increasing the same amount of the transmitted power density.

## Chapter 4 - LFOV Planar Subarrayed Architecture with Beamforming in NTN Systems

In this chapter, we first provide the state of the art on subarrays antenna architecture and then we propose the LFOV subarrays with CSI/location-based beamforming on-board in standalone satellite scenario. Thereafter, we discuss the mathematical description of the proposed scheme and the main assumptions of the system model. Finally, simulation and numerical results of the proposed scheme will be provided, comparing its performance with the benchmark beamforming design without subarraying in terms of the system KPIs, demonstrating the superiority of the proposed scheme and its significant role in improving the performance of the considered NTN system.

The content of this chapter is based on the following published paper:  
M. R. Dakkak, D. G. Riviello, A. Guidotti and A. Vanelli-Coralli, “Assessment of Beamforming Algorithms with Subarrayed Planar Arrays for B5G/6G LEO Non-Terrestrial Networks”, *European Wireless 2023; 28th European Wireless Conference*, Rome, Italy, 2023.

## 4.1 State of the art on subarrays

In [79], the authors presented a comprehensive review of recent advancements in antenna technology that have facilitated the commercial applications of planar arrays in NTN. While phased arrays have demonstrated notable benefits in terms of compactness, electronic steering, and rapid reconfigurability compared to the conventional solutions, such as reflector antennas, certain challenges are still present. These challenges include the affordability of the antenna, its robustness, the complexity of the Beamforming Network (BFN), power efficiency, and the increasing demand for a greater number of antenna elements to meet the requirements of evolving B5G and the future 6G systems. One of the main solutions, to address such issues related to the cost and complexity, is the subarrayed configuration [80, 81], i.e., a partition of the larger planar array into smaller planar arrays. This partitioning is crucial to achieve specific design goals such as providing more degrees of freedom (DoF), alleviate the hardware complexity, and improve system performance. Subarrayed configuration is presented in the literature of TN [82–85] and NTN [86, 87]. For instance, in [88], the authors proposed a novel beamforming architecture based on phased subarrays for TN. This study showed that subarrays, when properly combined at the user locations, provide relatively high gains towards the intended users and sufficiently low inter-user interference levels. In [89], the authors introduced a design of beamforming algorithms for MU-MIMO communications in LEO satellite systems utilizing multiple subarrays, in which each radio frequency (RF) chain drives one subarray allowing

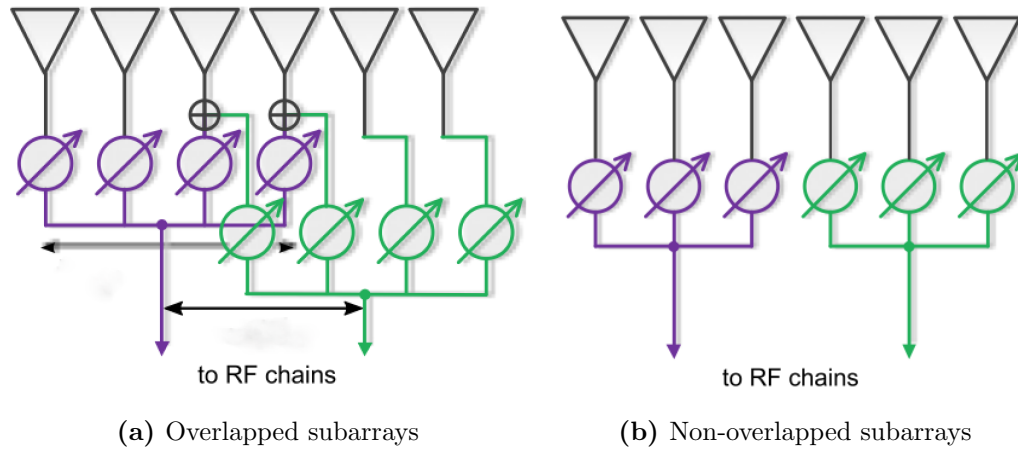


**Figure 4.1:** Categories of subarrays architecture [82].

the reduction in the number of beamforming ports and, consequently, relaxing the on-board processing requirements. An array of subarrays can be classified into two main categories of architecture, according to [90], as:

- Non-overlapped architecture: each RF chain is connected to a separate subset of antenna elements.
- Overlapped architecture: each RF chain is connected to a subset of antenna elements, that overlaps with other subsets.

Fig 4.1 provides an example of an overlapped and non-overlapped subarrays architecture. Regarding the beamforming with subarrayed configuration, two different categories can be distinguished based on the level of the beamforming implementation [91], i.e.,

- **beamforming at element level:** when beamforming is applied at element level, it means that the phase and/or amplitude of the individual antenna

elements within the subarray are adjusted to steer the beam towards a specific direction. Such implementation increases the complexity of the system, as it requires precise control over each element and thus it can lead to higher system complexity and cost, especially for large-scale phased arrays.

- **beamforming at subarray level:** it involves adjusting the phase and/or amplitude of the combined output of the subarray to achieve the desired beam pattern. It reduces system complexity by grouping elements into subarrays compared to the design at element level, especially for large arrays. Moreover, it can be considered as a solution to reduce the number of phase shifters or RF chains, which are essential components in phased array antennas, leading to cost savings.

This type of configuration is also known as Limited Field Of View (LFOV) array as it utilizes a very narrow steering range. In [92], the LFOV architecture is introduced, in which subarrays can be placed at a spacing larger than half of the wavelength to reduce the angular steering range and simultaneously increase the directivity within the same range. When spacing is larger than half of the wavelength, grating lobes arise, nevertheless, they will appear outside the narrow steering range and thus will not impact the performance in this type of applications.

### 4.1.1 Contribution

The main contribution of this chapter to the literature of NTN, is proposing MU-MIMO based on CSI/location beamforming schemes incorporated with LFOV architecture of non-overlapped subarrays on-board of standalone LEO satellite scenario. By comparing the proposed scheme to the reference design in the literature, we proved the superiority of the proposed scheme in terms of system level performance while emphasizing that the number of RF chains for both scenario, i.e, the reference and proposed one, is the same. Hence, no costs added related to RF chains. Furthermore, we consider the movement of the satellite as a further novelty.

## 4.2 Mathematical model

In the analysis of this chapter, we extend and develop the previous system model which is thoroughly explained in Chapters 2 and 3, by implementing LFOV subarrays on-board of LEO satellite in standalone satellite scenario. With reference to the planar array geometry shown in Fig. 2.2, we can express the overall array response of the UPA made of subarrays in the direction  $(\vartheta_i, \varphi_i)$  for user  $i$  as the Kronecker product between the two array responses of the Uniform Linear Arrays (ULAs) lying on the  $y$ -axis and  $z$ -axis. Let us first define the  $1 \times N_H$  Steering Vector (SV) of the ULA along the  $y$ -axis,  $\mathbf{a}_H(\theta_i, \varphi_i)$ , and the  $1 \times N_V$  SV of the ULA along the  $z$ -axis,  $\mathbf{a}_V(\theta_i)$  [93]:

$$\mathbf{a}_H(\vartheta_i, \varphi_i) = \left[ 1, e^{jk_0 M_H d_H \sin \vartheta_i \cos \varphi_i}, \dots, e^{jk_0 M_H d_H (N_H - 1) \sin \vartheta_i \cos \varphi_i} \right] \quad (4.1)$$

$$\mathbf{a}_V(\vartheta_i, \varphi_i) = \left[ 1, e^{jk_0 M_V d_V \sin \vartheta_i \sin \varphi_i}, \dots, e^{jk_0 M_V d_V (N_V - 1) \sin \vartheta_i \sin \varphi_i} \right] \quad (4.2)$$

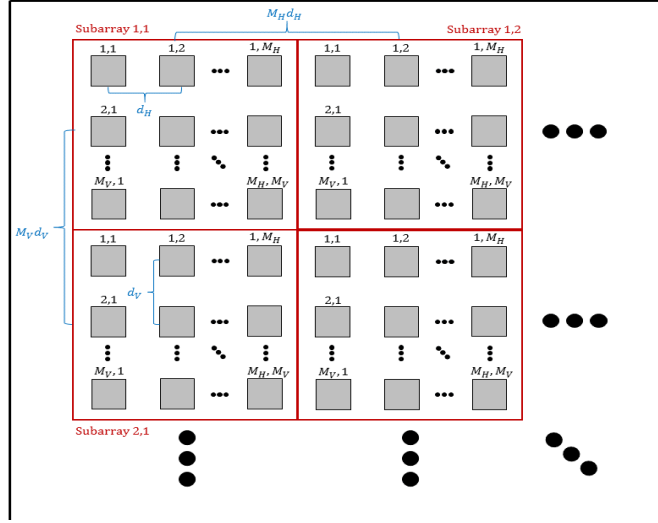


**Figure 4.2:** Structure of the subarrayed UPA on board of a single NTN node.

where  $k_0 = 2\pi/\lambda$  is the wave number,  $N_H, N_V$  denote the number of subarrays on the horizontal and vertical directions, respectively, with  $N = N_H N_V$ , and  $M_H, M_V$  denote the number of antenna elements per each subarray on the horizontal ( $y$ -axis) and vertical ( $z$ -axis) directions, respectively, with  $M = M_H M_V$ , and finally  $d_H, d_V$  denote the distance between adjacent antenna elements on the horizontal and vertical directions, respectively, as shown in Fig. 4.2.

It is worth mentioning that the total number of antenna elements are  $N_{tot} = MN$ , where  $M = 1$  if subarraying is not implemented. We can define the total steering vector of the full UPA (an array equipped with subarrays as antenna elements) as the Kronecker product of the 2 SV's along each axis:

$$\mathbf{a}_{UPA}(\vartheta_i, \varphi_i) = \mathbf{a}_H(\vartheta_i, \varphi_i) \otimes \mathbf{a}_V(\vartheta_i, \varphi_i). \quad (4.3)$$

We assume that the satellite is equipped with directive antenna elements (as previously assumed in Sec. 2.3), and the radiation pattern of each element is denoted by  $g_E(\vartheta_i, \varphi_i)$  according to Table 3 in [54]. These elements are grouped in  $N$  subarrays of size  $M_H \times M_V$ . It is worth recalling that a LFOV array has neither steering nor beamforming capabilities at antenna element level, but only at subarray level; for this reason, the linear phase shifts of the SVs in (4.1) and (4.2) are taken with respect to the center of each subarray. We can define the subarray factor  $F_{sub}(\vartheta_i, \varphi_i)$  as:

$$F_{sub}(\vartheta_i, \varphi_i) = \frac{\sin\left(\frac{M_H}{2}k_0d_H \sin \vartheta_i \cos \varphi_i\right)}{\sqrt{M_H} \sin\left(\frac{1}{2}k_0d_H \sin \vartheta_i \cos \varphi_i\right)} \frac{\sin\left(\frac{M_V}{2}k_0d_V \sin \vartheta_i \sin \varphi_i\right)}{\sqrt{M_V} \sin\left(\frac{1}{2}k_0d_V \sin \vartheta_i \sin \varphi_i\right)}. \quad (4.4)$$

Finally, we can express the total SV of the UPA of subarrays made of directive antenna elements at the satellite targeted for the  $i$ -th user as the product between the full UPA  $\mathbf{a}_{UPA}(\vartheta_i, \varphi_i)$ , the element radiation pattern, and the subarray factor:

$$\mathbf{a}(\vartheta_i, \varphi_i) = g_E(\vartheta_i, \varphi_i)F_{sub}(\vartheta_i, \varphi_i) \mathbf{a}_{UPA}(\vartheta_i, \varphi_i). \quad (4.5)$$

It is worth highlighting that the same assumptions related to the movement of the satellite and general system architecture, depicted in Fig. 2.1, are considered. Furthermore, we consider the same channel model expressed in this equation(2.10) in Chapter 2. However, the main difference here is the new steering vector generated by the proposed LFOV subarrays architecture.

### 4.3 Numerical Assessment

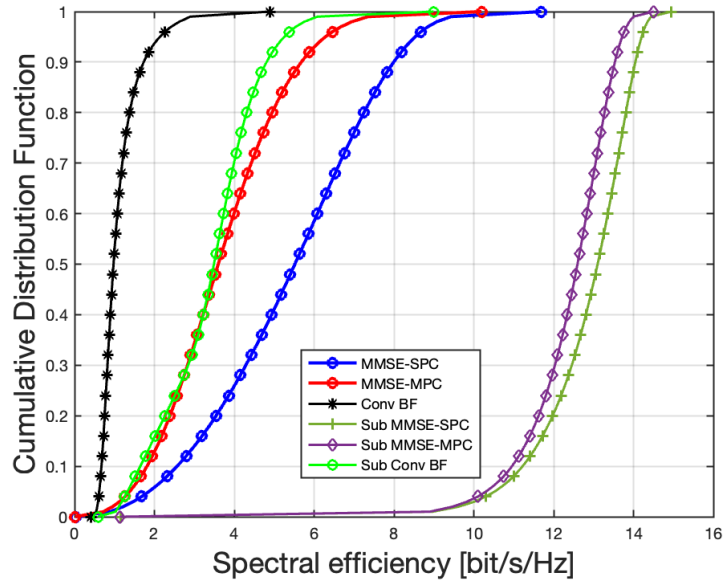
We present the numerical results of the evaluation based on the parameters listed in Tab. 4.1. The outcomes of the simulation are reported by means of the CDFs of the spectral efficiency of the users. Assuming fixed positions of UEs, they are uniformly distributed with a density of 0.5 users/Km<sup>2</sup>. This density translates to an average number of users  $K = 28500$  to be served for each Monte Carlo iteration.

Based on these premises, the users are scheduled based on their location. Specifically, a beam lattice is generated on ground only for scheduling purposes, as shown in Fig. 3.3, and a single user is randomly selected for each beam at each time slot; the total number of time slots is determined to ensure that every user is served at least once, as assumed previously in the results of chapter 3. Based on the coverage area shown in Fig. 3.3, it is possible to compute the minimum elevation angle, i.e., for a user at the edge of the coverage area, which is equal to 76°. This corresponds to a angular steering range for the array  $\Delta\vartheta = \Delta\varphi = 28^\circ$  in both angular directions, which justifies the use of a LFOV array. The analysis is provided for subarrayed MMSE and CBF beamforming schemes and then the performance is compared to the benchmark beamforming design without subarraying. In order to have a fair comparison, the transmitted power in case of subarrayed BF has been divided by  $(M_H M_V)$ , i.e., the maximum achievable subarray gain, so that the Effective Isotropic Radiated Power (EIRP) for both subarrayed and non-subarrayed cases shall be equivalent. Since the LFOV ar-

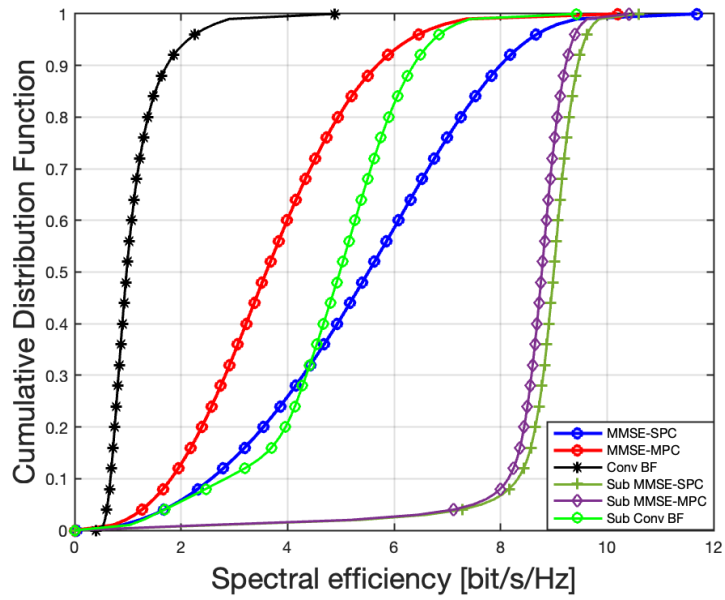
**Table 4.1:** System Configuration Parameters (proposed LFOV architecture)

Parameter	Value
Carrier frequency	S-band (2 GHz)
User bandwidth	30 MHz
Beamforming space	feed
Receiver type	fixed VSATs
Channel model	LOS
Propagation scenario	urban
Total on-board power density $P_{t,\text{dens}}$ without subarraying	4 dBW/MHz
Total on-board power density with subarraying	$P_{t,\text{dens}} - 10 \log_{10}(M_H M_V)$
Number of scheduled users $K_{sch}$	91
Number of subarrays $N$	1024 ( $32 \times 32$ )
Number of elements per each subarray $M$	$(2 \times 2)$ , $(3 \times 3)$ , $(4 \times 4)$
Number of antenna elements without subarraying $N_{tot} = N$	1024
Number of antenna elements with subarraying $N_{tot} = MN$	4096, 9216, 16384
User density	0.5 user/km <sup>2</sup>
Minimum elevation angle of the coverage area	76°
Angular scanning range ( $\Delta\vartheta = \Delta\varphi$ )	28°

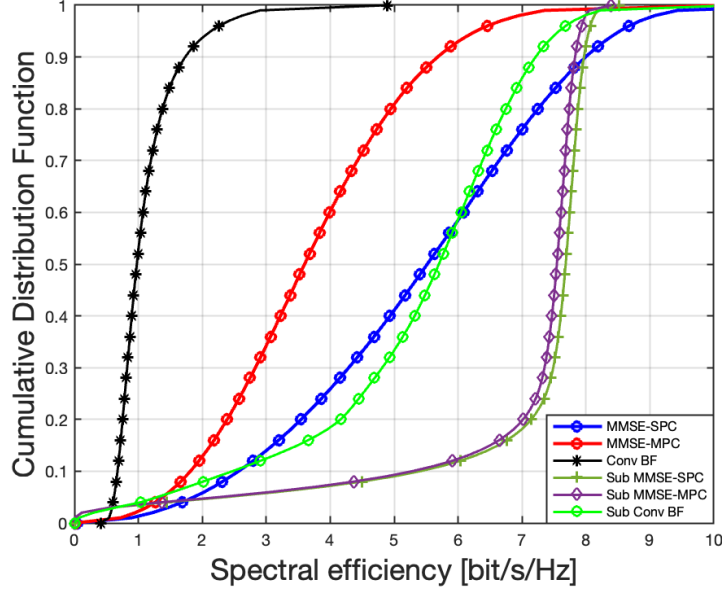
ray has no steering capability at antenna element level, it is worth mentioning that no hybrid beamforming is taken into account in this analysis, only digital beamforming, e.g. MMSE BF scheme or analog beamforming, e.g., CBF scheme.



(a) Subarray  $2 \times 2$



(b) Subarray  $3 \times 3$



(c) Subarray  $4 \times 4$

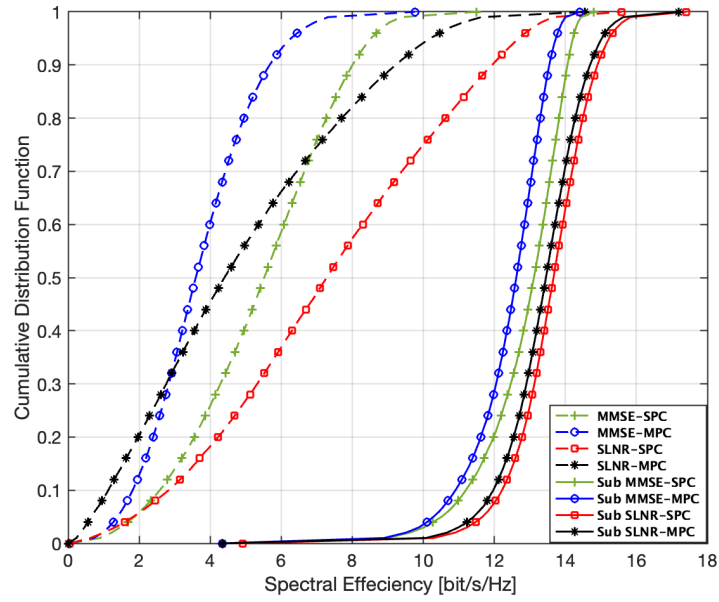
**Figure 4.3:** CDF of VSATs' spectral efficiency considering MMSE and CBF BF schemes.

We suppose LOS propagation scenario in urban environment. Fig. 4.3 shows the CDF of spectral efficiency of the users considering MMSE and CBF beamforming schemes with SPC and MPC normalization and three different dimensions of subarrays are considered, i.e.,  $2 \times 2$ ,  $3 \times 3$  and  $4 \times 4$ . It can be noticed, in Fig. 4.3a, that the proposed BF configuration with  $2 \times 2$  subarrays outperforms the BF design without subarraying for optimal MMSE followed by CBF. SPC performs better than MPC normalization since the latter does not exploit the whole available on-board power. In Fig. 4.3b, with subarray  $3 \times 3$ , we get a gain in the rate for MMSE-SPC in the order of 3.5 bit/sec/Hz, for MMSE-MPC in the order 5 bit/sec/Hz and for CBF in the order 3.5-4 bit/sec/Hz; whereas, in

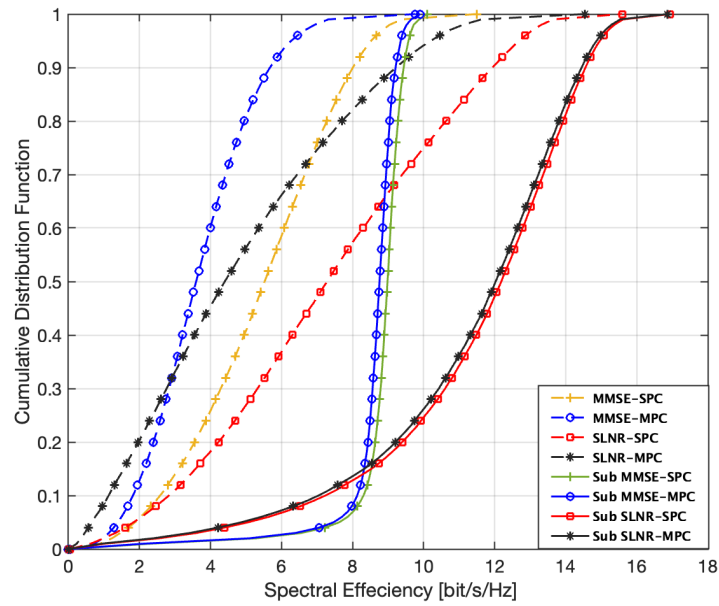
Fig. 4.3c, with subarray  $4 \times 4$ , we obtain a gain in the rate for MMSE-SPC in the order of 1.7-2 bit/sec/Hz, for MMSE-MPC in the order 3-4 bit/sec/Hz and for CBF in the order 4-4.5 bit/sec/Hz. It is worth noting that the analog CBF with  $3 \times 3$  and  $4 \times 4$  subarray configuration can clearly outperform the digital MMSE with MPC normalization with no subarrays, while the performance of analog CBF with  $4 \times 4$  subarray configuration and digital MMSE-SPC with no subarrays are very similar. Tab. 4.2 details the average values of the KPIs including SINR, SIR, SNR, INR, the rate and the relative gain (percentage) with subarrays compared to the benchmark of the considered BF schemes, taking into account different dimensions of subarrays. The superiority of the subarrayed configuration over the non-subarrayed one for both MMSE and CBF is motivated by the capability of an LFOV arrays to have high directivity as they produce narrower beams over the service area. Consequently, such high directivity enhances the interference mitigation capability of the proposed beamforming techniques. Furthermore, by observing Figs. 4.3a, 4.3b, 4.3c, and Tab. 4.2, it can be observed that the  $2 \times 2$  is the best configuration for MMSE, while for larger subarray configurations, the loss of SNR due to the reduction in angular scanning range becomes predominant factor; while for CBF, the  $4 \times 4$  configurations exhibits the best performance as it shows the highest interference rejection capability (highest SIR and lowest INR), as shown in the table Tab. 4.2. To conclude the analysis of this chapter, we also assess the performance of SLNR BF with subarrays for both SPC and MPC normalization and compared its performance with the optimal MMSE BF. Fig. 4.4 shows the CDF of the spectral efficiency of the users considering

**Table 4.2:** Performance of BF with subarraying  $M_H \times M_V$ .

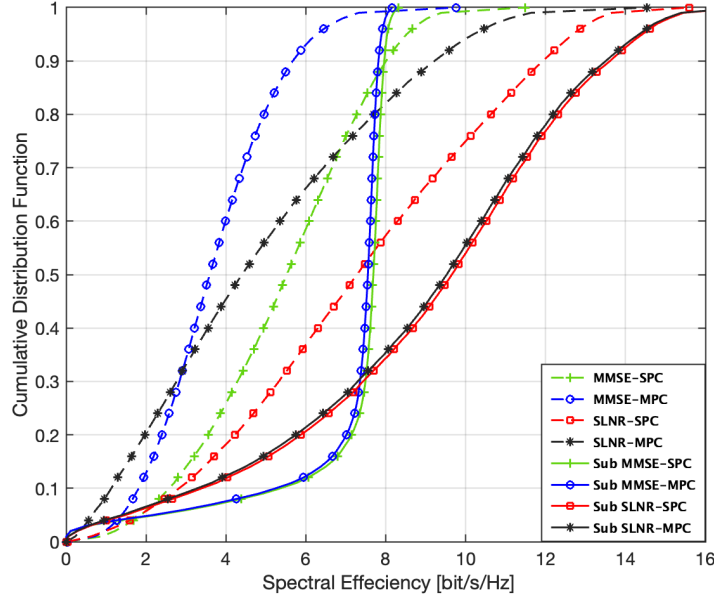
BF Scheme	KPIs					
	SINR	SIR	SNR	INR	Rate	
	[dB]	[dB]	[dB]	[dB]	[bits/sec/Hz]	Relative gain [%]
	Without Subarrays					
MMSE-SPC	15.93	18.09	25.21	7.12	5.40	-
MMSE-MPC	10.47	18.09	13.54	-4.55	3.69	-
CBF	0.35	0.35	47.75	47.40	1.11	-
	Subarray $2 \times 2$					
Sub MMSE-SPC	38.61	42.15	42.89	0.74	12.83	137.59
Sub MMSE-MPC	37.28	42.15	40.39	-1.76	12.38	235.5
Sub CBF	9.5	9.51	46.45	36.94	3.38	204.50
	Subarray $3 \times 3$					
Sub MMSE-SPC	26.38	39.71	26.95	-12.77	8.80	62.96
Sub MMSE-MPC	25.73	39.71	26.22	-13.49	8.59	132.79
Sub CBF	14.12	14.99	36.30	21.30	4.80	332.43
	Subarray $4 \times 4$					
Sub MMSE-SPC	20.56	37.69	20.84	-16.85	7.08	24.29
Sub MMSE-MPC	20.14	37.69	20.41	-17.28	6.95	88.35
Sub CBF	15.34	18.49	27.42	8.93	5.30	377.48



(a) Subarray  $2 \times 2$



(b) Subarray  $3 \times 3$



(c) Subarray  $4 \times 4$

**Figure 4.4:** CDF of users' spectral efficiency for VSATs considering SLNR and MMSE with different subarray configurations.

SLNR and MMSE BF schemes with SPC and MPC normalization. It can be noted that the proposed BF configuration with subarray  $2 \times 2$  in Fig. 4.4a outperforms the BF design without subarraying for SLNR followed by MMSE. In Fig. 4.4b, with subarray  $3 \times 3$ , we get a gain in the rate for SLNR-SPC in the order of 5 bit/sec/Hz, in the order 7 bit/sec/Hz for SLNR-MPC, in the order of 3.5 for MMSE-SPC, and finally about 5 bit/sec/Hz for MMSE-MPC. Whereas, in Fig. 4.4c, with subarray  $4 \times 4$ , the gain in the spectral efficiency with respect to no subarrays is in the order of 2.5 bit/sec/Hz for SLNR-SPC, and in the order of 5 bit/sec/Hz for SLNR-MPC.

#### 4.4 Conclusions

In this chapter, we proposed LFOV architecture of planar non-overlapped subarrays on-board in standalone LEO satellite scenario. We assessed the performance of digital BF (MMSE, SLNR) and analog BF as the benchmark algorithms dependent on CSI and non-CSI, respectively. Based on the numerical results, both digital and analog beamforming with subarraying proved to have significantly higher performance in terms of spectral efficiency compared to the reference non-subarrayed architecture. Furthermore, SLNR BF scheme showed once again better performance than MMSE BF with all the configurations of subarrays. The evaluation focused on the design of non-overlapped LFOV arrays, i.e., the beamforming has been implemented at subarray level only. We considered various dimensions in the configuration. In the next chapter, we will assess the improved performance introduced by this type of architecture in multiple satellite scenario.

## **Chapter 5 - Cell-Free Federated MIMO Beamforming in Multiple LEO Satellite Scenario**

Mega LEO (or NGSO nodes) constellations are recognized as one of the main enabling technologies for B5G and 6G systems. These constellations are instrumental in providing global coverage, and seamless connectivity [94, 95]. They pave the way for the implementation of advanced interference management techniques, such as distributed or federated massive MIMO technology, which involves non-co-located antenna elements onboard multiple satellites grouped within swarms. In this chapter, we adopt a multiple satellites scenario instead of standalone satellite considered in the previous chapters.

We, first, discuss possible options of multiple NGSO nodes NTN architecture, then we describe the system model of the proposed Cell-Free (CF) federated MIMO incorporated with LFOV subarrays in NTN. Thereafter, the numerical results in terms of system KPIs are provided showing a significant improvement obtained by the proposed scheme in such type of NTN architecture. Finally, a comparative analysis between single satellite node and multiple satellite node scenario is evaluated highlighting the trade-off between interference management limitation and the extended coverage provided by multiple satellite scenario.

The content of this chapter is based on the following accepted and presented paper at the IEEE WCNC 24 conference:

M. R. Dakkak, D. G. Riviello, A. Guidotti and A. Vanelli-Coralli, “Federated Beamforming with Subarrayed Planar Arrays for B5G/6G LEO Non-Terrestrial Networks”, *2024 IEEE Wireless Communications and Networking Conference (WCNC)*, Dubai, United Arab Emirates.

## 5.1 Contribution

The main contribution of this chapter is proposing a LFOV subarrays architecture incorporated with CF federated MIMO to improve system performance, and mitigate the CCI in FFR scenario within NTN systems. To the best of our knowledge, this particular scheme has not been previously presented in the existing literature within this type of NTN architecture. Additionally, the proposed design is deemed a cost-effective strategy, as it does not require an increase in the number of RF chains compared to the reference design. Furthermore, the consideration of the movement of a swarm of multiple satellites introduces an additional element of novelty to the proposed approach.

## 5.2 System architecture options

In this section, we distinguish between two possible architectures of NGSO based NTN to support Cell-free MIMO beamforming, [13]:

- Centralized MIMO architecture, in which MIMO is implemented with co-located radiating elements on-board a single satellite (this option was assumed in the previous analysis of the first four chapters).
- Federated MIMO architecture, where MIMO is implemented with non co-located radiating elements on-board multiple satellites belonging to the same formation, i.e, swarm.

With legacy transparent payloads, scheduling and beamforming are entirely defined on-ground; then, the beamforming coefficients can be applied to the users'

signals either on-board or on-ground, in this case no federated MIMO is possible and each node behaves as a standalone satellite scenario. Whereas for federated MIMO option, regenerative payload is needed as it requires a tight time and frequency synchronisation among the cooperating satellites in the swarm, which can be only achieved by means of Intra-Swarm Links (ISL). When regenerative payload is assumed, the CF federated MIMO architecture can be classified based on the the type of functional split, i.e, determining which layers of NR gNB are implemented on-board in the Distributed Unit (DU), gNB-DU, and which ones are implemented on-ground in the Centralized Unit (CU), gNB-CU, as defined in 3GPP TR 38.801 [96], furthermore, swarms can even be implemented with a full gNB (i.e., with all functions) on each NGSO node. It is worthwhile highlighting that, in the framework of NTN systems, the term *Cell-Free* refers to not requiring the definition of a beam lattice on-ground, thus computing the beamforming coefficients based on the channel between the on-board radiating elements (rather than the equivalent beam antennas) and the users. In this chapter, we consider the architecture option of CF federated MIMO, as depicted in Fig. 5.1.

### 5.3 System Model

We consider a constellation of NGSO nodes providing the service to the on-ground UEs. Notably, for a generic coverage area, only a subset of nodes will be visible from all of the UEs, based on the nodes' field of view and the minimum elevation angle requirements. In this chapter, we assume  $S$  NGSO nodes in a generic single swarm are visible by all the UEs in the considered area. The

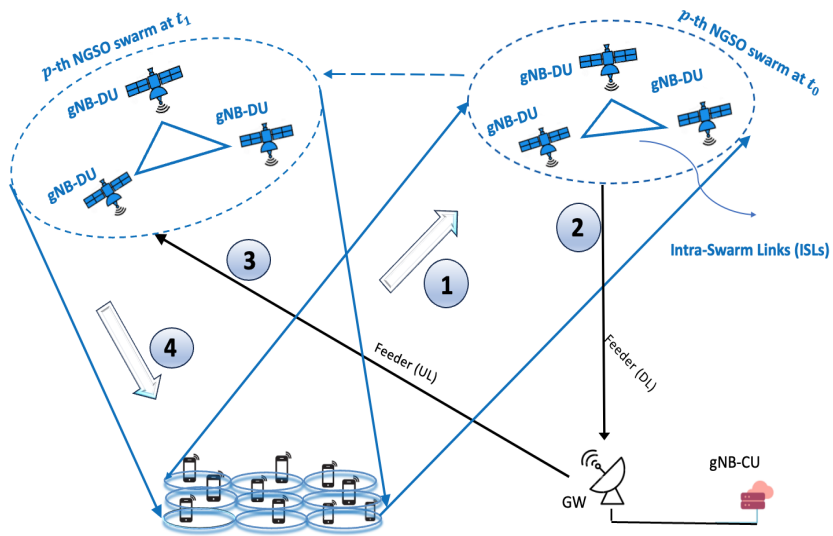


**Figure 5.1:** CF federated MIMO beamforming architecture for  $p$ -th NGSO swarm.

visibility assumption is possible thanks to the handover procedure that can be implemented through Intra-Swarm Links and/or Inter-Swarm links in the constellation [97]. It is worth mentioning that the handover procedure is out of scope of this thesis where the focus will be on the analysis of cell free federated MIMO schemes within swarms of multiple satellites. Additionally, thanks to ISLs, the nodes can synchronize the transmission in the time and frequency domains for realization the distributed BF schemes in feed space scenario. Each node is equipped with an on-board UPA made of  $N_{tot} = MN$  total radiating elements grouped into  $N$  subarrays of  $M$  elements, providing connectivity to  $K$  uniformly distributed on-ground UEs and utilizing the same spectral resources (FFR). We consider Earth-moving beams, i.e., the coverage area of each node is always centered around its Sub Node Point (SNP) and, thus, the beams move on-ground along with the node on its orbit. For the sake of simplicity, we assume that

all the nodes are at the same altitude and are equipped with the same antenna configuration as a typical mega-constellation. To ensure the user connectivity, the NGSO node shall establish a logical connection with a Centralized Unit on-ground gNB-CU (i.e., OGBF computation is assumed here). This connection can be achieved by either i) each node is assumed to be directly linked to a ground-based gateway (GW), or ii) to be connected to another node in the constellation by means of ISLs . Fig. 5.1 depicts the system architecture of the  $p$ -th NGSO swarm which requires  $G$  on-ground GWs. However, for the sake of simplicity, we depict only a single GW. The nodes are supposed to enable distributed BF schemes (introduced in the next section) which require the estimates of either the CSI or the user locations, respectively, to be provided by the UEs. Fig. 5.1 also illustrates the four main steps of on-ground BF in the proposed scenario: i) the CSI or location estimates are obtained by the UEs at time instant  $t_0$  and sent to the network, when the nodes of the  $p$ -th swarm are located at a specific orbital position; ii) the estimates are returned to the gNB-CU to calculate the beamforming coefficients; iii) such coefficients are sent to the nodes of the  $p$ -th swarm to be applied to the users' signals on-board by each gNB-DU; iv) the transmission of the beamformed signals occurs at time instant  $t_1 > t_0$ . During the aging interval,  $\Delta t = t_1 - t_0$ , the NGSO nodes have moved and, thus, there is a misalignment between the actual channel used during the transmission and the estimated channel used to compute the beamforming matrix. Hence, the MIMO performance will be impacted by such misalignment; the smaller the aging delay, the better the MIMO performance.

The aging delay is computed as:

$$\Delta t = t_{user} + t_{feeder}^{(UL)} + t_{feeder}^{(DL)} + t_p + t_{rout} + t_{ad} \quad (5.1)$$

where: i)  $t_{user}$  is the latency on the user return link; ii)  $t_{feeder}^{(DL)}$  is the delay on the feeder downlink; iii)  $t_{feeder}^{(UL)}$  is the delay on the feeder uplink; iv)  $t_p$  is the processing delay required to compute the beamforming coefficients; and v)  $t_{rout}$  is the latency due to routing on the ISLs, if present; finally  $t_{ad}$  includes any additional delay. Moreover, to avoid the feeder link latency, beamforming procedure can be implemented totally on-board in federated MIMO architecture, leading to mitigate the channel aging issue.

We assume the same antenna array model for each node which is based on ITU-R Recommendation M.2101-0. Generally, the antenna boresight direction points to the SNP, while the point  $\mathbf{P}$  represents the position of the user terminal on the ground. The user direction can be identified by the angle pair  $(\vartheta, \varphi)$  where the boresight direction is  $(0,0)$ . We can now derive the direction cosines for the considered user as:  $u = \frac{P_y}{\|\mathbf{P}\|} \sin \vartheta \sin \varphi$ , and  $v = \frac{P_z}{\|\mathbf{P}\|} \cos \vartheta$ . The total array response of the UPA of the  $s$ -th node in the generic direction  $(\vartheta_{i,s}, \varphi_{i,s})$  can be expressed as the Kronecker product between the array responses of the 2 ULAs of the  $s$ -th node lying on the  $y$ -axis and  $z$ -axis. We first define the  $1 \times N_H$  Steering Vector (SV) of the ULA along the  $y$ -axis,  $\mathbf{a}_H(\theta_{i,s}, \varphi_{i,s})$ , and the  $1 \times N_V$  SV of the ULA along the  $z$ -axis,  $\mathbf{a}_V(\theta_{i,s})$  [93]:

$$\mathbf{a}_H(\vartheta_{i,s}, \varphi_{i,s}) = \left[ 1, e^{jk_0 M_H d_H \sin \vartheta_{i,s} \cos \varphi_{i,s}}, \dots, e^{jk_0 M_H d_H (N_H - 1) \sin \vartheta_{i,s} \cos \varphi_{i,s}} \right] \quad (5.2)$$

$$\mathbf{a}_V(\vartheta_{i,s}, \varphi_{i,s}) = \left[ 1, e^{jk_0 M_V d_V \sin \vartheta_{i,s} \sin \varphi_{i,s}}, \dots, e^{jk_0 M_V d_V (N_V - 1) \sin \vartheta_{i,s} \sin \varphi_{i,s}} \right] \quad (5.3)$$

where:  $k_0 = 2\pi/\lambda$  is the wave number,  $N_H, N_V$  denote the number of subarrays on the horizontal and vertical directions, respectively, with  $N = N_H N_V$ , and  $M_H, M_V$  denote the number of antenna elements per each subarray on the horizontal ( $y$ -axis) and vertical ( $z$ -axis) directions, respectively, with  $M = M_H M_V$ , and finally  $d_H, d_V$  denote the distance between adjacent antenna elements on the horizontal and vertical directions, respectively, as depicted in the structure of subarrayed UPA for a single NTN node in Fig. 4.2. It is worth mentioning that the total number of antenna elements for each  $s$ -th node are  $N_{tot} = MN$ , where  $M = 1$ , if subarraying is not implemented. We can define the total steering vector of the full UPA (an array equipped with subarrays as antenna elements) of the  $s$ -th node as the Kronecker product of the 2 SV's along each axis:

$$\mathbf{a}_{UPA}(\vartheta_{i,s}, \varphi_{i,s}) = \mathbf{a}_H(\vartheta_{i,s}, \varphi_{i,s}) \otimes \mathbf{a}_V(\vartheta_{i,s}) \quad (5.4)$$

We further assume that the node is equipped with directive antenna elements, whose radiation pattern is denoted by  $g_E(\vartheta_{i,s}, \varphi_{i,s})$  according to Table 3 in [54], and these elements are grouped into  $N$  subarrays of size  $M_H \times M_V$ . We can define the subarray factor  $F_{sub}(\vartheta_{i,s}, \varphi_{i,s})$  as:

$$F_{sub}(\vartheta_{i,s}, \varphi_{i,s}) = \frac{\sin\left(\frac{M_V}{2}k_0d_V \cos \vartheta_{i,s}\right)}{\sqrt{M_V} \sin\left(\frac{1}{2}k_0d_V \cos \vartheta_{i,s}\right)} \frac{\sin\left(\frac{M_H}{2}k_0d_H \sin \vartheta_{i,s} \sin \varphi_{i,s}\right)}{\sqrt{M_H} \sin\left(\frac{1}{2}k_0d_H \sin \vartheta_{i,s} \sin \varphi_{i,s}\right)} \quad (5.5)$$

Finally, we can express the total SV of the UPA of subarrays made of directive antenna elements at the  $s$ -th node targeted towards the  $i$ -th user as the product of  $\mathbf{a}_{UPA}(\vartheta_{i,s}, \varphi_{i,s})$ , the element radiation pattern  $g_E(\vartheta_{i,s}, \varphi_{i,s})$  and the subarray factor  $F_{sub}(\vartheta_{i,s}, \varphi_{i,s})$ :

$$\mathbf{a}(\vartheta_{i,s}, \varphi_{i,s}) = g_E(\vartheta_{i,s}, \varphi_{i,s}) F_{sub}(\vartheta_{i,s}, \varphi_{i,s}) \mathbf{a}_{UPA}(\vartheta_{i,s}, \varphi_{i,s}) \quad (5.6)$$

The CSI vector  $\mathbf{h}_{i,s}$ , which represents the channel between the  $i$ -th on-ground UE and the UPA on-board of the  $s$ -th node, can be written as:

$$\mathbf{h}_{i,s} = G_{i,s}^{(rx)} \frac{\lambda}{4\pi d_{i,s}} \sqrt{\frac{L_{i,s}}{\kappa B T_i}} e^{-j \frac{2\pi}{\lambda} d_{i,s}} e^{-j \psi_{i,s}} \mathbf{a}(\vartheta_{i,s}, \varphi_{i,s}) \quad (5.7)$$

where: i)  $d_{i,s}$  is the slant range between the  $i$ -th user and  $s$ -th node; ii)  $\kappa B T_i$  denotes the equivalent thermal noise power, with  $\kappa$  being the Boltzmann's constant,  $B$  is the user bandwidth which is assumed to be the same for all users, and  $T_i$  is the equivalent noise temperature of the  $i$ -th user receiving equipment; iii)  $L_{i,s}$  denotes the additional losses between the  $s$ -th node and  $i$ -th user (*e.g.*, atmospheric and antenna cable losses), and iv)  $G_{i,s}^{(rx)}$  denotes the receiving antenna gain for the  $i$ -th user with respect to the  $s$ -th node and v)  $\psi_{i,s}$  is the possible misalignment between different nodes due to non-ideal swarm synchronization, modelled as a Gaussian random variable (RV). The additional losses are computed as:

$$L_{i,s} = L_{i,s}^{sha} + L_{i,s}^{atm} + L_{i,s}^{sci} + L_{i,s}^{CL} \quad (5.8)$$

where  $L_{i,s}^{sha}$  represents the log-normal shadow fading term,  $L_{i,s}^{atm}$  the atmospheric loss, and  $L_{i,s}^{sci}$  the scintillation, and  $L_{i,s}^{CL}$  is the Clutter Loss, to be included for the UEs in NLOS condition. These terms are computed based on 3GPP TR 38.811, in which it is also defined LOS probability that is a function of the propagation environment and the elevation angle for each UE. For the generic  $i$ -th user, its overall channel signature can be obtained by collecting the CSI vectors from all of the NGSO nodes into the  $NS$ -dimensional  $\mathbf{h}_i^{(t_0)} = [\mathbf{h}_{i,1}^{(t_0)} | \dots | \mathbf{h}_{i,S}^{(t_0)}]$ . The overall  $K \times (NS)$  channel matrix at the estimation time  $t_0$  is given by  $\hat{\mathbf{H}}_{Sys} = [(\mathbf{h}_1^{(t_0)})^\top | \dots | (\mathbf{h}_S^{(t_0)})^\top]^\top$ . For each time slot, the RRM algorithm selects a subgroup of  $K_{sch}$  users to be scheduled, resulting in a  $K_{sch} \times (NS)$  complex scheduled channel matrix,  $\hat{\mathbf{H}} = \mathcal{F}(\hat{\mathbf{H}}_{Sys})$  where  $\mathcal{F}(\cdot)$  stands for the RRM function. Hence,  $\hat{\mathbf{H}} \subseteq \hat{\mathbf{H}}_{Sys}$  is defined as a sub-matrix of  $\hat{\mathbf{H}}_{Sys}$ , which only includes the rows associated with the scheduled users. The proposed BF scheme calculates the  $(NS) \times K_{sch}$  complex beamforming matrix  $\mathbf{W}$  which projects the  $K_{sch}$  dimensional column vector,  $\mathbf{s} = [s_1, \dots, s_{K_{sch}}]^\top$  which contains the unit-variance user symbols, onto the  $(NS)$ -dimensional space determined by all of the swarm antenna feeds. The  $K_{sch}$ -dimensional vector of received symbols is:

$$\mathbf{y} = \mathbf{H}_{t_1} \mathbf{W}_{t_0} \mathbf{s} + \mathbf{z} \quad (5.9)$$

It shall be noted that, as previously discussed, the estimated channel matrix  $\hat{\mathbf{H}}_{t_0}$ , obtained at time instant  $t_0$ , is used to compute the beamforming matrix  $\mathbf{W}_{t_0}$ , whereas, at time instant  $t_1$ , the channel matrix to be used is different and characterized by  $\mathbf{H}_{t_1}$ . It is worth mentioning that the equations and definitions

of the system KPIs considered in this chapter, i.e., SINR and spectral efficiency, are already discussed in this section 2.6 in Chapter 2, and they are assumed the same here.

#### 5.4 Distributed beamforming schemes

The following CSI/location based algorithms are already discussed as the benchmark for the assessment of the performance in Chapter 3. However, in this section we update and clarify the formula definition in terms of NGSO node per each swarm instead of standalone node.

- **Conventional Beamforming (CBF):** or as also called beam steering. In this approach, for each  $s$ -th node the weights are generated in order to produce a phase shift to compensate the delay of the direction  $(\theta_{i,s}, \varphi_{i,s})$  of the  $i$ -th user of interest. The overall beamforming vector designed for the  $i$ -th user can be obtained by vertically concatenating the conventional beamformer at each  $s$ -node:

$$\mathbf{W}_{:,i} = \frac{1}{\sqrt{NS}} [\mathbf{a}_{UPA}(\vartheta_{i,1}, \varphi_{i,1}), \dots, \mathbf{a}_{UPA}(\vartheta_{i,S}, \varphi_{i,S})]^H \quad (5.10)$$

- **Minimum Mean Square Error (MMSE):** as already defined, it is given by:

$$\mathbf{W}_{MMSE} = \hat{\mathbf{H}}^H (\hat{\mathbf{H}}\hat{\mathbf{H}}^H + \alpha \mathbf{I}_{K_{sch}})^{-1} \quad (5.11)$$

where  $\hat{\mathbf{H}}$  is the estimated channel matrix at  $t_0$ . In the above equation,  $\alpha$  is a the regularisation factor, since the channel coefficients are normalised

to the noise power, its optimal value is given by  $\alpha = \frac{N}{P_{t,s}}$  [61], where  $P_{t,s}$  is the available power per node in the swarm. The above formulation is computationally efficient since, notably,  $K_{sch} < N S$ .

Lastly, as explained in [76], the power normalization is a crucial aspect in beamforming as it ensures accurate consideration of the potential power output from both the NGSO node and each individual antenna. We assume that each node has the same available on-board power  $P_{t,s}$ . We can observe that the overall  $(N S) \times K_{sch}$  beamforming matrix can be divided in blocks corresponding to the single node beamforming matrices, *i.e.*,  $\mathbf{W} = [\mathbf{W}_1 \mathbf{W}_2 \cdots \mathbf{W}_S]^T$  with  $\mathbf{W}_s$  denoting the  $N \times K_{sch}$  beamforming matrix of the  $s$ -th NGSO node. Therefore, we introduce the following swarm-based normalizations:

1. Swarm-based Sum Power Constraint (sSPC): an upper bound is imposed on the total per-node power  $P_{t,s}$ , therefore each node beamforming matrix  $\mathbf{W}_s$  can be normalized as:

$$\tilde{\mathbf{W}}_s = \frac{\sqrt{P_{t,s}} \mathbf{W}_s}{\sqrt{\text{tr}(\mathbf{W}_s \mathbf{W}_s^H)}} \quad (5.12)$$

This approach guarantees that the overall emitted power satisfies i)  $\|\mathbf{W}\|_F^2 = S P_{t,s}$ ; ii) each satellite emits a power  $\|\mathbf{W}_s\|_F^2 = P_{t,s}$  for  $s = 1, \dots, S$ . Clearly, this approach leads to a slight degradation in the performance, because when the normalisation is not scalar for the entire beamforming matrix  $\mathbf{W}$  leads to a loss of orthogonality in the beamforming matrix columns.

2. Swarm-based Maximum Power Constraint (sMPC):

$$\tilde{\mathbf{W}}_s = \frac{\sqrt{P_{t,s}} \mathbf{W}_s}{\sqrt{N \max_j [\mathbf{W}_s \mathbf{W}_s^H]_{j,j}}} \quad (5.13)$$

This approach ensures that the overall emitted power is still satisfying both aforementioned conditions i and ii but actually leads to lower emitted power levels, since only a single subarray per node in the swarm will transmit the maximum power.

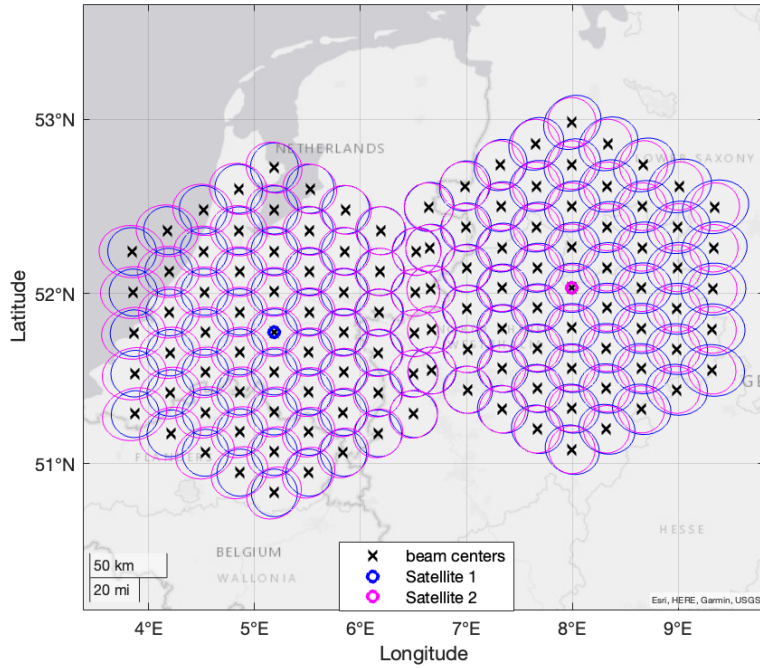


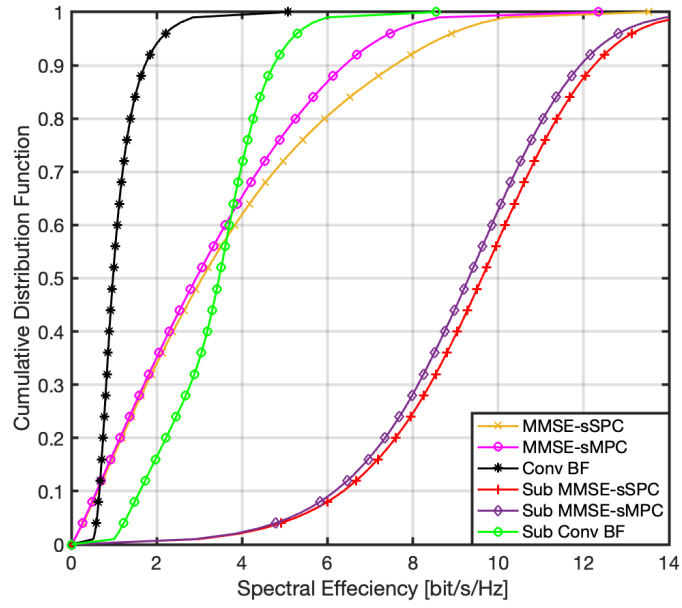
**Figure 5.2:** Federated scenario ( $S = 2$ ). Blue lines represent the beam lattice generated by node 1 and magenta by node 2.

**Table 5.1:** System Configuration Parameters (CF Federated MIMO)

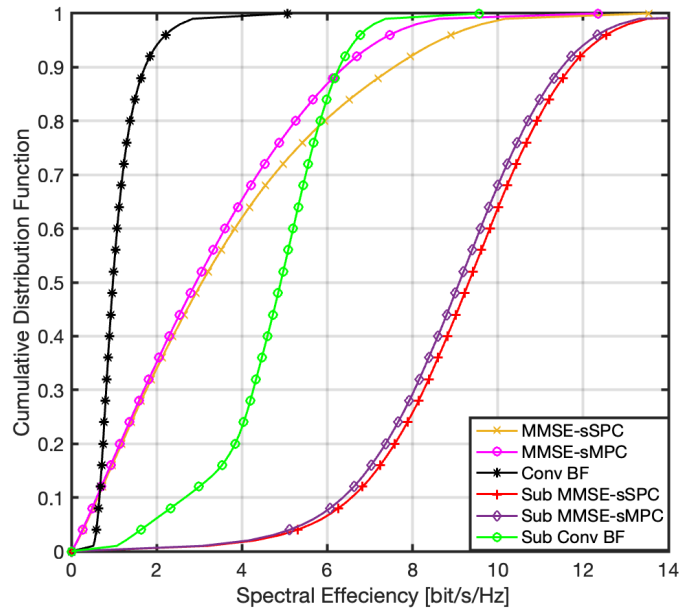
Parameter	Value
Carrier frequency	S-band (2 GHz)
User bandwidth	30 MHz
Beamforming space	feed
Receiver type	fixed VSATs
Channel model	LOS, NLOS
Propagation scenario	urban
Total on-board power density $P_{t,dens}$ without subarraying	0 dBW/MHz
Total on-board power density with subarraying	$P_{t,dens} - 10 \log_{10}(M_H M_V)$
Number of tiers	4
Number of scheduled users $K_{sch}$	118
Number of subarrays $N$	1024 ( $32 \times 32$ )
Number of elements per each subarray $M$	$(2 \times 2)$ , $(3 \times 3)$ , $(4 \times 4)$
Number of antenna elements without subarraying $N_{tot} = N$	1024
Number of antenna elements with subarraying $N_{tot} = MN$	4096, 9216, 16384
User density	0.5 user/km <sup>2</sup>
Number of nodes $S$ in the swarm	2
Angular scanning range	$\Delta\vartheta \simeq 37^\circ$ , $\Delta\varphi \simeq 24.5^\circ$

## 5.5 Numerical results

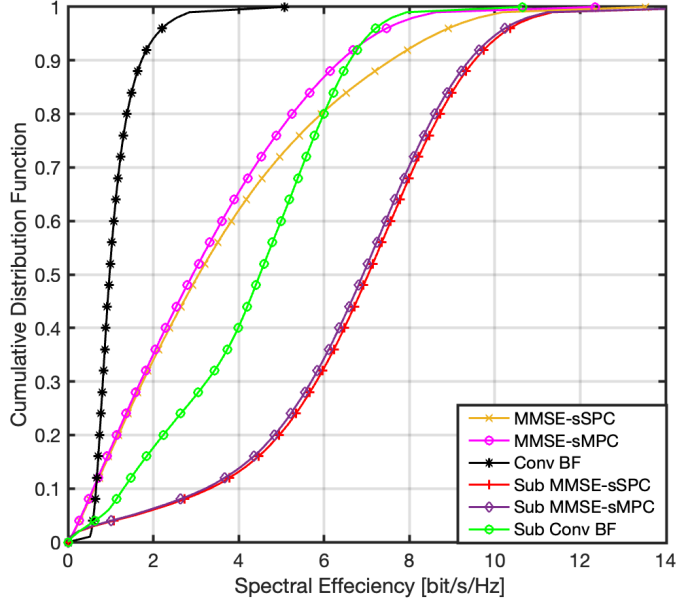
In this section, we report the outcomes of the numerical assessment based on the parameters reported in Table 5.1, considering a federated MIMO architecture with  $S = 2$  nodes at the same altitude  $h_{sat} = 600$  km. Each node in the swarm generates its corresponding lattice, as shown in Fig. 5.2, however this leads to some overlapping beams at the border between the two lattices, *i.e.*, there are beams that have their centers inside other beams boundaries at less than -3 dB. If two users at scheduling phase are selected from such beams, they might have very similar CSI coefficients, and therefore the matrix inversion in MMSE might be ill-conditioned. Hence, to circumvent this issue, we assume a proper RRM scheduling for the users by activating only one beam among those in which the relative distance between beam centers does not guarantee a 3 dB separation. Please notice that the beam lattices are generated only for scheduling purposes, since the aforementioned CF distributed MIMO algorithms are implemented in the feed space scenario. We assume fixed positions of UEs, and they are uniformly distributed with a density of 0.5 users/Km<sup>2</sup>. Specifically, each user is randomly selected for each beam at each time slot, and the total number of time slots is determined to ensure that each user is served at least once. Based on the coverage area shown in Fig. 5.2, it is possible to compute the angular steering range for the array as  $\Delta\vartheta \simeq 37^\circ$ ,  $\Delta\varphi \simeq 24.5^\circ$  in both horizontal and vertical angular directions, respectively, which justifies the use of a LFoV array. The numerical assessment is provided for subarrayed beamforming MMSE and CBF schemes and



(a) Subarray  $2 \times 2$



(b) Subarray  $3 \times 3$



(c) Subarray  $4 \times 4$

**Figure 5.3:** CDF of users' spectral efficiency considering federated MIMO BF schemes with different subarray configurations.

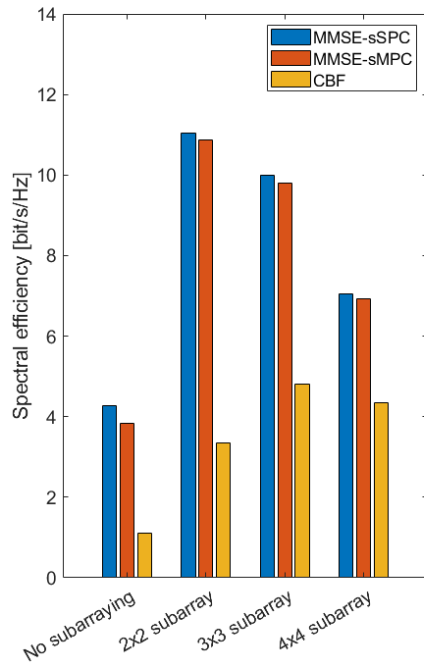
then the performance is compared to the reference beamforming design without subarraying. In order to have a fair comparison, the transmitted power from each node, in case of subarrayed BF, has been divided by  $(M_H M_V)$ , *i.e.*, the maximum achievable subarray gain. Hence, the EIRP values for both subarrayed and non-subarrayed cases shall be equivalent. Since the LFoV array has no steering capability at antenna element level, no hybrid beamforming is taken into account. We assume a propagation scenario with both LOS and NLOS UEs (according to their LOS probability) in urban environment.

Fig. 5.3 shows the CDFs of users' spectral efficiency for all the analyzed beamforming schemes with the sSPC and sMPC normalization considering differ-

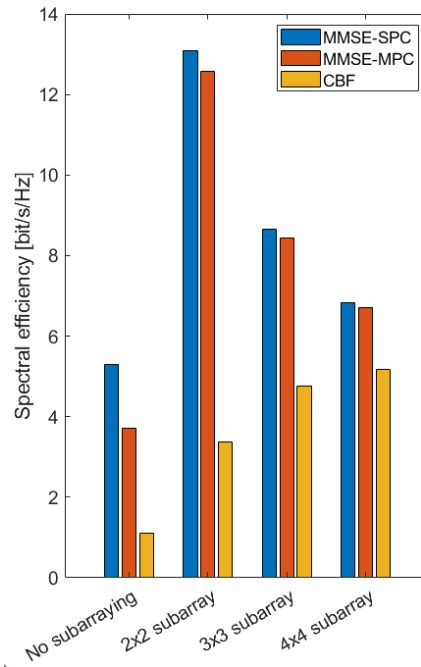
ent subarrays dimensions  $2 \times 2$ ,  $3 \times 3$  and  $4 \times 4$ . In terms of normalization, sSPC shows a slightly better performance than sMPC in all subarray configurations. It is possible to observe that both MMSE-sSPC and MMSE-sMPC show the best performance with  $2 \times 2$  subarray configuration with a gain in terms of rate in the order of 7 bit/s/Hz with respect to the non subarrayed MMSE, whereas CBF provides its best behaviour in terms of rate (about 3.5 bit/s/Hz) with  $4 \times 4$  subarrays and it is even able to outperform MMSE with no subarrays. The superiority of the proposed subarrayed beamforming over non-subarrayed scheme, for both MMSE and CBF, is motivated by the characteristics of LFoV architecture with subarrays that enable more directive (narrower) beams towards the UEs, and, thus enhance the capability of CCI suppression.

Tab. 5.2 details the average values of the KPIs including SINR, SIR, SNR, INR, the rate (spectral efficiency), and the relative gain (percentage) with LFoV subarrays compared to the benchmark of the considered BF schemes in  $S = 2$  scenario, taking into account different dimensions of subarrays.

Finally, we provide in Figs. 5.4a and 5.4b a comparison in the performance between the single satellite ( $S = 1$ ) scenario and multi-satellite ( $S = 2$ ) in LOS sub-urban scenario. In Tab. 5.3, we outline only the system parameters considered in the single satellite scenario which are different from those assumed in dual satellite scenario (Tab. 5.1). It is worth mentioning that in order to provide a fair comparison between the two scenarios, the transmitted power in the single satellite scenario  $P'_t$  is scaled to guarantee that the same average per-user power is available, *i.e.*,  $P'_t = P_{t,s} \frac{2K'_{sch}}{K_{sch}}$ . As illustrated in Fig. 5.4, it can be noticed that



(a)  $S = 2$ .



(b)  $S = 1$ .

**Figure 5.4:** Average spectral efficiency with multi-node ( $S = 2$ ) and single node ( $S = 1$ ) scenario.

**Table 5.2:** Performance of BF with subarraying  $M_H \times M_V$ , dual satellite ( $S = 2$ ).

BF Scheme	KPIs					
	SINR	SIR	SNR	INR	Rate	
	[dB]	[dB]	[dB]	[dB]	[bits/sec/Hz]	Relative gain [%]
	Without Subarrays					
MMSE-SPC	11.97	12.25	31.32	19.07	4.27	-
MMSE-MPC	10.60	12.02	21.15	9.13	3.84	-
CBF	0.32	0.32	42.59	42.26	1.11	-
	Subarray $2 \times 2$					
Sub MMSE-sSPC	33.24	36.75	38.43	1.69	11.05	158.78
Sub MMSE-sMPC	32.73	36.77	37.29	0.53	10.88	183.33
Sub CBF	9.42	9.46	40.74	31.28	3.36	202.70
	Subarray $3 \times 3$					
Sub MMSE-sSPC	30.11	40.61	31.28	-9.33	10.01	134.43
Sub MMSE-sMPC	29.51	40.60	30.56	-10.04	9.81	155.47
Sub CBF	14.16	14.51	34.79	20.28	4.80	332.43
	Subarray $4 \times 4$					
Sub MMSE-sSPC	20.91	33.65	31.74	-11.91	7.05	65.11
Sub MMSE-sMPC	20.52	33.65	21.30	-12.36	6.93	80.47
Sub CBF	12.34	15.06	24.35	9.28	4.34	290.99

**Table 5.3:** Simulation parameters ( $S = 1$  scenario).

Parameter	Value
Number of tiers	5
Number of scheduled users $K'_{sch}$	91
Total power density $P'_{t,s,dens}$ without subarraying	$P_{t,s,dens} + 10 \log_{10} \left( \frac{2K'_{sch}}{K_{sch}} \right)$
Total power density with subarraying	$P'_{t,s,dens} - 10 \log_{10}(M_H M_V)$
Angular scanning range	$\Delta\vartheta' = \Delta\varphi' \simeq 28^\circ$

there is a degradation in the performance compared to the single node scenario due to the geometry of the multi-node system and also due to the slight loss in orthogonality with sSPC and sMPC normalisation, hence the dual satellite scenario is more critical in terms of interference limitation. However, obviously the dual node scenario provides better coverage than the single satellite one.

## 5.6 Conclusions and future works

In this chapter, we proposed a NTN architecture composed of multiple swarms of NGSO nodes. We assessed the performance of CF-MIMO federated CSI/location-based beamforming algorithms with LFOV architecture made up of smaller planar subarrays. The numerical results provided a significant improvement in the performance in terms of spectral efficiency of the subarrayed beam-

forming configuration with respect to the non-subarrayed scenario, with both configurations having the same number of RF chains. Future works, which will be discussed in the next chapter, shall consider more than two nodes within the swarm, and shall assess multi-layered nodes, *i.e.*, not only the nodes at the same altitude. Furthermore, the implementation of Deep Learning algorithms will be a pivotal aspect, aiming to predict CSI for BF algorithms to mitigate the channel aging issue.

## Chapter 6 - Conclusion and Future Possible Technologies for MU-MIMO Beamforming in 5G/6G NTN

### 6.1 Thesis conclusion

In Chapter 1, we provided an overview of NTN in 5G and beyond by discussing the classification of NTN platforms and their topology types, the segments of SatCom architecture, the definition and roadmap of NTN in 3GPP standardization, and the main impairments that challenge the NTN systems, i.e., delay, Doppler effect, and path loss. Furthermore, we introduced the full frequency reuse scheme in NTN, emphasizing its trade-off in enhancing spectrum efficiency while introducing high CCI, and then we highlighted the possible techniques to address this issue, specifically MU-MIMO algorithms.

In Chapter 2, we described the system model of a standalone LEO satellite by discussing its architecture, antenna array model, and channel model. Then we defined the KPIs that will be utilized in the evaluation of the NTN system's performance.

In Chapter 3, we introduced the benchmark MU-MIMO beamforming algorithms based on i) either the knowledge of CSI estimates, i.e., MMSE and ZF, or ii) users' locations estimates i.e., MB and CBF. Then, we designed and proposed the SLNR BF scheme for a unicast approach within a standalone LEO satellite

scenario, stating that the SLNR BF can overcome the issue of joint optimization between beamforming vectors by splitting it into multiple separate optimization problems for the targeted users and provide a closed form solution. The simulation results of the proposed scheme showed higher performance compared to the benchmark techniques in terms of the system KPIs, i.e., per-user spectral efficiency, in both LOS and NLOS propagation scenarios. Furthermore, we considered the satellite's movement with both fixed and travelling UEs equipped with VSATs. Regarding the power normalization, the SPC approach proved the best performance for all the evaluated BF schemes, followed by the MPC approach, while the PAC one provided the worst performance, additionally a slight improvement for the SLNR BF with respect to the MMSE BF was observed by increasing the same amount of the transmitted power density. Finally, the complexity analysis of SLNR and MMSE BF demonstrated that the proposed SLNR BF scheme is computationally more expensive than MMSE BF, thus we have a trade off between performance and complexity in terms of the proposed scheme.

In Chapter 4, we proposed LFOV architecture of non-overlapped planar subarrays within a standalone LEO satellite scenario. We assessed the performance of digital BF (MMSE, SLNR) and analog BF (CBF) as the benchmark algorithms dependent on CSI and users' locations, respectively. Based on the numerical results, both digital and analog beamforming with subarraying proved to have significantly higher performance in terms of spectral efficiency compared to the reference non-subarrayed architecture. Furthermore, SLNR BF scheme showed once again better performance than MMSE BF with all the configura-

tions of subarrays. It is important to remark that the number of RF chains for both scenario, i.e, the reference and proposed one, is the same. Hence, no further costs are added related to RF chains.

In Chapter 5, we discussed possible options of multiple NGSO nodes NTN architecture. Then we proposed CF federated MIMO beamforming incorporated with LFOV subarrays. The numerical results of the system level performance showed a significant improvement obtained by the proposed scheme in such type of NTN architecture compared to the benchmark design. Finally, a comparative analysis between single satellite node and multiple satellite node scenario demonstrated a trade-off between interference management limitation and the extended coverage provided by multiple satellite scenario.

## 6.2 Future work and possible enabling technologies

In this section, we discuss the possible extended developments to improve MU-MIMO beamforming in B5G/6G NTN, through the following aspects:

- **Extending CF federated MIMO scenario**, we can enhance and broaden the scenario introduced in Chapter 5 by: i) including more than two nodes in each swarm, ii) analyzing NTN nodes at various altitudes. These NTN nodes might be of the same type, such as two LEO nodes at different altitudes, or they may differ in types, e.g., a connection between LEO and HAPS nodes. This leads to configuring a 3D multi-layered hierarchical NTN architecture [98, 99], capable of offering extended and seamless coverage,

minimizing latency, and providing robust backup and resilience capabilities.

- **Hybrid beamforming**, in the LFOV architecture made of subarrays, presented in both single and multiple satellite scenarios, we explored the options of both fully digital and fully analog beamforming. This methodology can be expanded to include hybrid beamforming, representing a cost-effective alternative. With hybrid beamforming, there is the potential to substantially decrease hardware costs and power consumption by utilizing a limited number of RF chains, while still achieving performance levels comparable to those of a fully digital beamforming scheme [100].
- **AI/ML based beamforming**, obtaining effective instantaneous CSI becomes challenging due to the mobility of the satellite and this results in having a time-varying propagation environment. As previously seen in the system model analysis for both standalone and multiple satellite scenarios, such channel aging issue impacts the performance of MU-MIMO beamforming, since any minimal angular deviation may cause a beam alignment failure when the LEO or the NTN node transmits the beamformed symbols according to the obtained outdated CSI. Hence, a Deep Learning (DL)-based CSI prediction scheme can be proposed to address the channel aging issue by exploiting the temporal correlation of the channel. As shown in Fig. 6.1, a block diagram of a channel predictor is proposed to improve the CSI-based BF design in NTN. Basically, the channel predictor is composed by Conventional Neural Network (NN), then Long Short Term Memory (LSTM)

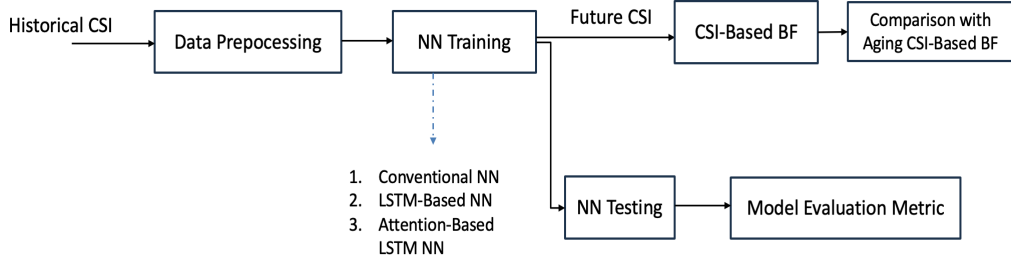


**Figure 6.1:** Block diagram of the proposed NN-based CSI prediction.

NN will be considered. The predictor is first trained by offline learning and then it feeds back the corresponding output results online based on the input data to realize channel feature extraction and future CSI prediction in LEO NTN scenario. Furthermore, advanced LSTM channel prediction scheme will be evaluated based on the attention, i.e., enabling higher weights to the more recent channels coefficients, to improve the future channel prediction [101].

- **RIS-based beamforming**, Reconfigurable Intelligent Surfaces (RIS) have recently received extremely high interest in NTN literature, as they can play a pivotal role in enhancing MIMO BF performance in NTN through two main aspects:

1. RIS technology can be integrated into the ground infrastructure of satellite networks to enable adaptive beamforming. This involves dynamically adjusting the reflective elements to optimize signal directionality based on changing communication requirements or environmental conditions.

2. RIS contributes to minimize interference in NTN by shaping and precisely steering beams. This capability is particularly valuable in environments with multiple satellites.

In 6.2, it is shown an example of RIS-assisted beamforming scheme in a LEO NTN system.

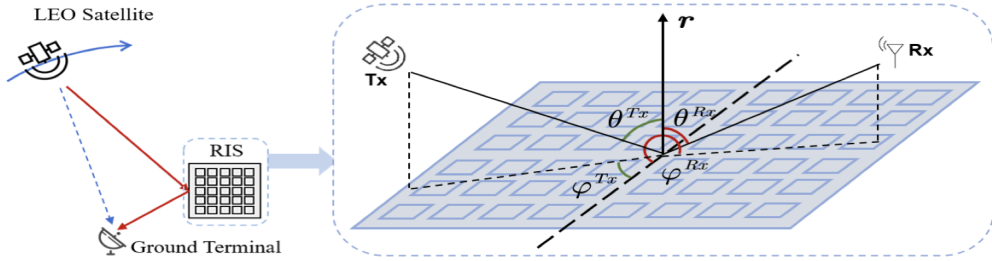


**Figure 6.2:** RIS-assisted beamforming scheme in LEO SatCom.  
[102]

Finally, it shall be noticed that, in terms of feasibility of the solutions and technologies discussed in this thesis, an important aspect is related to beam management in 3GPP NR via NTN. In fact, aspects related to, e.g., signalling or the number of allowed simultaneous beams are defined based on the mapping among NR cells, NR beams, and NTN beams. These aspects are not considered in this thesis and will be considered as an extension for future works.

## References

- [1] Oltjon Kodheli, Eva Lagunas, Nicola Maturo, Shree Krishna Sharma, Bhavani Shankar, Jesus Fabian Mendoza Montoya, Juan Carlos Merlano Duncan, Danilo Spano, Symeon Chatzinotas, Steven Kisseleff, Jorge Querol, Lei Lei, Thang X. Vu, and George Goussetis. "Satellite Communications in the New Space Era: A survey and future challenges". *IEEE Communications Surveys and Tutorials*, 23(1):70–109, 2021.
- [2] Federica Rinaldi, Helka-Liina Maattanen, Johan Torsner, Sara Pizzi, Sergey Andreev, Antonio Iera, Yevgeni Koucheryavy, and Giuseppe Araniti. "Non-Terrestrial Networks in 5G and Beyond: A survey". *IEEE Access*, 8:165178–165200, 2020.
- [3] Claudia Carballo González, Sara Pizzi, Maurizio Murrone, and Giuseppe Araniti. "Multicasting Over 6G Non-Terrestrial Networks: A Softwarization-Based Approach". *IEEE Vehicular Technology Magazine*, 18(1):91–99, 2023.
- [4] A. Vanelli-Coralli, N. Chuberre, M. Gino, A. Guidotti, and M. Eljaafari. "5G Non-Terrestrial Networks: Technologies, Standards, and System Design". Wiley, 2024.
- [5] Andri Qiantori, Agung Sutiono, Hadi Hariyanto, Hirohiko Suwa, and Toshizumi Ohta. "An Emergency Medical Communications System by Low Altitude Platform at the Early Stages of a Natural Disaster in Indonesia". *Journal of medical systems*, 36:41–52, 02 2012.
- [6] Bin Li, Zesong Fei, and Yan Zhang. "UAV Communications for 5G and Beyond: Recent Advances and Future Trends". *IEEE Internet of Things Journal*, 6(2):2241–2263, 2019.
- [7] Mario Marchese, Aya Moheddine, and Fabio Patrone. "IoT and UAV Integration in 5G Hybrid Terrestrial-Satellite Networks". *Sensors*, 19(17), 2019.
- [8] Laurent Reynaud and Tinku Rasheed. "Deployable Aerial Communication Networks: Challenges for Futuristic Applications". In "*Proceedings of the*

*9th ACM symposium on Performance evaluation of wireless ad hoc, sensor, and ubiquitous networks*", pages 1–4, 2012.

- [9] AMS Dottorato (Institutional Doctoral Theses Repository by AlmaDI University of Bologna). <http://amsdottorato.unibo.it/9879>.
- [10] G. Maral, M. Bousquet, and Z. Sun. *"Satellite Communications Systems: Systems, Techniques and Technology"*. Wiley, 2020.
- [11] Zanyang Dong, Longteng Yi, Pengfei Qin, Yejun Zhou, Cheng Zhang, and Kang Liu. "Quantification and Analysis of Carrier-to-Interference Ratio in High-Throughput Satellite Systems". *Electronics*, 12(16), 2023.
- [12] Toon Norp, Jean-Yves Fine, and Relja Djapic. "Network Aspects of Integrating 5G and Satellite Communication". *International Journal of Satellite Communications and Networking*, 41(3):239–248, 2023.
- [13] Alessandro Guidotti, Alessandro Vanelli-Coralli, and Carla Amatetti. "Federated Cell-Free MIMO in Non-Terrestrial Networks: Architectures and Performance". Jan 2023.
- [14] Oltjon Kodheli, Eva Lagunas, Nicola Maturo, Shree Krishna Sharma, Bhavani Shankar, Jesus Fabian Mendoza Montoya, Juan Carlos Merlano Duncan, Danilo Spano, Symeon Chatzinotas, Steven Kisseleff, Jorge Querol, Lei Lei, Thang X. Vu, and George Goussetis. "Satellite Communications in the New Space Era: A Survey and Future Challenges". *IEEE Communications Surveys and Tutorials*, 23(1):70–109, 2021.
- [15] Israel Leyva-Mayorga, Beatriz Soret, Maik Röper, Dirk Wübben, Bho Matthiesen, Armin Dekorsy, and Petar Popovski. "LEO Small-Satellite Constellations for 5G and Beyond-5G Communications". *IEEE Access*, 8:184955–184964, 2020.
- [16] Xiaohua Jia, Tao Lv, Feng He, and Hejiao Huang. "Collaborative Data Downloading by Using Inter-Satellite Links in LEO Satellite Networks". *IEEE Transactions on Wireless Communications*, 16(3):1523–1532, 2017.
- [17] Aizaz U. Chaudhry and Halim Yanikomeroglu. "Free Space Optics for Next-Generation Satellite Networks". *IEEE Consumer Electronics Magazine*, 10(6):21–31, 2021.

- [18] Mohammed Y. Abdelsadek, Aizaz U. Chaudhry, Tasneem Darwish, Eylem Erdogan, Gunes Karabulut-Kurt, Pablo G. Madoery, Olfa Ben Yahia, and Halim Yanikomeroglu. "Future Space Networks: Toward the Next Giant Leap for Humankind". *IEEE Transactions on Communications*, 71(2):949–1007, 2023.
- [19] 3GPP.Global Standardization (Official Website). <https://www.3gpp.org/about-us>.
- [20] 3GPP. "Technical Specification Group Radio access Network; Study on New Radio (NR) to Support Non Terrestrial Networks"; (Release 15). Technical Report TR 38.811 V15.2.0, 3GPP, September 2019.
- [21] 3GPP. "Technical Specification Group Radio Access Network; Solutions for NR to Support NON-Terrestrial Networks", (Release 16). Technical Report Rep. 38.821 version 0.9.0, 3GPP, September 2019.
- [22] 3GPP. "Solutions for NR to Support Non-Terrestrial Networks (NTN)" (release 16). Technical Report TR 38.821, 3GPP, May 2018.
- [23] 3GPP. 5G in Release 17—strong Radio Evolution Accessed. Technical Report Rep. 38.821 version 0.9.0, 3GPP, January 2020.
- [24] 3GPP. Technical Specification Group Services and System Aspects; Study on Using Satellite Access in 5G; (Release 16). Technical Report Rep. 38.822 version 16.0.0, 3GPP, Sophia Antipolis, France, June 2018.
- [25] Xinran Fang, Wei Feng, Te Wei, Yunfei Chen, Ning Ge, and Cheng-Xiang Wang. "5G Embraces Satellites for 6G Ubiquitous IoT: Basic Models for Integrated Satellite Terrestrial Networks". *IEEE Internet of Things Journal*, 8(18):14399–14417, 2021.
- [26] Xiangming Zhu and Chunxiao Jiang. "Integrated Satellite-Terrestrial Networks Toward 6G: Architectures, Applications, and Challenges". *IEEE Internet of Things Journal*, 9(1):437–461, 2022.
- [27] Xingqin Lin, Stefano Cioni, Gilles Charbit, Nicolas Chuberre, Sven Hellsten, and Jean-Francois Boutillon. "On the Path to 6G: Embracing the Next Wave of Low Earth Orbit Satellite Access". *IEEE Communications Magazine*, 59(12):36–42, 2021.

- [28] Haoran Xie, Yafeng Zhan, Guanming Zeng, and Xiaohan Pan. "LEO Mega-Constellations for 6G Global Coverage: Challenges and Opportunities". *IEEE Access*, 9:164223–164244, 2021.
- [29] Alessandro Guidotti, Alessandro Vanelli-Coralli, Vincenzo Schena, Nicolas Chuberre, Mohamed El Jaafari, Jani Puttonen, and Stefano Cioni. The Path to 5G-Advanced and 6G Non-Terrestrial Network Systems. In *2022 11th Advanced Satellite Multimedia Systems Conference and the 17th Signal Processing for Space Communications Workshop (ASMS/SPSC)*, pages 1–8, 2022.
- [30] A. Guidotti, A. Vanelli-Coralli, M. Conti, S. Andrenacci, S. Chatzinotas, N. Maturo, B. Evans, A. Awoseyila, A. Ugolini, T. Foggi, L. Gaudio, N. Alagha, and S. Cioni. "Architectures and Key Technical Challenges for 5G Systems Incorporating Satellites". *IEEE Transactions on Vehicular Technology*, 68(3):2624–2639, 2019.
- [31] A. Guidotti, A. Vanelli-Coralli, M. Caus, J. Bas, G. Colavolpe, T. Foggi, S. Cioni, A. Modenini, and D. Tarchi. "Satellite-enabled LTE systems in LEO constellations". In *2017 IEEE International Conference on Communications Workshops (ICC Workshops)*, pages 876–881, 2017.
- [32] Alessandro Guidotti, Alessandro Vanelli-Coralli, Alberto Mengali, and Stefano Cioni. "Non-Terrestrial Networks: Link Budget Analysis". In *ICC 2020 - 2020 IEEE International Conference on Communications (ICC)*, pages 1–7, 2020.
- [33] 3GPP. "Technical Specification Group Radio Access Network; Study on New Radio (NR) to Support Non-Terrestrial networks (Release 15). Technical Report TR38.811 V15.4.1, 3GPP, October 2020.
- [34] C.E. Mayer, B.E. Jaeger, R.K. Crane, and Xuhe Wang. "Ka-band Scintillations: Measurements and Model Predictions". *Proceedings of the IEEE*, 85(6):936–945, 1997.
- [35] ITU-R. "Propagation Data and Prediction Methods Required for The Design of Earth-Space Telecommunication Systems". Technical Report "P.618, Tech. Rep., December 2017.

- [36] ITU-R. Itu-r p.531: ”Ionospheric Propagation Data and Prediction Methods Required For the Design of Satellite Networks and Systems”. Technical Report “ITU-R P.618, Tech. Rep., August 2019.
- [37] Yoann Couble, Catherine Rosenberg, Emmanuel Chaput, Jean-Baptiste Dupé, Cédric Baudoin, and André-Luc Beylot. ”Two-Color Scheme for a Multi-Beam Satellite Return Link: Impact of Interference Coordination”. *IEEE Journal on Selected Areas in Communications*, 36(5):993–1003, 2018.
- [38] E. Feltrin, J. Freixe, and E. Weller. ”Mobility in Ku and Ka bands: the Eutelsat’s point of view”. In *Proceedings of the 5th European Conference on Antennas and Propagation (EUCAP)*, pages 2336–2340, 2011.
- [39] Hien Quoc Ngo, Alexei Ashikhmin, Hong Yang, Erik G. Larsson, and Thomas L. Marzetta. ”Cell-Free Massive Mimo Versus Small Cells”. *IEEE Transactions on Wireless Communications*, 16(3):1834–1850, 2017.
- [40] Wei-Shun Liao, Mirza Golam Kibria, Gabriel Porto Villardi, Ou Zhao, Kentaro Ishizu, and Fumihide Kojima. ”Coordinated Multi-Point Downlink Transmission for Dense Small Cell Networks”. *IEEE Transactions on Vehicular Technology*, 68(1):431–441, 2019.
- [41] Selcuk Bassooy, Hasan Farooq, Muhammad A. Imran, and Ali Imran. ”Coordinated Multi-Point Clustering Schemes: A Survey”. *IEEE Communications Surveys & Tutorials*, 19(2):743–764, 2017.
- [42] Muhammad Sohaib J. Solaija, Hanadi Salman, Abuu B. Kihero, Mehmet Izzet Sağlam, and Hüseyin Arslan. ”Generalized Coordinated Multipoint Framework for 5G and Beyond”. *IEEE Access*, 9:72499–72515, 2021.
- [43] S. M. Riazul Islam, Nurilla Avazov, Octavia A. Dobre, and Kyung-sup Kwak. ”Power-Domain Non-Orthogonal Multiple Access (NOMA) in 5G Systems: Potentials and Challenges”. *IEEE Communications Surveys and Tutorials*, 19(2):721–742, 2017.
- [44] Jianhang Chu, Xiaoming Chen, Caijun Zhong, and Zhaoyang Zhang. ”Robust Design for NOMA-Based Multibeam LEO Satellite Internet of Things”. *IEEE Internet of Things Journal*, 8(3):1959–1970, 2021.

- [45] Joel S. Biyoghe and Vipin Balyan. "A Survey of Existing Studies on NOMA Application to Multi-beam Satellite Systems for 5G". In V. Suma, Joy Iong-Zong Chen, Zubair Baig, and Haoxiang Wang, editors, *Inventive Systems and Control*, pages 255–267, Singapore, 2021. Springer Singapore.
- [46] Kang An, Xiaojuan Yan, Tao Liang, and Weixin Lu. "NOMA Based Satellite Communication Networks: Architectures, Techniques and Challenges". In *2019 IEEE 19th International Conference on Communication Technology (ICCT)*, pages 1105–1110, 2019.
- [47] Lina Wang, Yanan Wu, Haijun Zhang, Sunghyun Choi, and Victor C. M. Leung. "Resource Allocation for NOMA Based Space-Terrestrial Satellite Networks". *IEEE Transactions on Wireless Communications*, 20(2):1065–1075, 2021.
- [48] Alan Barbieri, Dario Fertonani, and Giulio Colavolpe. "Time-Frequency Packing for Linear Modulations: Spectral Efficiency and Practical Detection Schemes". *IEEE Transactions on Communications*, 57(10):2951–2959, 2009.
- [49] Mrinmoy Jana, Lutz Lampe, and Jeebak Mitra. "Design of Time-Frequency Packed WDM Superchannel Transmission Systems". *Journal of Lightwave Technology*, 38(24):6719–6731, 2020.
- [50] Giulio Colavolpe, Andrea Modenini, Amina Piemontese, and Alessandro Ugolini. Multiuser Detection in Multibeam Satellite systems: Theoretical Analysis and Practical Schemes. In *2015 IEEE 16th International Workshop on Signal Processing Advances in Wireless Communications (SPAWC)*, pages 525–529, 2015.
- [51] F. Lombardo, E.A. Candreva, I. Thibault, A. Vanelli-Coralli, and G.E. Corazza. "Multi-user interference mitigation techniques for broadband multi-beam satellite systems". In *2011 Conference Record of the Forty Fifth Asilomar Conference on Signals, Systems and Computers (ASILOMAR)*, pages 1805–1809, 2011.
- [52] Sirui Miao, Neng Ye, Qiaolin Ouyang, Peisen Wang, Xiangming Li, and Lian Zhao. "Cooperative Multi-User Detection for Satellite IoT under Constrained ISLs". In *2023 IEEE 34th Annual International Symposium on*

- Personal, Indoor and Mobile Radio Communications (PIMRC)*, pages 1–6, 2023.
- [53] Pantelis-Daniel Arapoglou, Alberto Ginesi, Stefano Cioni, Stefan Erl, Federico Clazzer, Stefano Andrenacci, and Alessandro Vanelli-Coralli. "DVB-S2X-Enabled Precoding for High Throughput Satellite Systems". *International Journal of Satellite Communications and Networking*, 34(3):439–455, 2016.
- [54] ITU. "Modelling and Simulation of IMT Networks and Systems for Use in Sharing and Compatibility Studies". Technical Report ITU-R M.2101-0, Tech. Rep., 2017.
- [55] Harry L. Van Trees. "*Optimum Array Processing: Part IV of Detection, Estimation, and Modulation Theory*". John Wiley and Sons, 2004.
- [56] Alfano Giuseppa, Carla Fabiana Chiasserini, Nordio Alessandro, DANIEL GAETANO Riviello, et al. "A Random Matrix Model for mmWave MIMO Systems". *ACTA PHYSICA POLONICA. B*, 51:1627–1640, 2020.
- [57] ITU. "Modelling and Simulation of IMT Networks and Systems for Use in Sharing and Compatibility Studies". Technical Report ITU-R M.2101, Tech. Rep., February 2017.
- [58] 3GPP. "Study of Radio Frequency (RF) and Electromagnetic Compatibility (MC) Requirements for Active Antenna Array System (AAS) Base Station (Release 12)". Technical Report TR 37.840 V12.1.0, 3GPP, December 2013.
- [59] 3GPP. "Study on New Radio to support Non-Terrestrial Networks", Release 15. Technical Report TR 38.811 V15.4.0, 3GPP, September 2020.
- [60] Alessandro Guidotti, Claudio Sacchi, and Alessandro Vanelli-Coralli. "Feeder Link Precoding for Future Broadcasting Services". *IEEE Transactions on Aerospace and Electronic Systems*, 58(4):3126–3146, 2022.
- [61] Rusdha Muharar and Jamie Evans. "Downlink Beamforming with Transmit-Side Channel Correlation: A Large System Analysis". In *2011 IEEE International Conference on Communications (ICC)*, pages 1–5, 2011.

- [62] Vincenzo Icolari, Alessandro Guidotti, Daniele Tarchi, and Alessandro Vanelli-Coralli. "An interference estimation technique for Satellite cognitive radio systems". In *2015 IEEE International Conference on Communications (ICC)*, pages 892–897, 2015.
- [63] Piero Angeletti and Riccardo De Gaudenzi. "A Pragmatic Approach to Massive MIMO for Broadband Communication Satellites". *IEEE Access*, 8:132212–132236, 2020.
- [64] Mirette Sadek and Sonia Aissa. "Leakage Based Precoding for Multi-User MIMO-OFDM Systems". *IEEE Transactions on Wireless Communications*, 10(8):2428–2433, 2011.
- [65] Bingying Ren, Mao Wang, Chunliang Yang, Linjiao Wang, Jun Zou, Tingting Liu, and Wenjie Yang. "An Improved Leakage-Based Precoding Scheme for Multi-User MIMO Systems". In *2013 IEEE 77th Vehicular Technology Conference (VTC Spring)*, pages 1–4, 2013.
- [66] Daniel Gaetano Riviello, Francesco Di Stasio, and Riccardo Tuninato. "Performance Analysis of Multi-User MIMO Schemes under Realistic 3GPP 3-D Channel Model for 5G mmWave Cellular Networks". *Electronics*, 11(3), 2022.
- [67] Daniel Gaetano Riviello, Riccardo Tuninato, and Roberto Garelo. "assessment of MU-MIMO Schemes With Cylindrical Arrays Under 3GPP 3D Channel Model for B5G Networks". In *2023 IEEE 20th Consumer Communications and Networking Conference (CCNC)*, pages 769–774, 2023.
- [68] Zhi Lin, Kang An, Hehao Niu, Yihua Hu, Symeon Chatzinotas, Gan Zheng, and Jiangzhou Wang. "SLNR-Based Secure Energy Efficient Beamforming in Multibeam Satellite Systems". *IEEE Transactions on Aerospace and Electronic Systems*, 59(2):2085–2088, 2023.
- [69] Kang An, Min Lin, Jian Ouyang, and Wei-Ping Zhu. "Secure Transmission in Cognitive Satellite Terrestrial Networks". *IEEE Journal on Selected Areas in Communications*, 34(11):3025–3037, 2016.
- [70] Zhi Lin, Hehao Niu, Kang An, Yong Wang, Gan Zheng, Symeon Chatzinotas, and Yihua Hu. "Refracting RIS-Aided Hybrid Satellite-Terrestrial Re-

- lay Networks: Joint Beamforming Design and Optimization”. *IEEE Transactions on Aerospace and Electronic Systems*, 58(4):3717–3724, 2022.
- [71] Miguel Ángel Vázquez, Xavier Artiga, and Ana I. Pérez-Neira. ”Closed-Form Multicast Precoding for Satellite Flexible Payloads”. In *2021 29th European Signal Processing Conference (EUSIPCO)*, pages 910–914, 2021.
- [72] Mirette Sadek, Alireza Tarighat, and Ali H. Sayed. ”A Leakage-Based Precoding Scheme for Downlink Multi-User MIMO Channels”. *IEEE Transactions on Wireless Communications*, 6(5):1711–1721, 2007.
- [73] Piya Patcharamaneepakorn, Simon Armour, and Angela Doufexi. ”On the Equivalence Between SLNR and MMSE Precoding Schemes with Single-Antenna Receivers”. *IEEE Communications Letters*, 16(7):1034–1037, 2012.
- [74] Wang J. et al Li Y., Hu SL. ”An Introduction to the Computational Complexity of Matrix Multiplication”. *J. Oper. Res. Soc. China*, page 29–43, 2020.
- [75] Tian Lin, Jiaqi Cong, Yu Zhu, Jun Zhang, and Khaled Ben Letaief. ”Hybrid Beamforming for Millimeter Wave Systems Using the MMSE Criterion”. *IEEE Transactions on Communications*, 67(5):3693–3708, 2019.
- [76] Alessandro Guidotti and Alessandro Vanelli-Coralli. ”Design Trade-off Analysis of Precoding Multi-Beam Satellite Communication Systems”. In *2021 IEEE Aerospace Conference (50100)*, pages 1–12, 2021.
- [77] 3GPP. ”Solutions for NR to support Non-Terrestrial Networks (NTN)”. Technical Report TR 38.821, 3GPP, 2021.
- [78] 3GPP. ”Service Requirements for the 5G system; Stage 1 (Release 18)”. Technical Report TS 22.261 V18.2.0, 3GPP, 2021.
- [79] Paolo Rocca, Michele D’Urso, and Lorenzo Poli. ”Advanced Strategy for Large Antenna Array Design With Subarray-Only Amplitude and Phase Control”. *IEEE Antennas and Wireless Propagation Letters*, 13:91–94, 2014.
- [80] Luca Manica, Paolo Rocca, and Andrea Massa. ”Design of Subarrayed Linear and Planar Array Antennas With SLL Control Based on an Excitation

- Matching Approach”. *IEEE Transactions on Antennas and Propagation*, 57(6):1684–1691, 2009.
- [81] T. Isernia, M. D’Urso, and O. M. Bucci. ”A Simple Idea for an Effective Sub-Arraying of Large Planar Sources”. *IEEE Antennas and Wireless Propagation Letters*, 8:169–172, 2009.
- [82] Nuan Song, Tao Yang, and Huan Sun. ”Overlapped Subarray Based Hybrid Beamforming for Millimeter Wave Multiuser Massive MIMO”. *IEEE Signal Processing Letters*, 24(5):550–554, 2017.
- [83] Yan Wang, Biaolin Yan, Rong Yu, Mengmeng Fan, Zhongxing Duan, Zongfa Ma, Hongping Fu, Zhihai Wang, Kunpeng Yu, Wenzhi Wu, and Congsi Wang. ”Sub-array Level Structural Compensation Method for Radiating and Scattering Performance of Array Antennas”. *IET Microwaves, Antennas & Propagation*, 17(12):940–954, 2023.
- [84] Santhi Swaroop Madeti, Stephen E. Saddow, and Gokhan Mumcu. ”Low Complexity Beam Steering Antenna Array Using Beamforming Network Subarrays”. In *2022 IEEE 22nd Annual Wireless and Microwave Technology Conference (WAMICON)*, pages 1–4, 2022.
- [85] Bilgehan Avser, John Pierro, and Gabriel M. Rebeiz. ”Random Feeding Networks for Reducing the Number of Phase Shifters in Limited-Scan Arrays”. *IEEE Transactions on Antennas and Propagation*, 64(11):4648–4658, 2016.
- [86] Juan Andrés Vásquez-Peralvo, Jorge Querol, Flor Ortíz, Jorge Luis González Rios, Eva Lagunas, Victor Monzon Baeza, Gianluca Fontanesi, Luis Manuel Garcés-Socorrás, Juan Carlos Merlano Duncan, and Symeon Chatzinotas. ”Flexible Beamforming for Direct Radiating Arrays in Satellite Communications”. *IEEE Access*, 11:79684–79696, 2023.
- [87] Sangbae Oh, Jungjin Shin, Hyojoon Lim, Joongki Park, Heedong Do, and Namyoon Lee. ”Linear Subarrays for Multi-Beam Satellites”. In *2023 14th International Conference on Information and Communication Technology Convergence (ICTC)*, pages 802–804, 2023.

- [88] Yanki Aslan, Jan Puskely, Antoine Roederer, and Alexander Yarovoy. "Active Multiport Subarrays for 5G Communications". In *2019 IEEE-APS Topical Conference on Antennas and Propagation in Wireless Communications (APWC)*, pages 298–303, 2019.
- [89] Joan Palacios, Nuria González-Prelcic, Carlos Mosquera, Takayuki Shimizu, and Chang-Heng Wang. "A Hybrid Beamforming Design for Massive MIMO LEO Satellite Communications". *Frontiers in Space Technologies*, 2, 2021.
- [90] Akram Najjar, Mohammed El-Absi, and Thomas Kaiser. "Dynamic Array of Subarrays Architecture Based Hybrid Beamforming in UM-MIMO Systems". In *2021 Fourth International Workshop on Mobile Terahertz Systems (IWMTS)*, pages 1–5, 2021.
- [91] Randy L. Haupt. "*Antenna Arrays: A Computational Approach*". Wiley-IEEE Press, 2010.
- [92] Robert J. Mailloux. "Subarray technology for time delayed scanning arrays". In *2009 IEEE International Conference on Microwaves, Communications, Antennas and Electronics Systems*, pages 1–6, 2009.
- [93] Marco Bertola and Ayman Assra. "Random Matrix Approach for the Capacity of Large-Scale MIMO Systems using the Harish-Chandra Formula". In *2020 14th International Conference on Signal Processing and Communication Systems (ICSPCS)*, pages 1–8, 2020.
- [94] Bassel Al Homssi, Akram Al-Hourani, Ke Wang, Phillip Conder, Sithamparamanathan Kandeepan, Jinho Choi, Ben Allen, and Ben Moores. "Next Generation Mega Satellite Networks for Access Equality: Opportunities, Challenges, and Performance". *IEEE Communications Magazine*, 60(4):18–24, 2022.
- [95] Wei Jiang, Bin Han, Mohammad Asif Habibi, and Hans Dieter Schotten. "The Road Towards 6G: A Comprehensive Survey". *IEEE Open Journal of the Communications Society*, 2:334–366, 2021.
- [96] 3GPP. "Study on New Radio Access Technology: Radio Access Architecture and Interfaces". Technical Report TR 38.801, 2017.

- [97] Mohammed Y. Abdelsadek, Gunes Karabulut-Kurt, Halim Yanikomeroglu, Peng Hu, Guillaume Lamontagne, and Khaled Ahmed. "Broadband Connectivity for Handheld Devices via LEO Satellites: Is Distributed Massive MIMO the Answer?". *IEEE Open Journal of the Communications Society*, 4:713–726, 2023.
- [98] L. A. Grieco, G. Piro, A. Petrosino, S. Morosi, A. Guidotti, D. Tarchi, A. Vanelli-Coralli, E. Cianca, M. Ruggieri, P. Salvo, F. Matera, V. Petrini, and S. Valbonesi. "Integration of Terrestrial and Non-Terrestrial Networks for Automotive: Challenges and Perspectives Within the S11 RESTART Project". In *2023 AEIT International Conference on Electrical and Electronic Technologies for Automotive (AEIT AUTOMOTIVE)*, pages 1–6, 2023.
- [99] Channasandra Ravishankar, Rajeev Gopal, Nassir BenAmmar, Gaguk Zakaria, and Xiaoling Huang. "Next-Generation Global Satellite System With Mega-Constellations". *International Journal of Satellite Communications and Networking*, 39(1):6–28, 2021.
- [100] Jun Zhang, Xianghao Yu, and Khaled B. Letaief. "Hybrid Beamforming for 5G and Beyond Millimeter-Wave Systems: A Holistic View". *IEEE Open Journal of the Communications Society*, 1:77–91, 2020.
- [101] Juping Zhang, Gan Zheng, Yangyishi Zhang, Ioannis Krikidis, and Kai-Kit Wong. "Deep Learning Based Predictive Beamforming Design". *IEEE Transactions on Vehicular Technology*, 72(6):8122–8127, 2023.
- [102] Ziyuan Zheng, Wenpeng Jing, Zhaoming Lu, and Xiangming Wen. "RIS-Enhanced LEO Satellite Communication: Joint Passive Beamforming and Orientation Optimization". In *2022 IEEE Globecom Workshops (GC Workshops)*, pages 874–879, 2022.

## Acknowledgements

This thesis represents the culmination of three years of dedicated effort. I extend my sincere gratitude to the numerous individuals who have been by my side throughout this journey, offering their support and contributing to my personal and professional growth. The pursuit of a Ph.D. is paradoxically both the longest and shortest period of our lives, marked by moments of frustration, fatigue, and tears, as well as excitement, astonishment, joy, friendship, wonder, accomplishment and growth.

I would like to thank Professor **Alessandro Vanelli-Coralli**, who believed in me from the very beginning and gave me the opportunity to embark on this path. He has been an exceptional mentor, teacher, and significant influence in my journey. I am grateful to him for the valuable lessons he imparted, particularly his encouragement to persevere and never give up, always striving for perfection in the work. I have learned not only from his extensive expertise in research and academic life but also from his exceptional personality and his soft and communication skills. Professor Vanelli-Coralli taught me the art of constructive criticism and improvement of the work with kindness and wisdom manner, and how to be a great manager during observing his management of several European projects within Unibo's team. Beyond the professional aspects, Professor Vanelli-Coralli has stood by my side in numerous challenging circumstances throughout these three years when I was far from my home country and family by providing

support and help whenever is possible. Describing my feelings towards Professor Alessandro is challenging. In essence, he is not only an outstanding professor but also a great human. I am indebted for fate brought me to work under his guidance within his research group.

I would like to thank prof. Alessandro Guidotti for his guidance and efforts he gave to me during this journey. I have learned a lot from his great experience in NTN.

I would like to thank Dr. Daniel Gaetano Riviello for his consistent guidance and efforts. He was always available to clarify and discuss any doubts, showcasing his dedication and support. Together, Dr. Riviello and I weathered difficult times, grappling with frustrations over problematic results or paper rejections. At the same time, we celebrated moments of success and happiness when we solved problems, achieved outstanding results and had papers accepted.

Special thanks to Carla Amatetti, she was my first colleague at DIGI-COMM Lab, starting from my Master thesis as a co-supervisor until now as a colleague and friend. She was always available to provide me any possible help or support in the research and also in the difficult circumstances in which I passed.

I would like to express my gratitude to all my other colleagues in the DIGI-COMM lab; Riccardo Campana, Bruno De Filippo, Bilal Ahmad and Andrea Ambra Pescio, with whom I have shared numerous meaningful moments throughout this journey. And also to my new colleagues: Navid Hosseinzadehdehlan and Mahdi Abdollahpour for their motivational words during the stressed period of thesis writing.

Very special thanks to Swapnil Sadashiv Shinde for his kindness and support who motivated me in the most difficult moments during this journey. And thanks to all other colleagues and researchers who I met in the lab and spread positive vibes to me during this step, thanks David Naseh and Angela Faiella.

Additionally, I extend my appreciation to all the professors, teachers, and staff at UNIBO, and DEI department, particularly to Prof. Giovanni Emanuele Corazza, the founder of DIGICOMM LAB.

Many thanks to:

- My deceased father, Mustafa Dakkak: I hope you are alive today to witness that your youngest son is on the verge of achieving your dream—a doctorate in engineering.
- My life, my mother, Ghithaa Salem: I am doing my best always to make you happy and proud of me.
- To my brother and sister, Abdo and Abir Dakkak, who have always believed in me, motivated me and celebrated the moments of my success.
- To my best friend forever that we got to know each other in Italy, Mervat Mutluk, she believed in me and was the main supporter to me, especially in the moments of frustration and fatigue. She is such a great person and a amazing friend.
- To my best friend forever, Qasem Hussien, even if we lived far away in the last few years, but he always stood by my side, believed in me, provided

motivation during moments of fatigue, and celebrated the moments of my success.

- To all my friends: Hind, Muhammad, and Khaleel who stood by my side, and believed in me.
- Lastly, I would like to convey my heartfelt wishes for peace and safety to my country, "Syria," and to my beloved city, "Aleppo." It is my sincere hope that I have represented them very well here in Italy.
- I extend my thanks to all the individuals who have supported me, even if with just a single positive word, directly or indirectly, throughout the process of completing this thesis.